


Spring 5-2017

Effect of Chain Rigidity on Network Architecture and Deformation Behavior of Glassy Polymer Networks

Kyler Reser Knowles
University of Southern Mississippi

Follow this and additional works at: <https://aquila.usm.edu/dissertations>

 Part of the [Materials Chemistry Commons](#), [Polymer and Organic Materials Commons](#), [Polymer Chemistry Commons](#), and the [Structural Materials Commons](#)

Recommended Citation

Knowles, Kyler Reser, "Effect of Chain Rigidity on Network Architecture and Deformation Behavior of Glassy Polymer Networks" (2017). *Dissertations*. 1316.
<https://aquila.usm.edu/dissertations/1316>

This Dissertation is brought to you for free and open access by The Aquila Digital Community. It has been accepted for inclusion in Dissertations by an authorized administrator of The Aquila Digital Community. For more information, please contact aquilastaff@usm.edu.

EFFECT OF CHAIN RIGIDITY ON NETWORK ARCHITECTURE AND
DEFORMATION BEHAVIOR OF GLASSY POLYMER NETWORKS

by

Kyler Reser Knowles

A Dissertation
Submitted to the Graduate School
and the School of Polymers and High Performance Materials
at The University of Southern Mississippi
in Partial Fulfillment of the Requirements
for the Degree of Doctor of Philosophy

Approved:

Dr. Jeffrey S. Wiggins, Committee Chair
Associate Professor, Polymers and High Performance Materials

Dr. Sergei I. Nazarenko, Committee Member
Professor, Polymers and High Performance Materials

Dr. Sarah E. Morgan, Committee Member
Professor, Polymers and High Performance Materials

Dr. Robson F. Storey, Committee Member
Distinguished Professor, Polymers and High Performance Materials

Dr. Gopinath Subramanian, Committee Member
Assistant Professor, Polymers and High Performance Materials

Dr. Karen S. Coats
Dean of the Graduate School

May 2017

COPYRIGHT BY

Kyler Reser Knowles

2017

Published by the Graduate School



THE UNIVERSITY OF
SOUTHERN
MISSISSIPPI.

ABSTRACT

ROLE OF CHAIN RIGIDITY IN NETWORK ARCHITECTURE AND DEFORMATION BEHAVIOR OF GLASSY POLYMER NETWORKS

by Kyler Reser Knowles

May 2017

Processing carbon fiber composite laminates creates molecular-level strains in the thermoset matrix upon curing and cooling which can lead to failures such as geometry deformations, micro-cracking, and other issues. It is known strain creation is attributed to the significant volume and physical state changes undergone by the polymer matrix throughout the curing process, though storage and relaxation of cure-induced strains remain poorly understood. This dissertation establishes two approaches to address the issue. The first establishes testing methods to simultaneously measure key volumetric properties of a carbon fiber composite laminate and its polymer matrix. The second approach considers the rigidity of the polymer matrix in regards to strain storage and relaxation mechanisms which ultimately control composite performance throughout manufacturing and use.

Through the use of a non-contact, full-field strain measurement technique known as digital image correlation (DIC), we describe and implement useful experiments which quantify matrix and composite parameters necessary for simulation efforts and failure models. The methods are compared to more traditional techniques and show excellent correlation. Further, we established relationships which represent matrix-fiber compatibility in regards to critical processing constraints.

The second approach involves a systematic study of epoxy-amine networks which are chemically-similar but differ in chain segment rigidity. Prior research has investigated the isomer effect of glassy polymers, showing sizeable differences in thermal, volumetric, physical, and mechanical properties. This work builds on these themes and shows the apparent isomer effect is rather an effect of chain rigidity. Indeed, it was found that structurally-dissimilar polymer networks exhibit very similar properties as a consequence of their shared average network rigidity. Differences in chain packing, as a consequence of chain rigidity, were shown to alter the physical, volumetric, and mechanical properties of the glassy networks. Chain rigidity was found to directly control deformation mechanisms, which were related to the yielding behavior of the epoxy network series. The unique benefit to our approach is the ability to separate the role of rigidity – an intramolecular parameter – from intermolecular phenomena which otherwise influence network properties.

ACKNOWLEDGMENTS

Most importantly, I extend incredible gratitude to my advisor and mentor, Dr. Jeffrey Wiggins. Our discussions and life pontifications began with my recruitment in 2011 when Dr. Wiggins stood upon his figurative soapbox. He laid out his argument for the opportunities and “intellectual freedom” a graduate degree could offer a young, aspiring scientist with a background like my own. Like those before me, his “hands-off” management style led to struggles and frustrations, but through the process came confidence and growth. “Doc” places significant emphasis on the professional development of his students, and is never shy to share his philosophies - from the importance of cultivating relationships to big picture thinking and “how this stuff works.” He has made me a better researcher, communicator, teacher, and leader, and I am forever grateful for his guidance and mentorship.

For their ongoing consult and guidance, I extend sincere gratitude to my committee: Dr. Robson Storey, Dr. Sarah Morgan, Dr. Gopinath Subramanian, and Dr. Sergei Nazarenko. I especially want to thank Dr. Nazarenko for the countless hours he invested in me, particularly in the final months of my tenure. His guidance has tested my logic, experimental approach, and understanding of purpose-driven research.

I would also like to thank Dr. Derek Patton and Dr. Sarah Morgan for their guidance under the National Science Foundation Research Traineeship (NRT). The program’s emphasis on communication and leadership skills resonated with my passions and challenged my professional development. I am extremely grateful for the opportunities and experiences afforded to me through the traineeship. I also thank my fellow Year 1 Cohort for their guidance and criticisms as I addressed my strengths and

weaknesses. They say it takes a village to raise a child, and I have found no less is true for the development of a scientist.

To all of my mentors – and there are many – I extend great thanks. I would like to especially thank Dr. Sam Tucker, Dr. Matthew Jackson, and Dr. Stephen Heinz. As WRG alumni, they served as so much more than sponsors of my research but consistently invested time in my development as a researcher and professional. A noteworthy quote came from Dr. Stephen Heinz that I revisited often throughout my graduate tenure: “Do not perform experiments to solve problems. Ask questions, and then answer those questions with experiments.” I also thank Steve Christensen for the countless hours of phone and email conversations challenging my logic and understanding. Perhaps the best representation of his mentorship is embodied by his quote: “Ah the innocence of youth taking on the giants of science.” For helping me understand and appreciate the “giants,” I am grateful.

I would like to acknowledge those of the School of Polymers and High Performance Materials that made this research possible, specifically Richard Ferguson for aiding mechanical testing efforts, and David Delatte for supporting thermal and thermomechanical studies and instrumentation.

From the bottom of my heart, I thank the WRG family. Our administrative staff, Mrs. Charlie McMillin and Mrs. Stephanie Patton, I thank you for keeping the wheels of WRG turning, and on many occasions giving me encouragement, kindness, and food. To my lab mates Dr. John Misasi, Dr. Jeremy Moskowitz, Dr. Brian Greenhoe, Andy Frazee, Amit Sharma, and Andrew Janisse, thank you for your support, guidance, criticism, and adventures – both in the lab, and out.

Finally, I am eternally grateful of the friendships made along the way, specifically the 807 Crew: Drs. Jim Goetz, Brooks Abel, Lea Paslay, Dave Krzeminski, and Brian Greenhoe. Spending time with these guys – usually while pedaling a bike – has made me a better man.

DEDICATION

Above all, this dissertation is dedicated to my wife, Hanna, whose support has been endless and unwavering throughout the tumultuous life season of graduate school. From year one to year five, her support and care have not only made this journey possible but immensely fulfilling. I also dedicate this to my parents, Greg and Shareen, who have challenged and encouraged me to grow in all of aspects of life. From music to athletics, they have engrained in me a work ethic to pursue a life full of importance and meaning. I also dedicate this to my sister, Kaylee, whom I admire in more ways than words can describe.

“We do not think ourselves into new ways of living, we live ourselves into new ways of thinking.” – Richard Rohr

TABLE OF CONTENTS

ABSTRACT ii

ACKNOWLEDGMENTS iv

DEDICATION vii

LIST OF TABLES xiv

LIST OF ILLUSTRATIONS xv

CHAPTER I - INTRODUCTION 1

 1.1 Research Motives 1

 1.2 Background 2

 1.2.1 Cure-induced Strain in Composites 2

 1.2.1.1 Chemical Shrinkage 3

 1.2.1.2 Coefficient of Thermal Expansion 5

 1.2.1.3 Gelation and Vitrification 8

 1.2.1.4 Cure-induced Strain Measurement Methods 9

 1.2.2 Strain Development and Polymer Deformation 10

 1.2.2.1 Onset Theory 10

 1.2.2.2 Yield 11

 1.2.2.3 Deformation Theories 13

 1.2.2.4 Deformation Mechanisms of Amorphous Glasses 16

 1.2.3 Chain Rigidity and Cooperativity 18

1.2.3.1 Chain Rigidity	18
1.2.3.2 Cooperativity of Polymer Glasses	19
1.2.3.3 Polymer Fragility	20
1.3 Research Overview	22
CHAPTER II - EXPERIMENTAL.....	24
2.1 Materials	24
2.2 Glassy Polymer Network Preparation.....	25
2.2.1 Preparation of Commercial Matrix Specimens.....	25
2.2.2 Matrix Formulation.....	25
2.2.3 Test Specimen Preparation	25
2.3 Laminate Fabrication	26
2.4 Analysis.....	27
2.4.1 Mechanical Testing.....	27
2.4.1.1 Compression Testing	27
2.4.1.2 Tensile Testing.....	28
2.4.2 Thermal Analysis	28
2.4.2.1 Differential Scanning Calorimetry.....	28
2.4.2.2 Thermogravimetric Analysis	29
2.4.3 Thermomechanical Testing.....	30
2.4.3.1 Rheology.....	30

2.4.3.2 Thermomechanical Analysis.....	30
2.4.3.3 Dynamic Mechanical Analysis	31
2.4.4 Density Testing	31
2.4.5 Digital Image Correlation	32
2.4.5.1 Digital Image Correlation Measurement	32
2.4.5.2 Image Analysis.....	32
CHAPTER III - THERMAL AND VOLUMETRIC PROPERTY ANALYSIS OF POLYMER NETWORKS AND COMPOSITES USING ELEVATED TEMPERATURE DIGITAL IMAGE CORRELATION.....	34
3.1 Introduction.....	34
3.2 Elevated Temperature Digital Image Correlation.....	37
3.3 Results and Discussion	39
3.3.1 Chemical Shrinkage	39
3.3.2 Thermal Expansion of Matrix and UD Fiber-Reinforced Composites	40
3.3.3 Laminate Strain-free Temperature	43
3.3.4 Laminate Curvature Development.....	45
3.4 Conclusions.....	50
CHAPTER IV – EFFECT OF CHAIN RIGIDITY ON THERMAL, PHYSICAL, AND THERMOMECHANICAL PROPERTIES OF GLASSY AMORPHOUS NETWORKS	52

4.1 Introduction.....	52
4.2 Results and Discussion	55
4.2.1 Effect of Structural Isomers on Network Thermal Properties	55
4.2.1.1 Polymer Fragility Considerations	59
4.2.2 Role of structural isomers and chain rigidity in network architecture.....	64
4.2.2.1 Effect on Chain Packing	64
4.2.2.2 Free Volume Considerations.....	65
4.2.3 Influence of Network Rigidity on Thermal Expansion.....	69
4.2.3.1 Polymer Fragility Considerations	76
4.2.3.2 Influence of Network Connectivity	82
4.2.3.2.1 Difunctional vs. Multifunctional Epoxy Prepolymers	82
4.2.3.2.2 Alternative curing schedules.....	85
4.2.4 Effect of Network Rigidity on Mechanical Relaxations.....	86
4.2.4.2 Polymer Fragility Considerations	95
4.3 Conclusions.....	97
 CHAPTER V – ROLE OF CHAIN RIGIDITY IN GLASSY STATE DEFORMATION PROCESSES OF AMORPHOUS POLYMER NETWORKS.....	
5.1 Introduction.....	99
5.2 Results and Discussion	101
5.2.1 Effect of Network Rigidity on Mechanical Properties	101

5.2.1.1 Relationship of Chain Rigidity and Elastic Modulus	101
5.2.1.2 Role of Chain Rigidity on Yield Stress and Strain	105
5.2.1.3 Relating Chain Rigidity to Elastic Recovery	107
5.2.2 Effect of Network Rigidity on Deformation Mechanisms.....	108
5.2.2.1 Observing Deformation Mechanisms by Calorimetry	108
5.2.3 Separating Deformation Mechanisms via Strain Recovery Experiments.....	115
5.2.3.2 Deformation Components of Network Isomer Series.....	121
5.2.3.3 Network Architecture Considerations.....	128
5.2.3.4 Effect of Deformation Temperature.....	130
5.2.3.5 Correlation of Deformation Processes with Yield	131
5.2.3.6 Network Deformation Scheme	133
5.2.3.7 Network Rigidity and Deformation Mechanism Limits	139
5.2.4 Elevated Temperature Tensile Testing	140
5.3 Conclusions.....	142
CHAPTER VI CONCLUDING REMARKS AND FUTURE WORK.....	144
APPENDIX A – Molecular Dynamics Simulation.....	147
A.1 Introduction.....	147
A.2 Experimental	147
A.2.1 Simulation.....	147
A.2.2 High Pressure Mercury Dilatometry	148

A.3 Results and Discussion.....	149
REFERENCES	162

LIST OF TABLES

Table 2.1 <i>Thermal Cure Profiles.</i>	26
Table 2.2 <i>Polymer Network Mold Materials and Geometries.</i>	26
Table 3.1 <i>CTE values of the matrix and UD laminate obtained via TMA and DIC.</i>	42
Table 3.2 <i>Glassy-state CTE values for variable fiber orientation laminates.</i>	47
Table 4.1 <i>Epoxy prepolymers and diamine curatives.</i>	54
Table 4.2 <i>Epoxy-amine network isomer nomenclature.</i>	54
Table 4.3 <i>T_gs of networks formed from structural isomers.</i>	58
Table 4.4 <i>Differences in thermodynamic fragility via DSC measurements.</i>	62
Table 4.5 <i>Thermal and physical properties of difunctional epoxy network isomers.</i>	65
Table 4.6 <i>Thermal and architectural property relationships of network isomers.</i>	74
Table 4.7 <i>Temperature dependence of network CTEs by TMA measurements.</i>	78
Table 4.8 <i>Rate of change of CTE and breadth of glass transition by TMA.</i>	80
Table 4.9 <i>Multifunctional epoxy prepolymer.</i>	83
Table 4.10 <i>Thermal property comparison of DGEBF and TGDDM network isomers.</i> ...	84
Table 4.11 <i>Thermal property comparison of DGEBF and TGDDM network isomers.</i> ...	86
Table 4.12 <i>DMA frequency sweep for sub-T_g relaxations from 33A tanδ curves.</i>	90
Table 4.13 <i>Loss modulus γ peak temperatures and apparent activation energies.</i>	94
Table 4.14 <i>DMA loss modulus α peak analysis.</i>	96
Table 5.1 <i>Elastic properties as compared to thermal and architectural properties.</i>	103
Table 5.2 <i>Mechanical properties of network isomer series.</i>	141
Table A.1 <i>Definition of force field parameters.</i>	151
Table A.2 <i>Polymer network densities measured by Archimedes' Principle.</i>	158

LIST OF ILLUSTRATIONS

Figure 1.1 Volume changes of a thermoset polymer network during cure.....	5
Figure 1.2 Deformation behaviors of polymer glasses.	12
Figure 3.1 Camera orientation for elevated temperature DIC.	38
Figure 3.2 Average change in linear dimension due to heating and continued curing.	40
Figure 3.3 Average dimension change due to thermal expansion of cured matrix.....	41
Figure 3.4 Laminate placement for CTE and strain-free temperature studies.....	43
Figure 3.5 Strain-free temperature measurements by changes in reference lengths.....	44
Figure 3.6 Changes in line length due to heating.....	47
Figure 3.7 Differences in line length changes with temperature.	49
Figure 4.1 DSC thermograms of 44F with and without thermal quenching.....	56
Figure 4.2 DSC thermograms showing T_g s of network isomer series.....	57
Figure 4.3 Diaminodiphenyl sulfone structural isomers.....	59
Figure 4.4 Heat flow and heat flow derivatives of DGEBA isomers.	61
Figure 4.5 DSC thermograms of 33F and 44A.....	62
Figure 4.6 Components of specific volume vs. temperature.	67
Figure 4.7 TMA plot of 33F sample length, first and second derivatives.	71
Figure 4.8 Dimension change and derivatives with respect to temperature.	72
Figure 4.9 Thermal expansion of network isomer series.....	73
Figure 4.10 Thermal expansion and derivatives of 44A with respect to temperature.	81
Figure 4.11 Storage modulus curves at 1Hz for network isomer series.	88
Figure 4.12 DMA frequency sweep for $\tan\delta$ curves of 33A.....	90
Figure 4.13 $\tan\delta$ sub- T_g relaxations at 1Hz for network isomer series.	92

Figure 4.14 Loss modulus sub- T_g transitions of network isomer series.	93
Figure 5.1 Stress-strain curves of epoxy network isomers in compression.	103
Figure 5.2 Vertically shifted DSC thermograms of deformed 33F cylinder.	110
Figure 5.3 Vertically shifted DSC thermograms of deformed 44F cylinder.	112
Figure 5.4 Vertically shifted DSC thermograms of deformed 33A cylinder.	112
Figure 5.5 Vertically shifted DSC thermograms of deformed 44A cylinder.	113
Figure 5.6 TMA strain recovery of 33A after deformation.	116
Figure 5.7 Derivative curves during thermal recovery of strained 33A cylinders.	118
Figure 5.8 Length change derivatives for samples deformed to 32.5%.	119
Figure 5.9 Recovery progress of network isomer series upon heating through T_g	121
Figure 5.10 Weight % vs. temperature for network isomers.	123
Figure 5.11 Strain components of 33F through progressing deformation.	124
Figure 5.12 Strain components of 44F through progressing deformation.	124
Figure 5.13 Strain components of 33A through progressing deformation.	125
Figure 5.14 Strain components of 44A through progressing deformation.	125
Figure 5.15 Recovery behavior of 44A tested at room and elevated temperatures.	131
Figure 5.16 Onset of the HTR process relative to stress-strain relationships.	133
Figure 5.17 Proposed deformation scheme for deformation mechanism development. ..	135
Figure 5.18 Length change derivatives of standard vs. restrained specimens.	136
Figure 5.19 Recovery progress for restrained and standard 44A specimens.	137
Figure 5.20 Recovery progress for restrained and standard 33A specimens.	138
Figure 5.21 Elevated temperature tension curves at $T_g + 50$ °C.	141
Figure A.1 DGEBF (left) and 33DDS (right) modified structures for simulation.	152

Figure A.2 Density upon annealing simulated 33F networks of increasing conversion.	154
Figure A.3 Room temperature density (300 K) for 33F at various conversions.....	155
Figure A.4 Density at 460 K for 33F at various conversions.	157
Figure A.5 Simulated chemical shrinkage of 33F.	159
Figure A.6 PVT volume change measurements and cell temperature vs. time.	160
Figure A.7 Simulated linear glassy state CTE of 33F at increasing conversions.	161

CHAPTER I - INTRODUCTION

1.1 Research Motives

Innovation is driven by necessity. As materials science had progressed through the Stone, Bronze, and Iron Ages, manufacturing knowledge has advanced through continuous engineering innovation. Starting with World War II the United States began a major engineering and manufacturing effort to develop fiber reinforced polymer matrix composites as lightweight replacement parts for metal aircraft. This work led to US dominance in aerospace composites through the Cold War with continuous advancement in composite science and engineering into the 21st Century.¹ The desire to produce aircraft with higher strength, lower weight, reduced fuel consumption, less maintenance and increased service life has driven the aerospace industry to continually advance composites manufacturing science and engineering for nearly 75 years. Although polymer matrix composites offer desirable benefits, the complexity of their properties demands significant research and engineering efforts for an improved understanding.

Glassy amorphous high T_g epoxy matrices have evolved for use in high-performance aerospace composite laminates through decades of use and advancement due to their high moduli and strengths, favorable processing properties, environmental stability, and economics. For these reasons, epoxies have emerged as the dominant polymer matrix, incorporated with high strength and modulus carbon fibers, employed for aerospace primary and secondary structures.¹ One important challenge still limiting the use of composites in certain manufacturing applications is associated with residual strains which develop in the polymer matrix during cure, often referred to as “cure-induced strains.” As matrix strain reaches a critical threshold, the associated stored

stresses are ultimately relieved through physical matrix-critical processes such as geometrical deformations, inter-layer delamination, and/or microcracking.²⁻⁵ As a result, further research on cure-induced strain in composite laminates in an attempt to better understand how strains develop and are stored within the polymer matrix during cure is necessary. Historical research has failed to lead to agreement within the composites science and engineering community on major concepts associated with cure-induced strains, in particular how polymer matrix strains are stored or relaxed throughout the progression of cure. Furthermore, there is considerable scientific disagreement associated with the most effective analytical methodology to quantify cure-induced strains in glassy amorphous polymer matrix composite laminates. This research will strive to enhance our fundamental understanding of key polymer properties which we believe ultimately dictate how residual strains build and relax in composite laminate structures. Our study will investigate the polymer volumetric and deformation properties which influence cure-induced strains in composite laminates to afford predictability and control to advance processing and performance.

1.2 Background

1.2.1 Cure-induced Strain in Composites

Continuous fiber reinforced polymer matrix composite laminates experience volumetric changes in the matrix during cure attributed to high processing temperatures and polymerization reactions. Carbon fibers in proximity with the reactive, crosslinking matrix create a constrained environment for the matrix reaction due to the high fiber volume fraction. Molecular dynamics simulation has shown the enthalpy of matrix-fiber interaction to be favorable, binding the matrix from free expansion and contraction which

ultimately leads to the formation of the interphase.⁶ Several groups suggest the volume change of the matrix in the presence of carbon fibers is influenced by processing conditions leading to variances in residual strains of a cured laminate due to differences in strain storage and relaxation.⁷⁻⁹

1.2.1.1 Chemical Shrinkage

During the cure of epoxy-amine polymer networks, small molecules and oligomers react through step-growth polymerization mechanisms at elevated temperature building in size through the gel-point and ultimately vitrify into a highly crosslinked glassy amorphous polymer network solid of infinite molecular weight. During polymerization, two distinct processes contribute to the dynamic volumetric state of the polymer matrix. First, during heating and cooling thermal variances lead to volumetric expansion and contraction of the polymer, and second chemical shrinkage leads to volumetric contraction through the formation of covalent bonds and non-covalent bonded forces as polymerization progresses and molecular weight increases.^{10,11} The extent of chemical shrinkage for a given polymerization reaction is specific to the chemical make-up of each monomer and pre-polymer molecule and varies with composition and extent of reaction (degree of cure). Each epoxy composition has a characteristic volumetric shrinkage during cure which typically resides in the range of 5-10%.¹² Higher functionality monomers which yield an increase in crosslink density display a higher degree of chemical shrinkage during cure.¹³ Glassy polymer networks that contain additives such as tougheners, fillers, nanomaterials or continuous fiber reinforcements display a reduction in chemical shrinkage (in the bulk) compared to unfilled networks.^{14,15} Figure 1.1 depicts a generalized schematic which shows a theoretical

matrix volume change during cure. Volume increase of the polymer from Point a to Point b shows thermal expansion which occurs during the initial heating of uncured materials. Reaction at the isothermal cure temperature causes significant densification due to chemical shrinkage (Point b to Point c). Upon completion of cure and subsequent cooling (Point c to Point e), thermal contraction controls volume change and shows two distinct slopes above and below the glass transition (Point d), which may not be present for high T_g polymer networks whose T_g often exceeds the ultimate cure temperature. While chemical shrinkage is often considered in manufacturing, standard practices only examine initial and end states.¹⁶ From this schematic, it becomes obvious chemical shrinkage causes a significant volume change which is largely ignored when considering only initial and end states. Several studies suggest chemical shrinkage scales with conversion, depending only on final conversion regardless of cure path.¹⁶⁻¹⁹ We hypothesize volume changes of the matrix in the solid state due to chemical shrinkage can have significant contributions to cure-induced strains within composite laminates.

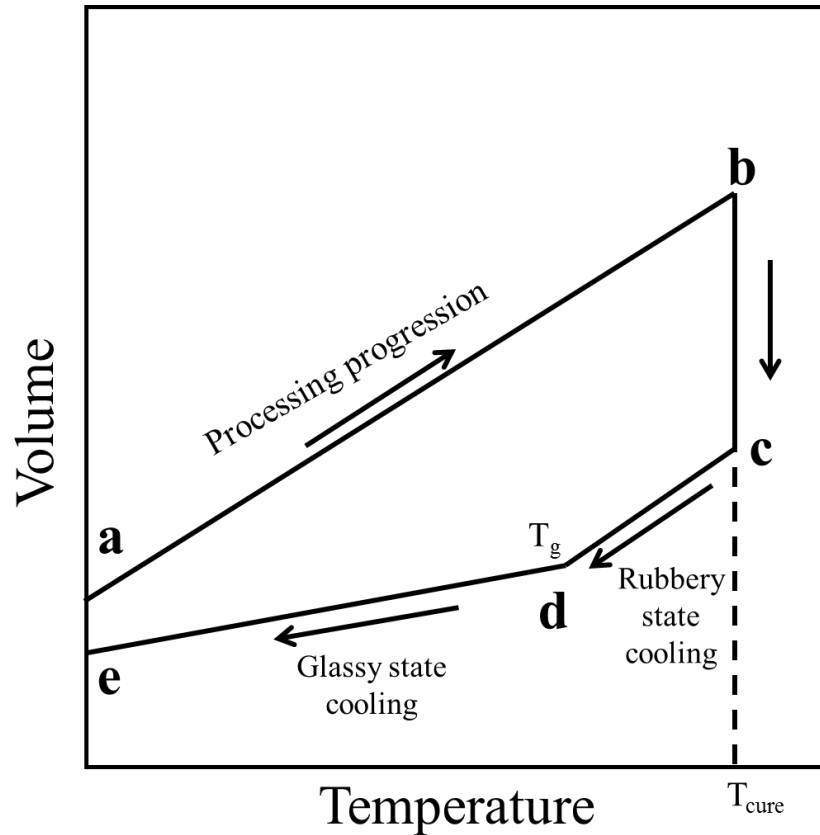


Figure 1.1 Volume changes of a thermoset polymer network during cure.

1.2.1.2 Coefficient of Thermal Expansion

Polymers behave like most traditional structural materials in that upon heating they undergo volumetric expansion. Upon heating, polymer chains may adopt conformations otherwise energetically unfavorable, undergoing glassy state molecular motions at increasing frequencies. In linear polymers, this is accompanied by a decrease in end-to-end distance; however, this does not correspond with a decrease in volume. Rather, individual chains are able to occupy more space due to local chain motions.

The coefficient of thermal expansion (CTE) describes the volumetric changes a material exhibits as a function of temperature. In polymeric materials, CTE varies greatly with temperature, with significant changes in its values occurring at state transitions, such

as the glass transition. As temperature increases, polymer chains increase in mobility and thereby occupied volume.^{20,21} Polymer glasses will have varying CTE values depending on their chemical structures and connectivity. In heating through T_g , CTE changes significantly, with greater expansion occurring in the rubbery state, as a function of temperature. It has been suggested rubbery state CTE is strongly influenced by the stiffness of individual polymer chains, whereby increases in chain stiffness correlate with decreases in CTE.²² CTE can be expressed in one, two, or three dimensions. Linear (1D) and volumetric (3D) are most commonly reported, and save for a few specialty polymers with a high degree of chain alignment, expansion is isotropic. There are a number of methods used to calculate CTE including thermomechanical analysis (TMA), dilatometry, and simulation.

There has been a significant amount of work investigating the CTE of various glassy polymers, particularly for applications with complex interfaces of multiple materials as is the case in optics,²³ electronics,^{24,25} and coatings.^{13,26,27} There has been significantly less work, however, investigating the specific molecular contributions to CTE. A common method for CTE prediction incorporates the Grüneisen theory of solids, which is based solely on a material's atomic structure and interatomic interaction potentials. This theory assumes that CTE arises from atomic vibration around each atom's energy minima (i.e. zero temperature), and takes only the first-term non-harmonic corrections to the harmonic potentials into consideration. In the case of amorphous polymer glasses, which are in a non-equilibrium state, molecular dynamic simulations have shown local chain relaxation processes account for the majority contribution to the glassy state CTE.²⁸

In a composite laminate, the observed or effective CTE is dependent on the properties of both the fiber and matrix. The CTE of carbon fiber is low compared to the matrix, and also varies depending upon the fiber grade and the direction (longitudinal vs. transverse).²⁹ Timmerman et al. report that the longitudinal CTE of the fiber is negative and decreases with increasing Young's Modulus due to variations in fiber morphology.⁴ Conversely, the CTE in the transverse direction is positive and of greater magnitude.^{1,30} In a composite laminate, the large differential in matrix and fiber CTEs creates complex interfacial strain states within the matrix.³¹ Differences of CTEs in dissimilar materials have been studied through the incorporation of additives/reinforcements in polymers including carbon nanofibers,^{32,33} carbon nanotubes,³⁴ hyperbranched polymers,³⁵ and polyhedral oligomeric silsesquioxane (POSS),^{24,36} with general conclusions that low-CTE additives/reinforcements decrease the effective CTE of the matrix. Since CTE of the matrix in composite laminates is a dynamic property that varies during cure, it becomes difficult, if not impossible to measure in-situ since volume changes associated with thermal expansion are confounded with chemical shrinkage. Consequently, simulation and theoretical models which describe the evolution of CTE with cure currently serve as the most reliable predictive measures.³⁷⁻³⁹ Although it has been shown that chemical shrinkage significantly contributes to cure-induced strains,⁴⁰ Olivier and coworkers suggest cooling in the glassy state is responsible for the majority of residual strains imparted during the processing of carbon fiber-epoxy laminates.²

1.2.1.3 Gelation and Vitrification

Gelation and vitrification are critical points which define the polymerization of amorphous glassy polymer networks and serve as important variables for consideration of the development of cure-induced strains in thermoset matrix composites. Chemical gelation is the point in the polymerization when a continuous network of infinite molecular weight is observed, and theoretically, all monomers are connected through covalent bonds. At the point of gelation modulus and viscosity undergo a significant increase.⁴¹ As a result of gelation, the polymer irreversibly transforms from a liquid to a rubbery solid; the specific degree of conversion at which this occurs is referred to as the critical gel-point.⁴¹ Gelation can be determined via rheology as the crossover point of the shear storage modulus, G' , and the shear loss modulus, G'' , as well as the intersection of $\tan\delta$ curves generated at multiple testing frequencies.^{42,43} Gelation marks the onset of strain creation as the polymer begins to develop mechanical strength and integrity.^{17,35,40,44} In this pre-vitrified rubbery state the relaxation moduli and relaxation times are sufficiently low to allow strain relaxations to occur.^{2,26,40}

Vitrification occurs when the glass transition temperature, T_g , exceeds the cure temperature, T_{cure} , transitioning the polymer from a rubber to a glass.^{10,45} Vitrification differs from gelation since it is a reversible transition. Devitrification occurs as the polymer's temperature exceeds its instantaneous T_g . This phenomenon may repeatedly occur for a polymer matrix during the heating ramp stage of a composite cure.⁴⁵ Vitrification is dependent on time and temperature and can occur at varying degrees of conversion depending on T_{cure} , as described in Gillham's Time-Temperature-Transformation diagram for isothermal cure.⁴⁶ Analytical techniques employed to

quantify vitrification/devitrification behaviors include modulated differential scanning calorimetry and dielectric spectroscopy.^{45,47}

Prior to vitrification, reaction kinetics are dependent on temperature, while beyond vitrification in the glassy state, reaction kinetics are measurably reduced and become diffusion controlled. The matrix undergoes several changes at this point. For example, vitrification marks measurable increases in Young's, shear and bulk moduli, which in turn correspond with increases in relaxation times.^{40,46,48} For this reason, it is assumed that strain relaxation ceases upon vitrification.⁴⁹ Due to high values of moduli upon vitrification, additional polymerization and network formation imparts strain as the matrix continues to cure.²

1.2.1.4 Cure-induced Strain Measurement Methods

Techniques for quantifying cure-induced strain within continuous fiber polymer matrix include thermal mechanical analysis,² interrupted cures with non-symmetric laminates,^{5,12} strain relief through incremental hole-drilling,⁵⁰ fiber optical sensors,⁵¹⁻⁵³ Raman spectroscopy,⁵⁴⁻⁵⁶ and the use of strain gauges.^{12,57} A widely accepted method has been quantifying geometrical deformations observed in composite panels before and after cure. This method has several variations including a balanced and symmetric [+45/0/-45/90]_s 90° "L-shaped" laminates, where geometrical deformations are measured through angle deviation from the molded-in 90° interior angle.⁵⁸⁻⁶⁰ Another sample geometry includes the measurement of balanced, non-symmetric [0_x/90_x] flat panels which develop curvature upon curing.^{61,62} All methods mentioned here have limitations, and/or require considerable assumptions. Many techniques must be conducted out-of-autoclave, or without the vacuum bagging process. These contribute significantly to laminate

compaction, and therefore macroscale constraints which may influence strain development. Other techniques require significant assumptions by the user. For example, fiber optical sensors can give sizeable strain measurements prior to gelation, while the matrix exists in primarily a liquid state, while the occurrence of gelation is not accompanied by a measurable signal.⁵¹ This requires the user to make assumptions regarding the beginning of measurement validity or the zero point from which strain measurements are referenced.

Whilst research on residual strains has acknowledged the importance of polymer volumetric properties, as well as the physical state changes brought about by gelation and vitrification, there is a void in the knowledge base of how the polymer matrix develops, stores, and relaxes strains throughout the elevated temperature curing process. To increase the knowledge base, additional research efforts are necessary regarding strain performance of glassy amorphous polymer networks which are employed as high-performance composite matrices. A deepened understanding of strain development and relaxation is critical to capture the polymer properties which define composite processing properties and performance.

1.2.2 Strain Development and Polymer Deformation

1.2.2.1 Onset Theory

While polymer dynamics in solution have been relatively well-described by the scientific community for several decades, the melt and solid states persist as a somewhat contested area of research. This is due to a number of reasons including increased timescales of relaxation processes and convolution of intramolecular and intermolecular interactions. Despite the challenge, understanding mechanisms and events which govern

composite matrix failure modes is of specific interest to the composites science and engineering communities. Researchers at The Boeing Company developed a theory to accurately predict composite failure through analysis of invariant strain values at critical locations within a composite laminate.⁶³ Onset Theory focuses on the prediction of both matrix critical and fiber critical strain invariants and suggests failure will initiate when one component reaches a critical value during a deformation event. A composite structure is typically only able to realize 40% (or less) of the fiber's theoretical load capability. This brings Onset Theory to propose the properties which control damage initiation within a lamina are the effective volumetric and equivalent strains of the polymer matrix. Mechanical deformation of the matrix under uniaxial compression allows for calculation of a yield strain, from which the equivalent strain may be calculated.⁶⁴

1.2.2.2 Yield

Traditional definitions of yield consider it to be the onset of plastic (permanent) deformation, often termed viscoplastic flow. The yielding deformation process is the mechanical analogue to long-range segmental motions or “flow” which constitute the glass transition.⁶⁵ Under high applied stresses, the polymer deforms via a number of behaviors to store or dissipate stress, shown in Figure 1.2. At small strains, glassy polymers deform in a linear viscoelastic manner. The slope of the curve, i.e. the elastic modulus, will vary depending on the deformation rate and temperature due to the viscoelastic nature of polymers;⁶⁶ however, strains are fully and instantaneously recoverable. Beyond the small strain regime, glassy polymers follow nonlinear viscoelastic behavior prior to yield. As applied stresses continue to increase, the yield point is approached. The yield point is often identified as a local maximum preceding

strain softening, or a “stress-drop” in the stress-strain curve.⁶⁴ While it is common for linear glassy polymers to show strain softening, this is not always the case with glassy polymer networks. As shown in Figure 1.2, the stress-strain curve may plateau rather than reach a local maximum, making accurate determination of a yield point from a stress-strain curve problematic.

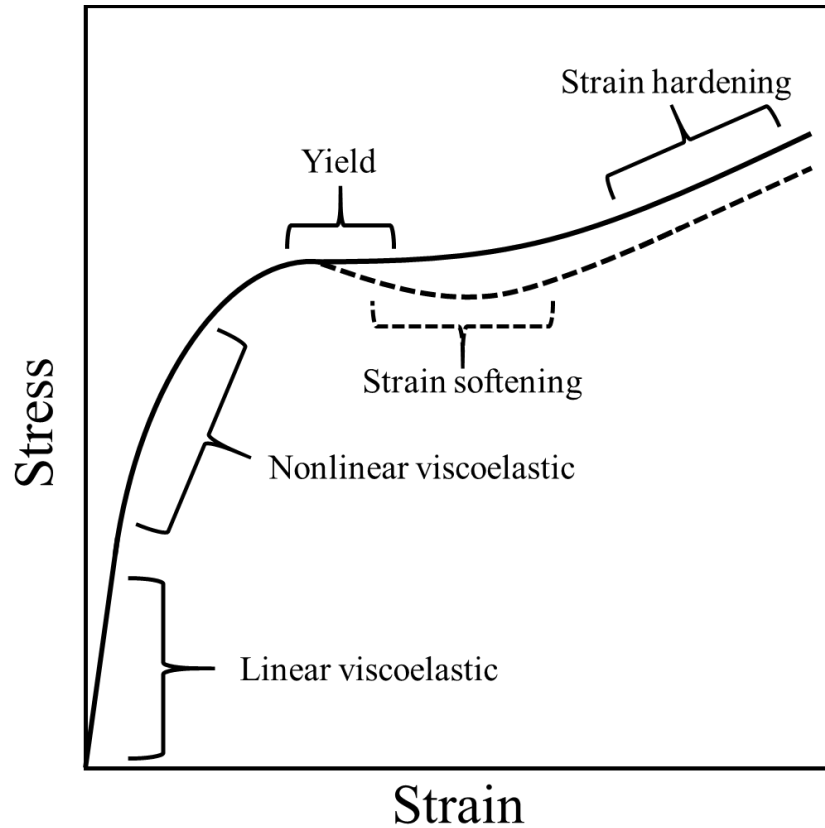


Figure 1.2 Deformation behaviors of polymer glasses.

Typical deformation behavior is shown with and without strain-softening behavior, shown in dashed and solid curves, respectively.

As simulation of composite properties proliferates as a materials research tool, accurate identification of the yield behavior in polymer networks continues to receive significant interest.⁶⁷ Advanced techniques such as digital image correlation (DIC) have aided in the accurate characterization of key polymer properties. A distinct advantage to

non-contact methods such as DIC is the removal of erroneous measurements due to fixture or equipment compliance. Previous work in our group has shown sizable differences in Young's modulus and yield strain calculations between DIC and traditional linear variable differential transducer (LVDT) measurements due to increased sensitivity.⁶⁴ Beyond this, DIC has proven useful in other complex strain measurements environments, such as fluid ingress and strain recovery of glassy polymers.^{68,69}

When the stress-strain curve does not exhibit a clear local maximum, the offset method can be used. In this, the yield point is taken by the intersection of the stress-strain curve with an offset line of equal initial slope. The placement of this line is traditionally offset on the strain axis by a specified strain, commonly 0.2%. It is assumed deviation of the stress-strain curve from linearity corresponds with yield-type deformations, and upon unloading the polymer will undergo linear elastic recovery along this line.⁷¹ A number of researchers have shown the recovery behavior of polymers is nonlinear due to anharmonic, but recoverable deformations.^{72,73} Therefore, the true yield point is better identified by residual strain measurements, where the yield stress is the smallest stress value that gives a nonzero residual strain. Although advanced techniques such as DIC aid in measurement sensitivity and accuracy, the relationship of yield behavior with molecular relaxations is not well understood.

1.2.2.3 Deformation Theories

A number of theories exist regarding yield behavior during polymer deformation. Some of the earliest theories, such as that developed by Eyring, are based on transition states. The Eyring theory suggests that under sufficient applied stress, the activation barrier will be overcome and a deformation will occur within a shear stress activation

volume.⁷⁴ For example, a kink in a polymer chain will jump to an available hole. A similar theory developed by Argon suggests thermally-activated local molecular kinks are achieved once an applied stress field creates the activation free enthalpy to overcome the intermolecular energy barrier.⁷⁵ These theories have shown success in yield prediction of glassy materials with consideration of temperature and strain rate. Duckett et al.⁷⁶ made some key improvements to the Eyring model including:

1. The difference in glassy polymer yield behavior in tension vs. compression is due to the hydrostatic pressure component.
2. The rate dependence of yield can be described by an effective polymer viscosity, which is dependent on pressure, temperature, and shear stress.
3. A modified Williams-Landel-Ferry (WLF) equation can relate yield behavior to low strain viscoelastic behavior.

Applied stresses can be separated into a hydrostatic component, relating to volume change (dilation), and a deviatoric component which relates to shape change (distortion).⁷⁷ Polymers are intrinsically ductile, though their deformation behavior depends highly on testing methods. For example, in tension, many glassy polymers experience brittle fracture prior to yield, while in compression the polymer deforms with increased ductility and may undergo yield-type deformation. A tensile stress applies a negative hydrostatic stress (pressure), causing many rigid polymers to tend towards cavitation prior to yield.⁷⁸ This cavitation process serves as the onset of fracture and in many cases causes brittle failure preventing the necking behavior observed by more flexible polymers in tension. If a positive hydrostatic stress is applied to a glassy polymer in tension, for instance by testing in a pressure chamber, cavitation can be suppressed

during deformation. This allows for increased ductility and often results in the necking phenomenon observed in rubbery materials. In compression, however, the hydrostatic component of the stress tensor is positive, allowing deformation to proceed in a more ductile manner.

Other theories take into consideration the free volume available to the polymer under deformation. The model developed by Rusch and Beck proposes that polymers will respond to an applied stress as if it were at an “effective” temperature, which takes into consideration testing temperature, free volume, and changes in CTE with temperature.⁷⁹ This model better fit the temperature and strain rate dependence of polymethyl methacrylate (PMMA) yield behavior when tested across a broad range of each.

Glassy amorphous polymers exhibit not only reversible elasticity, but also partially recoverable plasticity, or anelastic behavior. Even well beyond the onset of plastic deformation, polymers are able to recover significant imparted strains upon load release. The amount of recoverable strains will depend on the deformation conditions, such as loading/unloading rate and temperature. Heating the polymer above the deformation temperature, to near its T_g , enhances molecular mobility and reduces internal friction, which in many cases leads to complete strain recovery.⁸⁰ At temperatures near the deformation temperature, however, they will retain their deformed shape for prolonged time periods, if not indefinitely. While many theories for polymer yield exist, a general model that applies to all materials has not been realized.⁸⁰ An ideal complete theory will include considerations to the transition state and free-volume theories, athermal yielding process, and the cooperative motion (chain cooperativity) process.

1.2.2.4 Deformation Mechanisms of Amorphous Glasses

Under applied load, polymers respond through several relaxations (energy dissipation) mechanisms which can be categorized as elastic, anelastic, and plastic deformation. Assigning specific molecular motions to each mode remains poorly understood, though some generalizations can be made. Elastic strains are effectively instantaneously recoverable, consisting of very small motions (i.e. bond bending, wiggling, small rotations, etc.). Anelastic strains are recoverable with sufficient time and/or temperature (below T_g), and are thought to correlate with sub- T_g transitions observed in rheological and spectroscopic studies such as dynamic mechanical analysis (DMA) and dielectric analysis (DEA), and solid-state NMR spectroscopy.⁸¹ Plastic strains are only recoverable at or near T_g , if the material's "memory" was not destroyed during the deformation (as can be the case with linear polymers).⁸⁰

Glassy amorphous polymer networks under mechanical loading are subjected to significant stress fields. This energy can be stored or dissipated within the glass, or released as heat. Numerous molecular relaxations are responsible for energy absorption and dissipation of a polymer experiencing a deformation event. Under high stresses, the distribution of activated molecular motions likely far exceeds the short range motions which can be probed or elucidated through the aforementioned rheological and spectroscopic characterization methods. A number of studies have correlated sub- T_g molecular motions to bulk mechanical properties of glassy amorphous polymers.⁸¹⁻⁸⁵ Extensive work has been performed to elucidate the size and cooperativity of specific motions responsible for secondary relaxation processes of glassy materials ($T < T_g$) through dynamic mechanical and spectroscopy studies, such as solid state nuclear

magnetic resonance (NMR) and dielectric spectroscopy (DS).⁸⁶ These secondary relaxation processes are partially responsible for mechanical and dielectric properties of polymers in the glassy state; however, assignment of specific molecular motions to mechanical deformations remains a disputed topic.^{81,86} For instance, it has been argued that certain sub- T_g motions such as ring flipping are not mechanically activated, as the polymer chain conformation undergoes no net change.⁸⁷ Ring flipping, side group motions, and other short-range processes may interrelate with additional processes that hold direct mechanical and dielectric roles.⁸⁶⁻⁸⁸

Testing conditions, such as the temperature at which a polymer is deformed, have drastic effects on the deformation performance. For example, testing a material at temperatures below T_g corresponds with an increase in Young's modulus at the expense of deformation processes which govern strain at yield and/or break.⁶⁵ As previously mentioned, the theory by Rusch and Beck suggests that in polymers the dependence of mechanical performance on temperature stems from free volume, where free volume alters the statistical mechanics of energy dissipation.⁷⁹ Polymer systems with increased free volume, therefore, may exhibit increased anelastic deformation components, attributed to available free volume allowing increased segmental motions. This theory has been supported by studies involving DGEBA network isomers which differ significantly in average free volume hole size and density.⁶⁹

Connecting the dependence of molecular mobility with deformation is a considerable barrier to understanding the deformation mechanisms of amorphous polymer glasses. The activation of molecular motions with deformation is complex, and motions are likely highly interdependent. Certain polymer glasses are known to undergo

stress-induced acceleration of thermally-activated cooperative relaxations, thus molecular mobility changes with deformation as local chain segments experience a variety of strain states.⁸⁹ Lee et al. showed increases in mobility upon stress application in lightly crosslinked PMMA; however, their investigation showed differences in recovery behavior in single vs. multiple step creep and recovery tests, suggesting changes in segmental mobility by stress application is path dependent.⁹⁰ Therefore stress does not uniquely lead to increases in molecular mobility, and perhaps a single mechanical variable cannot universally relate mobility to deformation behavior due to varying levels of cooperativity. Indeed, the relationship is complicated and makes the development of a generalized model which extends across numerous materials, even material families, quite difficult. Much of the work regarding strain development has focused on linear amorphous glassy polymers. While studies involving model glassy polymers like polystyrene (PS), polycarbonate (PC), polyethylene terephthalate (PET), and PMMA are useful, drawing conclusions which relate deformation behavior to molecular architecture is difficult given their highly dissimilar molecular compositions.

1.2.3 Chain Rigidity and Cooperativity

1.2.3.1 Chain Rigidity

The stiffness or rigidity of a polymer chain has profound effects on its solution and solid state properties.⁶⁵ Properties representative of chain stiffness such as Kuhn length (b), radius of gyration (R_g), and mean-square end-to-end distance (r^2) are commonly characterized for linear polymers in the solution state. As chain rigidity increases, however, polymer properties in solution are less well established, and their behavior deviates significantly from flexible chains which can adopt a random-coil

conformation. For instance, solution-cast films of semi-rigid rod polyethersulfone show significantly different concentrations of chain end at the surface compared to the bulk. Bulk chain end concentration has been shown to lie at a depth near R_g rather than $2R_g$, as seen with more flexible amorphous polymers.⁹¹ This is attributed to chain rigidity hindering mobility during film formation and causes rigid rod polymers to deviate from solution relationships established from flexible linear polymers. In the case of polysulfones, rigidity is derived from the relatively inflexible and immobile phenyl and sulfone groups which make up much of their backbone compositions, and are also common backbone groups in aromatic epoxy-amine networks.⁹² Small differences in chain connectivity have been correlated to sizable differences in thermal, environmental, and mechanical performance of chemically-identical polymers.^{70,93,94} Within the thermoset polymer science community the role of chain rigidity has been studied for a variety of systems ranging from low- T_g thiol-ene networks⁹⁵ to high- T_g , highly aromatic epoxy-amine systems;⁸³ though these studies often simultaneously vary chain rigidity and intermolecular interactions such as hydrogen bonding, which are known to influence cooperative motions. A study which probes the role of chain rigidity without significant alteration of secondary interactions would add value to the polymer science community.

1.2.3.2 Cooperativity of Polymer Glasses

Simply defined, cooperativity is the non-independent dynamics or cooperative movement of chain elements and may describe both intra- and intermolecular interactions. As cooperativity increases, motions of chain elements increasingly correspond relative to a hypothetical system in which the individual elements act independently. Intramolecular cooperativity is believed to be primarily bond rotations,

with large-scale segmental motion avoided by cooperative rotation of neighboring elements along the chain.⁹⁶ Segmental chain motion of dense polymers, such as glassy amorphous networks, is also restricted by intermolecular cooperativity.⁹⁷ This has inspired some researchers to use cooperativity measurements as a tool for evaluation of cure kinetics.⁹⁸ More flexible, tightly packed polymer chains typically exhibit increased cooperativity as molecular motions influence nearby chains. Similarly, polymers which show large changes in enthalpy upon the glassy transition indicative of significant gains in translational freedom are considered more cooperative; however, the temperature of the glass transition does not directly relate to cooperativity.⁹⁹

1.2.3.3 Polymer Fragility

First introduced by Angell in the 1980s, the fragility of a glassy material describes the rate of change of physical properties and dynamics within the relatively narrow temperature range of the glass transition.¹⁰⁰ Dynamic fragility refers to the rate at which a material's relaxation or mass transport behavior (relaxation time, viscosity, fluidity, etc.) changes through the glass transition. Upon cooling a "strong" liquid, dynamic properties maintain a nearly Arrhenius temperature dependence, while a "fragile" liquid will behave nearer a Williams-Landel-Ferry (WLF) relationship.^{101,102} Angell went on to suggest the "universal" C_1 constant of the WLF equation (Equation 1) relates to the dynamic fragility of a polymer.¹⁰³

$$\log a_T = \frac{-C_1(T-T^*)}{C_2+T-T^*} \quad (1)$$

Specifically, Angell showed when T_g is chosen as the reference temperature T^* , C_1 represents the difference (in orders of magnitude) between the relaxation time and the pre-exponent of the Vogel-Fulcher-Tammann equation (Equation 2), which is often used

to explain the temperature dependence of polymer dynamics. A number of authors showed that while C_1 value of 17.4 remained constant across many polymers, the second constant of the WLF equation, C_2 , was much less constant and more likely a polymer-specific structural parameter.^{103,104}

$$\tau = \tau_0 e^{\left(\frac{B}{T-T_0}\right)} \quad (2)$$

Dynamic fragility has historically been represented by mechanical means, and more recently through thermodynamic measurements as $C_{P,l}/C_{P,g}$, where $C_{P,l}$ and $C_{P,g}$ are heat capacity values in the liquid (or rubbery) and glassy states, respectively.¹⁰⁵ The relationship between a thermodynamic fragility parameter, represented by changes in heat capacity at T_g , and the dynamic fragility parameter “ m ” (measured by dielectric or mechanical methods) has been of interest in recent work and remains a topic of dispute within the scientific community. While some authors suggest the two parameters lack any correlation,^{106,107} others have found a negative correlation.^{85,105} McKenna and coworkers suggested a correlation between m and T_g , with polymers sharing an approximately linear increase in dynamic fragility with T_g .¹⁰² Bartolotta and coworkers related dynamic fragility to network connectivity of heterocyclic polymer networks, wherein increased connectivity was accompanied by a decrease in thermodynamic fragility.⁸⁵ They attributed this to decreasing degrees of freedom and configurational entropy with increasing connectivity. Polymer fragility, whether dynamic or thermodynamic, continues to be a research space of interest for the design and simulation of advanced materials.

1.3 Research Overview

The creation of strains through processing and deformation of polymers proceeds through numerous mechanisms, the molecular processes of which continue to be topics of dispute within the scientific community. Testing methods for the evolution of cure-induced strains in processing have not been standardized, limiting the accuracy of property simulation. Similarly, we do not fully understand the molecular structure attributes which dictate strain creation and relaxation in amorphous polymer glasses. Resolving strain storage and dissipation mechanisms is complicated due to confounding intra- and intermolecular factors present with common glassy amorphous linear polymers. While chain rigidity is an intrinsic property which dictates behavior of polymers in the solution and solid state, there is relatively little discussion within the literature connecting chain rigidity to deformation processes in glassy amorphous polymer networks. Further, there is often convolution of intra- and intermolecular factors which limits generalized conclusions regarding the mechanisms of strain storage and relaxation. Chemically-similar epoxy-amine network isomers will be studied in this research to provide a system of materials which exhibit similar intermolecular interactions but differ in chain structure and therefore rigidity. A deepened understanding of the roles of chain rigidity in the formation and performance of glassy amorphous networks will allow the polymer science community to approach the design of next-generation materials more holistically.

The research scope of this dissertation is twofold. In our first approach, the focus of *Chapter III*, we will establish a toolset for accurate measurement of critical matrix and composite properties which govern the creation and relaxation of process-induced strains.

In the second approach, through *Chapters IV and V*, we will elucidate fundamental polymer properties that drive strain creation and recovery in glassy amorphous networks. Ultimately, each of these approaches can be used to further investigate the development and final properties of high-performance polymers and their associated composites.

The subsequent chapters outline our approach to the measurement and quantification of strains in glassy amorphous polymer networks. Specific aims are:

1. Establish testing methods to be used by the science and engineering communities for improved understanding of matrix and composite volumetric properties which control property development and strain creation during composites manufacturing.
2. Investigate the role of network rigidity in the thermal, physical, volumetric, and thermomechanical properties of chemically-similar glassy epoxy-amine networks.
3. Relate network rigidity to mechanical properties and deformation behavior of chemically-similar epoxy-amine networks, with further considerations to the attributing network thermal, architectural, and thermomechanical properties.

CHAPTER II - EXPERIMENTAL

2.1 Materials

A wide range of epoxy-amine systems was investigated in this work, from common two-component polymer networks to highly-formulated, commercially-sold matrix and prepreg systems. Commercial systems were used for studies which compared neat matrix properties with laminate-level responses. CYCOM 977-3 was supplied by Cytec Aerospace Materials in the form of bulk prepolymer matrix and was used without further modification. Composite laminates were built from epoxy matrix prepregs fabricated on our Western Advanced Engineering Company 12" unidirectional hot-melt tape line using Hexcel IM7 unsized carbon fiber. All fabricated panels in this study made use of 190 grams per meter² (fiber weight) prepregs containing approximately 67 wt.% carbon fiber and 33 wt.% matrix.

A number of two-component systems were also investigated, including multiple epoxy prepolymers and amine curatives. The series of epoxy resins included both difunctional and multifunctional materials. For difunctional resins, both diglycidyl ether of bisphenol A (DGEBA, EPONTM 825, 175 gram per equivalent, Hexion Specialty Chemicals Co.) and diglycidyl ether of bisphenol F (DGEBF, EPONTM 862, 165 gram per equivalent, Hexion Specialty Chemicals Co.) were used. The multifunctional resin studied was tetraglycidyl-4,4'-diamino-diphenyl methane (TGDDM, Araldite[®] MY 721, 111-117 gram per equivalent, Huntsman Co.). All epoxy resins were combined with aromatic amine isomer curatives including 3,3'-diaminodiphenyl sulfone (33DDS, 97%, Aldrich Chemical Co.) and 4,4'-diaminodiphenyl sulfone (44DDS, 97%, Royce Chemical Co.). All materials were used as received.

2.2 Glassy Polymer Network Preparation

2.2.1 Preparation of Commercial Matrix Specimens

For studies involving comparison of neat matrix to the associated composite laminates, the as-received commercial prepolymer matrix was heated and degassed at 125 °C (10^{-3} Torr) and cast into silicone molds (internal cavity 130 x 12 x 6 mm) without further modification. It was then cured by the manufacturer's recommended cure cycle (MRCC) (temperature ramp at 1.8 °C/min to 177 °C, 6h isothermal hold).

2.2.2 Matrix Formulation

In a typical reaction, 100.0 g (285.7 mmol) DGEBA epoxy resin was charged to a 125 ml sidearm flask equipped with a vacuum fitting and magnetic stirring device. The epoxy prepolymer was first heated to 100 °C to reduce viscosity and remove residual moisture under applied vacuum at $\sim 10^{-3}$ Torr. At this time 35.45 g (142.85 mmol) of 33DDS or 44DDS micronized powder was incrementally added to avoid agglomeration. Upon complete addition, vacuum was slowly applied to a level of $\sim 10^{-3}$ Torr and the temperature was increased to 125 °C. The mixture was stirred until dissolution of amine was observed, at which time vacuum was removed. The transparent solution was cast into preheated (125 °C) molds. Amine masses were adjusted based on epoxide equivalent weight of the selected epoxide prepolymer to maintain 1:1 stoichiometric ratio of epoxide: amino-hydrogen in all two-component formulations.

2.2.3 Test Specimen Preparation

Following formulation prepolymer, epoxy-amine mixtures were slowly cast into molds and cured by the selected thermal cure profile, listed in Table 2.1. Unless otherwise specified, all non-commercial, formulated networks were cured by the

academic cure profile. A number of specimen geometries were used for the analysis of glassy polymer networks. The mold materials and geometries can be found in Table 2.2. Experiments involving mechanical testing in compression used polymer network cylinders. Upon cooling the cured glassy polymer was precision turned on a lathe into compression test cylinders of 2.0, 1.5, or 1.0 aspect ratio and parallel loading surfaces. Specimens were conditioned for at least 48 hours at 25°C and 50% RH prior to testing. Experiments involving non-contact analysis under heating used polymer network “cubes” approximately 15 mm in height which were manually cut from longer bars. This allowed under-cured, fragile network specimens to be handled and prepared without machining.

Table 2.1

Thermal Cure Profiles.

Name	Thermal Profile
Academic Cure	5 h at 125 °C + 2 h at 225 °C, 1 °C/min ramp
Industrial Cure	3 h at 180 °C, 1 °C/min ramp

Table 2.2

Polymer Network Mold Materials and Geometries.

Mold Geometry	Mold Material	Internal Cavity Dimensions (mm)
Compression Cylinder	PTFE	152.4 x 11.1125
Flexural Bar	Silicone	130 x 12 x 6

2.3 Laminate Fabrication

Prepreg materials were stored in vacuum-sealed containers at sub-ambient temperatures and equilibrated at room temperature prior to use. Flat composite panels (30.48 x 30.48 cm) were fabricated into unidirectional (UD) [0₈], off-axis (OA) [45₄/90₄], and non-symmetric (NS) [0₈/90₈] laminates on flat Invar tools with steel caul plates.

Panels were cured by the manufacturer's recommended cure cycle (MRCC – 1.8 °C/min to 177 °C, 6h hold) in an American Autoclave under vacuum bag and pressure ($\sim 10^{-3}$ Torr and 0.586 MPa, respectively) to fully compact plies and assure void-free laminates. Panels were machined into 2.54 x 7.62 cm coupons using a diamond saw and cutting fluid. Due to non-traditional lay-up sequences, some coupons developed cracks upon machining and were not used. Non-symmetric $[0_8/90_8]$ and off-axis $[45_4/90_4]$ laminates exhibited significant concave curvature with respect to the 90° and 45° face, respectively.

2.4 Analysis

2.4.1 Mechanical Testing

2.4.1.1 Compression Testing

Mechanical testing and strain recovery experiments followed ASTM D695-02a. Epoxy network cylinders were compressed at a displacement-controlled test rate of 1.27mm/min on a MTS Systems Corporation Model 810 servo-hydraulic universal test frame. Compression under uniaxial load was ensured using a low friction compression sub-press (Wyoming Test Fixtures Model CU-SP). Axial displacement was measured by the test frame's linear variable differential transformer (LVDT) and load was measured using a MTS 100 kN load cell. MTS TestWorks[®] software recorded load and displacement data at a sampling rate of 10Hz. The secant modulus was taken from 0.5 to 1.0% LVDT-derived global strain measurements and reported as an average of no fewer than five specimens. Elevated temperature testing was performed in an air atmosphere using an environmental chamber. Samples were allowed to equilibrate at temperature for 5 minutes prior to testing.

2.4.1.2 Tensile Testing

Tensile testing was performed on all two-component epoxy network cylinders at elevated temperatures. ASTM D638 Type IV tensile bars were mounted in wedge grips and placed under uniaxial tension at a displacement-controlled test rate of 1.27mm/min on a MTS Systems Corporation Insight electromechanical universal test frame fitted with an environmental chamber. Axial displacement was measured by the test frame's LVDT and load was measured using a MTS 100 N load cell. MTS TestWorks® software recorded load and displacement data at a sampling rate of 10Hz. The secant modulus was taken from 0.5 to 1.0% LVDT-derived global strain measurements and reported as an average of no fewer than three specimens.

2.4.2 Thermal Analysis

2.4.2.1 Differential Scanning Calorimetry

Differential scanning calorimetry (DSC) experiments were conducted using a Thermal Analysis (TA) Q200 differential scanning calorimeter. Sample mass ranged from 3 to 7 mg in hermetic aluminum pans. Nitrogen was used as purge gas and Indium and Sapphire were used as temperature and enthalpy calibrates, respectively. Heat-cool-heat cycles at a constant heating rate of 10 °C/min were used in order to determine the glass transition temperatures (T_g) of the glassy amorphous network series. To determine T_g value and breadth, the derivative of heat flow with respect to temperature was taken using a linear least squares fitting method over 10 °C intervals. T_g was assigned as the peak of this curve, which aligns with the traditional endothermic step observed during the second heating cycle of cured materials. This value aligned very closely (within 1 °C) to the T_g value by the inflection point method. The breadth of the glass transition was taken

using the full-width-half-height measurement of the derivative peak. No significant differences were observed between the second and third heating cycles of the fully-cured networks.

Calorimetry experiments of deformed samples used small, precision turned cylinders with parallel top and bottom faces and an aspect ratio of 1.0 due to height constraints within the cell (approximately 4mm height and diameter, mass range 50-70 mg). This allowed entire deformed specimens to be placed within the DSC cell, negating the need to cut or machine samples for calorimetric strain recovery measurements. This also allowed the same cylinder to be retested after each trial, during which complete recovery of stored strains was realized. To limit changes in heat capacity due to contact area with the sidewalls of testing pans, inverted hermetic pans were placed over the reference and sample platforms. Cylinders were compressed in uniaxial compression following the same procedure previously described, using a MTS Systems Corporation Insight electromechanical universal test frame equipped with a low friction compression sub-press. LVDT compression data was recorded from MTS Testworks® software using a MTS 10 kN load cell at a sampling rate of 10 Hz. A heat-cool-heat-cool-heat procedure allowed for the observation of strain recovery and subsequent baseline single heat cycles with a temperature ramp of 10 °C/min.

2.4.2.2 Thermogravimetric Analysis

Thermal stability of cured amorphous networks was determined using thermogravimetric analysis (TGA). Experiments were performed using a Thermal Analysis (TA) Q50® instrument, platinum pans, and nitrogen purge gas. Approximately 10 mg of each glassy epoxy network was heated at 2 °C/min to 400 °C. The degradation

temperature was identified by the onset point of sample weight with respect to temperature at the occurrence of at least 5% weight loss.

2.4.3 Thermomechanical Testing

2.4.3.1 Rheology

Parallel plate rheological experiments were conducted to determine the gelation point of uncured resin systems on a Thermal Analysis (TA) ARES-G2 rotational rheometer using 8mm aluminum plates with a 0.3 mm gap and frequency of 1 Hz. The development of the shear storage (G') and loss (G'') moduli as well as complex viscosity (η^*) were observed as the systems were heated using select thermal profiles. The gelation point was defined by the crossover of G' and G'' curves.

2.4.3.2 Thermomechanical Analysis

Thermal expansion/contraction properties of cured amorphous networks and composite laminates, as well as thermal strain recovery behavior of deformed polymer networks, were determined using thermomechanical analysis (TMA). Cured matrix cylinders approximately 20 x 10 mm were precision turned and sanded for parallel top and bottom faces. Due to an instrument maximum measurement range of 3.4 mm, cylinders with an aspect ratio of 1.5 (i.e. 12 x 8 mm) were used for strain recovery experiments. Specimens were heated at 2 °C/min with a 0.05 N force using a Thermal Analysis (TA) Q400[®] instrument fitted with a quartz stage and macro expansion probe. Linear coefficients of thermal expansion were determined by the slope of a linear fit to sample length vs. temperature curves from 50-100 °C. T_g measurements were taken by bilinear fit of the sample length vs. temperature curves above and below the “knee” at T_g . Laminate measurements were taken parallel and perpendicular to the fiber direction (0°

and 90°, respectively) using 1 x 1 cm specimens, and heated at 1 °C/min from 25 °C to 177 °C.

2.4.3.3 Dynamic Mechanical Analysis

Dynamic mechanical analysis (DMA) experiments were conducted using a Thermal Analysis (TA) Q800 dynamic mechanical analyzer fitted with tension clamps. Samples dimensions were approximately 20 x 5 x 0.8 mm, cast from degassed, homogeneous epoxy-amine mixtures. Samples were heated at 2 °C/min from -130 to 275 °C using strain amplitude of 0.05% and a loading frequency of 1 Hz. For activation energy calculations, frequencies of 0.1, 1, 10, and 100 Hz were used. Storage modulus, loss modulus, and loss tangent ($\tan \delta$) were recorded as a function of temperature. Peak analysis was performed with Origin 8.6 plotting software.

2.4.4 Density Testing

The densities of the epoxy networks were determined using the hydrostatic weighing method, in which the mass of a specimen was recorded in and out of deionized water. The Archimedes' principle was then used to calculate density at room temperature and atmospheric pressure. The specimens were machined cylinders identical to those used in compression testing, which were carefully inspected to ensure lack of internal voids or bubbles, as well as smooth, homogenous surfaces. Density was calculated using the following equation:

$$\rho = \frac{m_{dry}}{m_{dry} - m_{immersed}} \times \rho_{water} \quad (3)$$

where m_{dry} is the mass of the specimen prior to immersion, $m_{immersed}$ is the weight of the specimen in deionized water, and ρ_{water} is the density of the deionized water. An average of 5 measurements is reported.

2.4.5 Digital Image Correlation

A unique digital image correlation (DIC) procedure was used in this research, which will be discussed at length in the subsequent chapter. Here we will describe our basic procedure for measurement and image analysis.

2.4.5.1 Digital Image Correlation Measurement

Digital image correlation was conducted using a GOM Optical Measuring Techniques ARAMIS 3D Deformation Analysis System (Trilion Quality Systems). Digital grey scale images were captured using two 2M digital CCD cameras equipped with 50mm lenses at a frame (capture) rate of 1 frame per minute, creating a set of two images upon each capture. Specimens were speckle coated to create a non-uniform surface pattern using white and black aerosol paints with a black solid basecoat and white speckles in a controlled airflow environment, allowing for control of the speckle size within an appropriate range of 2-5 pixels.¹⁰⁸ Prior to testing, the capture volume was calibrated using a manufacturer-provided 25mm x 20mm calibration panel. The calibration procedures performed obtained a resolution deviation of less than 0.03 pixels.

2.4.5.2 Image Analysis

In this work, digital images were taken through a series of steps prior to strain computation to increase accuracy and decrease computation time. First, image processing and strain analysis areas were defined through use of an image mask, effectively reducing image sizes. A start point was then defined for the initial image set, taken prior to sample deformation. The start point was not used as a reference for deformation calculations, but solely as a seed for recreation of the facet field in each image set.¹⁰⁹ A facet size of 15 x 15 pixels with a 13 pixel step length were used in all experiments. Facets are computation

elements which are combined to generate a grid patterns across the defined image areas, while step length is the distance between adjacent facet centers.¹¹⁰ During computation, the grey scale speckle pattern was tracked within each facet from image set to image set. Deformation was calculated from a three-dimensional displacement gradient tensor field based on the change in facet coordinates with respect to the facet center. Strain tensors were calculated from this displacement field, allowing for strain distribution profiles within the facet field.^{111,112} Major strain was the selected visualization in all experiments, though the user may select from numerous visualizations based on the displacement field including major strain, minor strain, and X, Y, and Z direction displacements.

CHAPTER III - THERMAL AND VOLUMETRIC PROPERTY ANALYSIS OF
POLYMER NETWORKS AND COMPOSITES USING ELEVATED
TEMPERATURE DIGITAL IMAGE CORRELATION

3.1 Introduction

Molecular-level strains are introduced within the matrix due to volume changes during the manufacturing of continuous fiber composite laminates, and lead to a number of failure modes including geometry deformation, matrix micro-cracking and ply delamination, among others.³⁻⁵ The sources of these strains are complex, ranging from material properties to processing factors such as tooling material or autoclave thermal gradients; however, a clear consensus exists that dominant contributing factors include a differential in the coefficients of thermal expansion (CTE) between the matrix and reinforcement and, to a lesser extent, matrix chemical shrinkage. Understanding the magnitude of these contributing factors, as well as any potential areas for control, is critical for material and process qualification.

The basics of strain creation within a composite material involve constraints placed on volume changes of the matrix by the fiber environment. The community agrees that a strain cannot build until the matrix has developed an appreciable mechanical strength; a number of authors have shown that, in the processing of thermoset networks, strain creation begins on gelation.^{2,3} In this rubbery state, however, strain relaxation is significant, and molecular segments are able to rearrange to dissipate energy.²⁷ As molecular weight continues to build throughout cure, the polymer network's ability to realize these cooperative motions decreases until the point of vitrification, at which point continued reaction slows drastically and a number of network properties significantly

change. For example, vitrification marks measurable increases in Young's, shear and bulk moduli, and increases in moduli correspond with increases in relaxation times.⁴⁶ For this reason, it is assumed that strain relaxation ceases upon vitrification and this corresponding temperature is often denoted as the strain-free temperature.^{40,48,49} Due to high values of moduli upon vitrification, additional reaction and bond formation imparts strain as the matrix continues to cure, and may also increase the strain-free temperature.² From this glassy state, the material still must undergo cooling from the cure temperature to room temperature. This corresponds with a significant change in matrix volume inducing sizeable thermal residual strains, which are considered to be the largest contributors to process-induced strain within composite materials.⁵¹

Due to the multifaceted mechanisms of strain creation, the measurement of residual strains is complex. While tools such as classical laminate theory allow for the calculation of residual strains based on constituent material properties, techniques which directly measure the strains are not common. Unlike more established polymer analysis techniques, there is a lack of consensus within the community to a preferred method to measure or represent the magnitude of strains. In-situ strain measurement devices such as Fiber Bragg grating sensors and strain electric gauges involve uncertainties as to when the measurement becomes valid during the cure due to the developing interface between the part and the sensor.⁵¹ Other techniques, such as dynamic mechanical or thermomechanical analysis, measure laminate dimension changes or developing mechanical strength of uncured laminates throughout the curing process; however, these do not represent the true manufacturing environment for high-performance composite laminates.^{2,113} Because of the implications of in-situ techniques, comparison of laminate

geometry in uncured and cured states continues to be a common method for researchers. In this, process-induced strains are examined through either curvature reduction of an angled part or by the introduction of curvature upon curing a flat laminate of a non-symmetric laminate sequence. In each scenario, it is understood that the magnitude of residual strain relates to the deviation of mold geometry. In the case of an angled tool, a decrease in interior angle also called “spring-in,” corresponds to an increase in residual strain within the laminate. Conversely, the creation of curvature upon the curing of a flat, non-symmetric laminate is also related to the magnitude of residual strain, wherein increased curvature corresponds to increased residual strain. These techniques are based on measurements made before and after laminate curing. This limits the knowledge of process-induced strain development to an initial (prior to curing) and final (after curing) conditions. We believe heating cured laminates to elevated temperatures provides additional insight into the residual strain state and offers an additional response to laminate deformation. Further, we show that a single experimental setup can be used for accurate measurement of critical matrix properties which serve as the contributing factors to process-induced strains within continuous fiber composite laminates.

Elevated temperature digital image correlation has found application in a number of research areas including high-temperature deformations,¹¹⁷ thermally activated shape memory polymers,¹¹⁸ calculations of Poisson’s ratio for soft materials,¹¹⁹ and the coefficient of thermal expansion for thin films.¹²⁰ Using elevated temperature digital image correlation, the expansion behavior of cured matrix and laminates can be accurately measured for key insights into their volumetric properties. Further, as laminates are heated to elevated temperature, process-induced residual strains are

relieved, and this response can be captured via DIC. The expansion behavior, as well as reduction of laminate deformation, each relate to thermal residual strains and are critical for material and process qualification. The temperature at which all residual strains have been relieved is known as the strain-free temperature, which directly relates to the magnitude of process-induced strains and is also used in composite failure models.⁶³ In this work, we propose differences in thermal expansion and deformation between various lay-up sequences as means to probe the internal strain state of composite laminates.

3.2 Elevated Temperature Digital Image Correlation

Specimens were speckle coated to create a non-uniform surface pattern using high-temperature white and black aerosol paints with a black solid basecoat and white speckles in the appropriate size range of 2-5 pixels.¹⁰⁸ In the case of composite laminates, a basecoat was not necessary. Digital gray scale images were captured via two 2M digital CCD cameras equipped with 50mm lenses. In this setup, the DIC cameras were placed squarely and level in front of a Memmert UF55 Plus laboratory oven fitted with a glass window. Placement of the cameras was chosen such that the camera span, camera angle, measuring distance, and viewing angle were appropriate for elevated temperature experiments. A camera angle of 11.8° was chosen for optimized lighting and minimal glare through the laboratory oven window. This is a decreased angle from previous DIC procedures used in our group and limits the computable surface map due to sample curvature. Furthermore, increased camera angles can degrade image quality due to light distortion by the oven glass. This effect could be limited through use of optical grade glass for the oven window. In this case, sample curvature was very minor, making a small

camera angle, or even use of a single camera (2D DIC), sufficient for our procedures. Dark, non-reflective backboards were placed behind the cameras to further reduce glare. Camera calibration was performed using a 25mm x 20mm standard placed within the oven (at ambient temperature) to obtain a resolution deviation of less than 0.03 pixels. Images were taken through the glass door throughout the calibration procedure. To improve lighting conditions, the lens aperture was opened to the maximum, and shutter speed was increased to approximately 120 ms. During the heating event, images were taken at a frame rate of 1 image per minute to align with the oven temperature ramp rate of 1 °C/min. Camera orientation relative to the sample within the oven is shown in Figure 3.1.

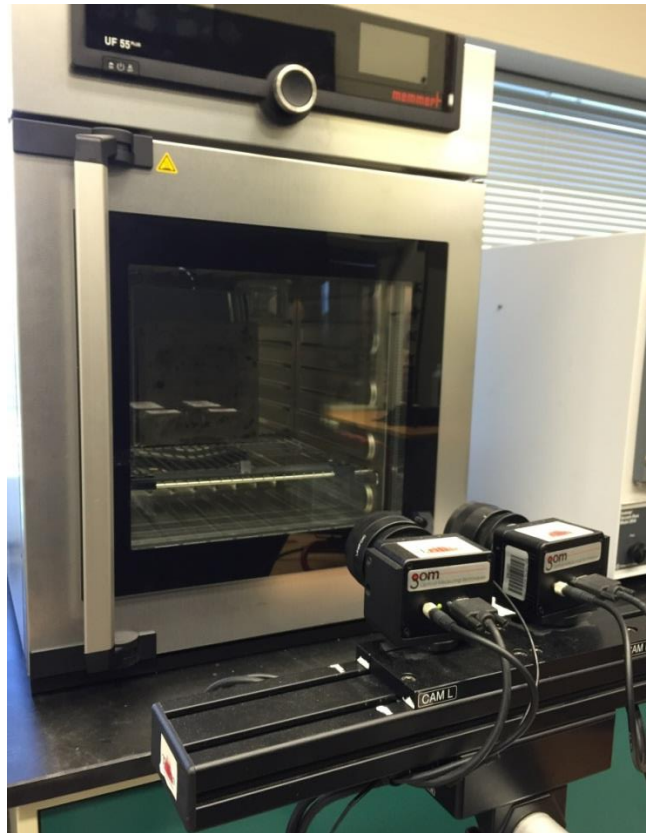


Figure 3.1 Camera orientation for elevated temperature DIC.

3.3 Results and Discussion

3.3.1 Chemical Shrinkage

A unique benefit to DIC techniques, including its attendant software, is the ability to calculate numerous responses from a single series of images. While DIC is typically used as a full-field strain measurement technique, the ARAMIS software also provides analytical reference tools, known as “primitives” related to the computed surface maps, including points, lines, planes, best-fit shapes, etc. These tools can be used to track dimension changes from image to image. Line lengths calculated along the surface map can be used for analysis of sample expansion or contraction throughout the image series. In this work, five lines whose lengths were nearly equal to the sample’s height (approximately 13.6 mm) were created. Maximum line lengths were found to reduce the noise associated with the measurement. Length changes were then tracked from the first image prior to heating (L_0) through the MRCC. In this case, a maximum heating rate under the MRCC (2.8 °C/min) was chosen to limit the convolution of chemical shrinkage with thermal expansion. The average change in line length is plotted in Figure 3.2. Initially, the partially-cured sample undergoes thermal expansion. As the cure temperature is approached, the curve deviates from linearity and begins to decrease. Once the sample has equilibrated near the cure temperature (sample temperature approximately 175.5 °C), all changes in line length are assumed to be associated with continued crosslinking, or chemical shrinkage. The $\Delta L/L_0$ curve shows a negative slope until nearly the end of the 6h isothermal hold, at which point it approaches a plateau as the cure approaches completion. From this study, we measured chemical shrinkage beyond gelation to be 0.8%.

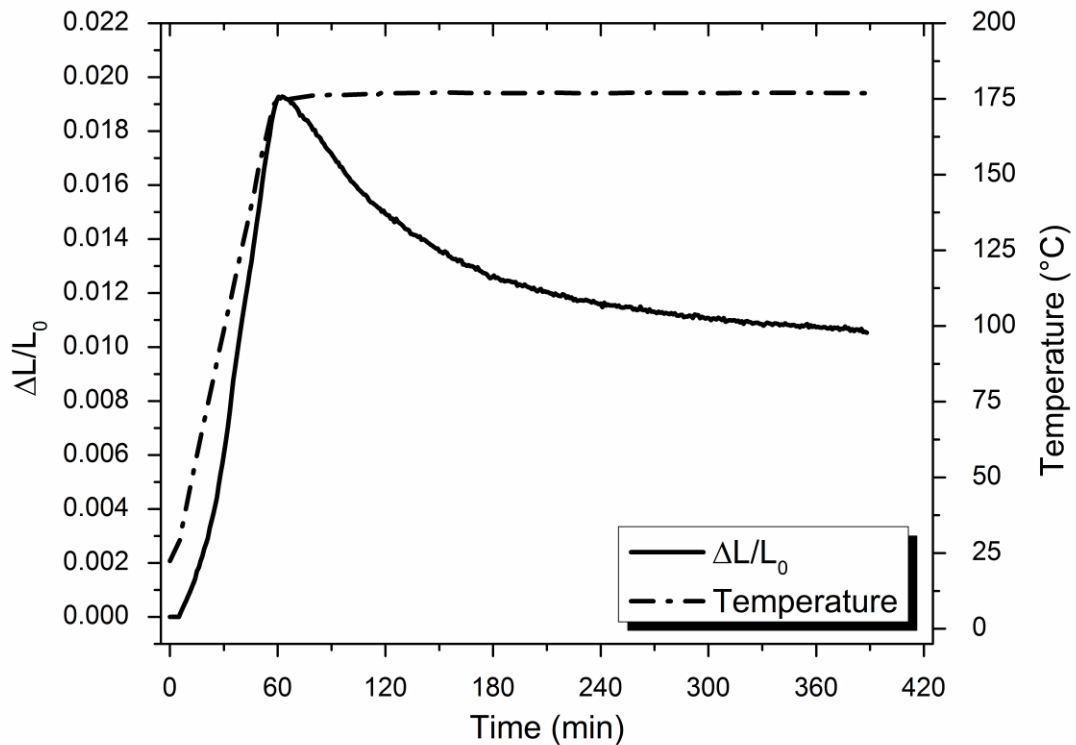


Figure 3.2 Average change in linear dimension due to heating and continued curing.

Sample: Neat 977-3 resin cube cured to gelation and quenched to room temperature before testing.

3.3.2 Thermal Expansion of Matrix and UD Fiber-Reinforced Composites

Cooling the matrix within the glassy state, from the cure temperature to room temperature, is often cited as the largest contributing factor in strain creation in continuous fiber composite laminates.^{2,51} Measurement of the glassy state CTE within the processing temperature range is desirable to simulate the cooling process. Through line length measurements on the surface of glassy polymer networks during heating, data from elevated temperature DIC may be directly compared to the linear coefficient of thermal expansion as measured by TMA. Figure 3.3 shows thermal expansion of a cured

resin cube in heating to 177 °C as the average dimension change ($\Delta L/L_0$) of five software reference lines placed vertically on the sample's strain map vs. temperature. The length of each line spans the height of the strain map on a cured sample (approximately 13.6mm in length). As with chemical shrinkage measurements, increasing the length of the analysis tool increases the signal to noise ratio. Calculated linear coefficients of thermal expansion by DIC and TMA from 25-50 °C are shown in Table 3.1. The relationship between change in line length and temperature throughout this temperature window shows a clear increase, with a “knee” at 118.5 °C by bilinear fit, suggesting a glassy-state expansion event.

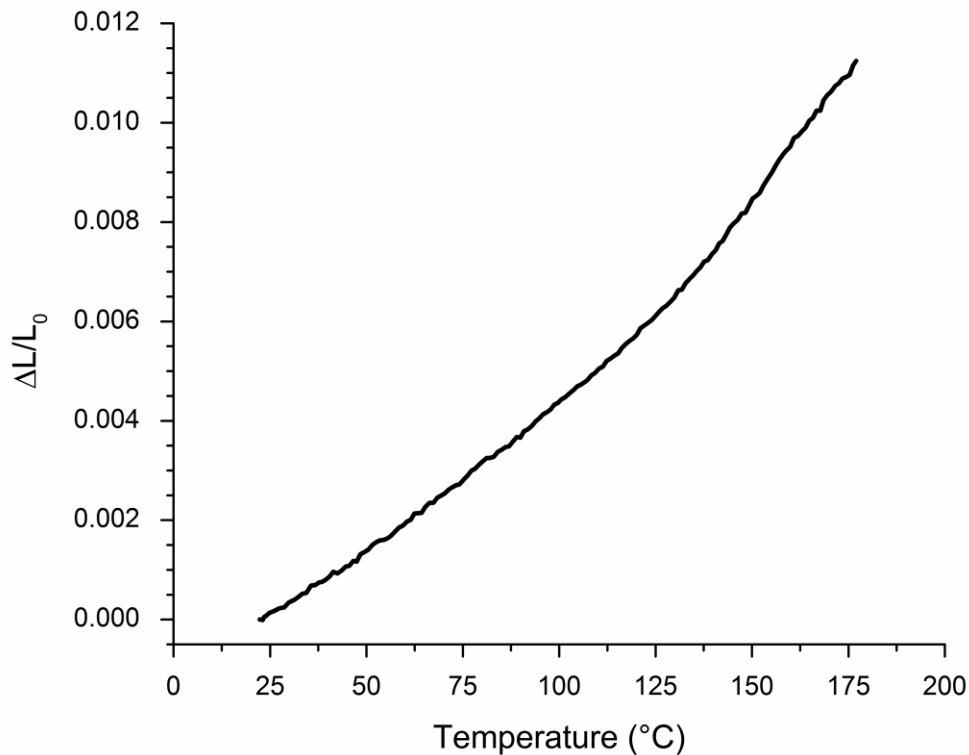


Figure 3.3 Average dimension change due to thermal expansion of cured matrix.

Sample: 977-3 resin cube cured per MRCC then heated at 1 °C/min to 177 °C.

Table 3.1

CTE values of the matrix and UD laminate obtained via TMA and DIC.

Method	Matrix CTE ($\mu\epsilon/^\circ\text{C}$)	UD Laminate CTE – Parallel to Fiber ($\mu\epsilon/^\circ\text{C}$)	UD Laminate CTE – Orthogonal to Fiber ($\mu\epsilon/^\circ\text{C}$)
TMA	62.7	-1.1	31.6
DIC	60.0	-0.65	31.4

Similar procedures for thermal expansion of neat matrix were applied to a unidirectional (UD) composite laminate to probe dimension changes due to the presence of carbon fibers. A UD laminate coupon was clamped and horizontally suspended, in this case above a non-symmetrical (NS) laminate (method discussed in Section 3.3.3). Five lines were placed parallel or orthogonal to the fiber orientation of the observed laminate surface, each spanning a length nearly equal to the width of the coupon (approximately 25 mm). Laminate orientation and reference line placement (parallel and orthogonal) are shown in Figure 3.4. Dimension changes parallel and orthogonal to the fiber orientation allowed for calculation of the effective glassy state CTE in these two directions. CTE values taken from 50-100 °C are reported in Table 3.1 with comparison to measurements obtained via TMA. Along the fiber orientation, volumetric properties are fiber-dominant and lead to thermal contraction, as denoted by a negative CTE observed in both techniques. Conversely, thermal expansion perpendicular to the fiber orientation is matrix dominant and the glassy state CTE is significantly larger. The presence of the fibers, however, significantly decreases the observed CTE as compared to the neat matrix. Decreasing the macroscopic CTE of a polymer through incorporation of low CTE reinforcements is well established.^{24,32,121}

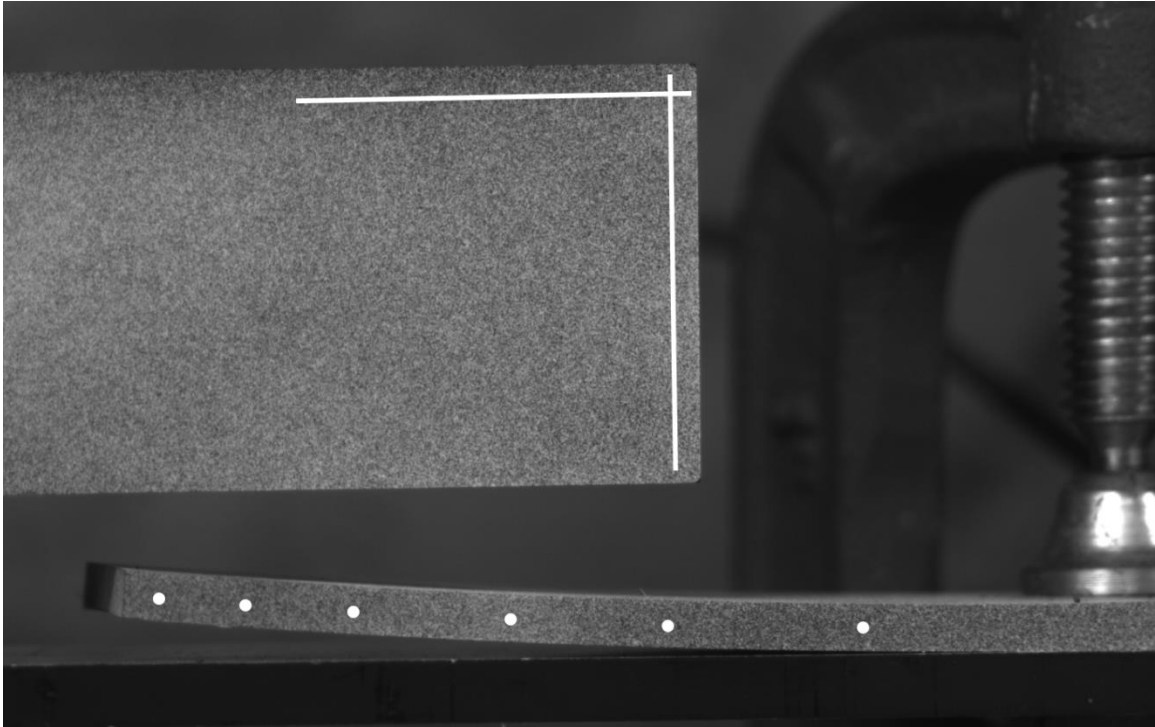


Figure 3.4 Laminate placement for CTE and strain-free temperature studies.

White lines shown as representative reference lines and stage points used for calculation of CTE and strain-free temperature.

3.3.3 Laminate Strain-free Temperature

Of the laminate sequences fabricated, NS laminates have the most significant difference in fiber orientation, leading to significant interlaminar strain. Some of this strain is relieved through geometry deformation, and large aspect ratio coupons have significant concave curvature towards the 90° surface. The residual strains causing curvature may be relieved upon heating. Elevated temperature DIC can be used to accurately track curvature compensation during heating to identify the strain-free temperature. The NS laminate was constructed with 16 plies (as opposed to eight), allowing for a thicker edge and a larger surface map. The coupon was anchored at one end with a clamp, fitted with a thermocouple, and the oven was heated at 1 °C/min to

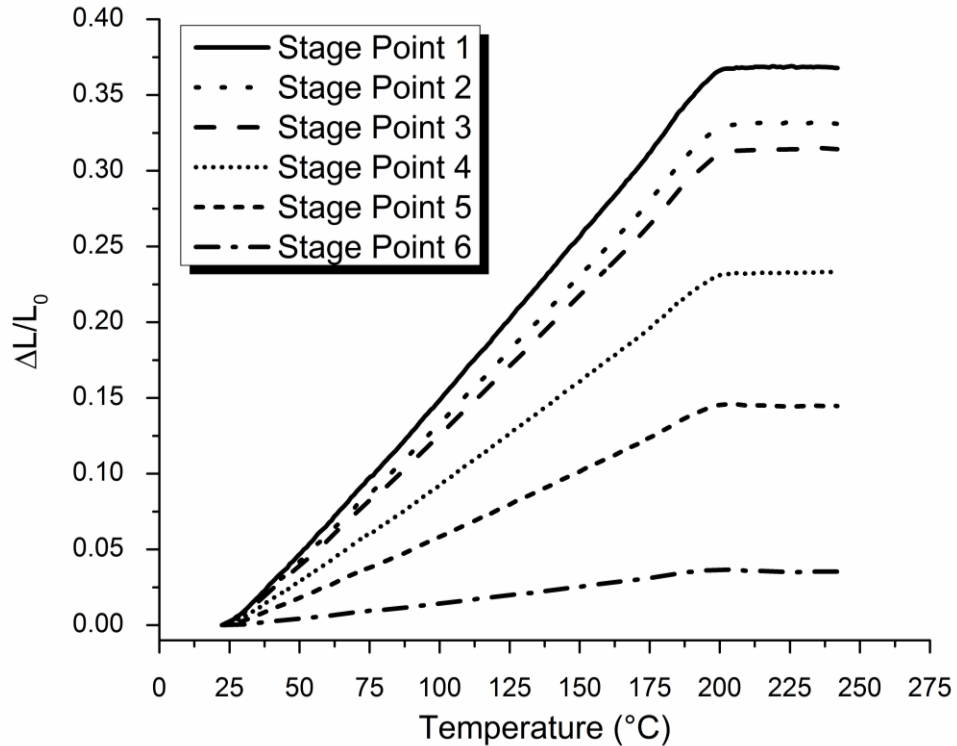


Figure 3.5 Strain-free temperature measurements by changes in reference lengths.

250 °C (see Figure 3.4, bottom). In addition to primitives, the ARAMIS software allows users to create reference planes and monitor point-to-plane distances. Point-to-plane distances can be tracked through the image series using stage points to quantify laminate curvature changes with respect to the vertical axis during the heating event. A representation of stage point placement is shown in Figure 3.4, while distance change vs. temperature for the stage points is shown in Figure 3.5. A clear plateau is observed for all stage points regardless of proximity to the anchoring clamp. From these curves, the laminate reached maximum curvature compensation at a laminate surface temperature of 199 °C. On cooling, the laminate redevelops curvature as thermal strains build, and at room temperature displays increased curvature due to exposure to temperatures above the ultimate cure temperature. This not only drove the matrix to a higher degree of cure but

also created a larger temperature differential increasing glassy state cooling.

3.3.4 Laminate Curvature Development

As the temperature deviates from the strain-free temperature, the matrix and fiber undergo significantly different volume changes, as previously observed by directional CTE differences in UD laminates, leading to non-uniform contraction. This non-uniform dimension change, which leads to curvature development in laminates which lack symmetry about the mid-plane, can be captured using elevated temperature DIC. If we consider the strain-free temperature to be the temperature at which all process-induced strains within the composite laminate have been relaxed, it is logical to regard dimensions at this temperature as the reference lengths, or L_0 . In this case, we re-heat the laminate to the strain-free temperature to compensate the residual strains induced during the cooling stage, with the assumption that thermal expansion upon re-heating produces a similar response to thermal contraction upon cooling. This allows for a simulation of the cooling stage in laminate processing, during which a significant proportion of thermal residual strains are introduced.

The effective laminate thermal properties such as CTE are combinatorial between the matrix and fiber properties and determined by laminate ply sequence. Traditional contact-based techniques such as TMA are capable of one-dimensional measurements. Therefore, these measurements are an average response from all plies within the laminate. Non-contact techniques, however, are capable of simultaneous multidirectional measurements on a surface. In the case of a composite laminate, these measurements probe the local environment of the topmost ply, thus more accurately representing the interactions between the matrix and fibers. Elevated temperature DIC is uniquely

positioned to quantify differences of the free (matrix-dominant) and hindered (fiber-dominant) thermal expansion/contraction directions on the surface of a composite laminate. Expansion/contraction anisotropy of different laminate sequences represents the variability of a composite due to the matrix and fiber constituent properties and deformation from process-induced strains. Composite anisotropy is represented in Figure 3.6, which shows the average dimension change parallel and orthogonal to the fiber orientation on the observed laminate surface. The fiber orientation on the observed surface of all laminates was 0° . Dimension changes along the surface map with respect to dimensions at the strain-free temperature were chosen to simulate the glassy state cooling process. As the temperature differential from the strain-free temperature increases, dimension changes parallel and orthogonal to the fiber axis are measurably different for the laminate sequences tested. This relationship is unique and demonstrates the benefits of elevated temperature DIC. Listed in Table 3.2 are the glassy-state CTE measurements as taken by DIC, in with comparison to TMA measurements. In both the OA and NS laminates, the parallel and orthogonal CTE values are decreased in comparison to the UD laminate. Within the TMA, the OA laminate was oriented such that the measurement was taken in the direction of the 0° fibers. Measurements by TMA are significantly different from either directional measurement taken by DIC due to being an average dimension change of all plies in the laminate.

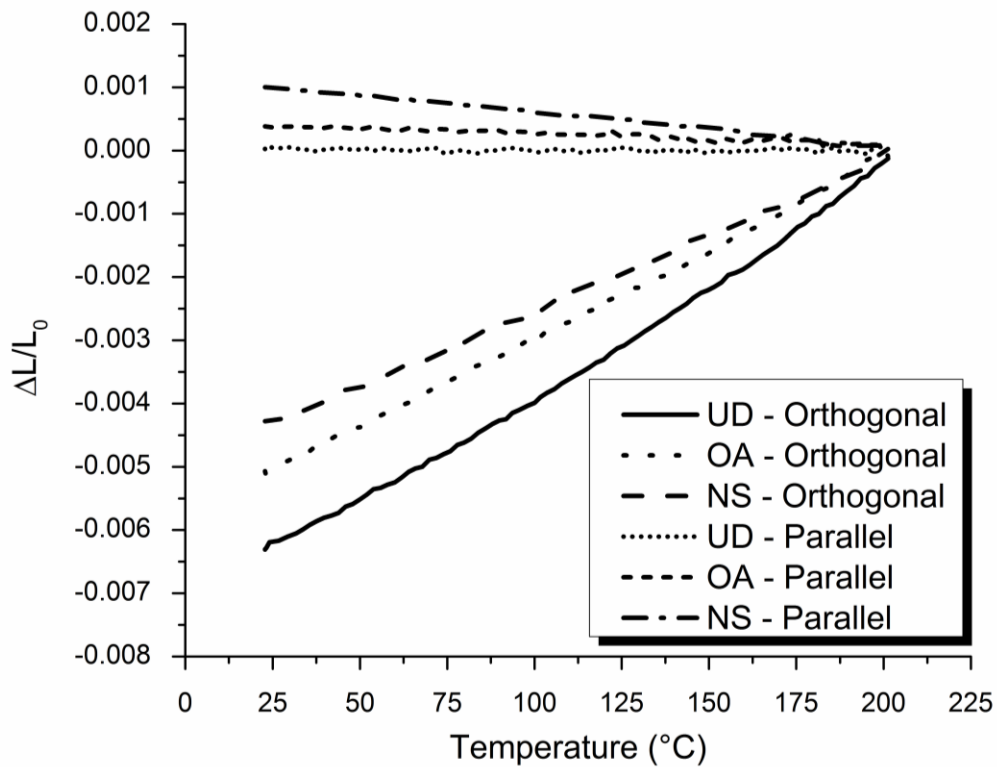


Figure 3.6 Changes in line length due to heating.

In this case, we have plotted the reference length at the strain-free temperature. The line slopes are representative of dimensional changes upon cooling from the strain-free temperature to room temperature.

Table 3.2

Glassy-state CTE values for variable fiber orientation laminates.

Laminate Sequence	DIC CTE – Parallel to Fiber ($\mu\epsilon/^\circ\text{C}$)	DIC CTE – Orthogonal to Fiber ($\mu\epsilon/^\circ\text{C}$)	TMA CTE – Parallel to 0° ($\mu\epsilon/^\circ\text{C}$)
0_8	-0.65	31.4	-1.1
$0_8/90_8$	-5.3	23.8	13.7
$0_4/+45_4$	-1.5	27.8	4.4

The UD laminate does not contain off-axis lamina, and thus the expansion/contraction properties of the observed surface are highly anisotropic with respect to the fiber orientation. Length changes parallel to the fiber orientation are

restricted throughout the temperature window tested. Orthogonal to the fiber orientation, however, significant increase/decrease in line length was observed with increasing/decreasing temperature, indicating matrix-dominant thermal expansion/contraction. The OA and NS laminates exhibit a similar difference in parallel vs. orthogonal directions; however, the expansion/contraction behavior of their observed surfaces is also affected by the nearby off-axis plies. The angular difference in fiber orientation of the NS laminate is 90° , thus the relative matrix and fiber-dominant directions are orthogonal about the mid-plane of the laminate. Therefore, expansion/contraction of the observed surface in the matrix-dominant direction is resisted by nearby layers whose expansion/contraction properties are fiber-dominant in this direction. This is apparent by the smaller slope of the NS laminate orthogonal to the fiber direction compared to the UD laminate. Due to a smaller angular difference in the OA laminate, this constraint is less prominent, which corresponds with increased dimension change in the orthogonal direction as compared to the NS laminate. However, both the OA and NS laminates have plies which resist free expansion of the observed surface, decreasing the effective CTE in the matrix-dominant direction in comparison to the UD laminate.

In Figure 3.6, it should be noted that the OA and NS laminates both show non-zero slopes parallel to the fiber orientation, while the curve of the UD laminate has effectively zero slope. On cooling below the strain-free temperature, residual strains build and cause curvature to develop within laminates which do not have symmetry about the mid-plane. By this method, changes in line length parallel to the fiber axis represent curvature development. The UD laminate has symmetry about its mid-plane, thus no

curvature changes contribute to the $\Delta L/L_0$ calculations. This corresponds with large thermal expansion/contraction anisotropy relative to the fiber direction. To show this, we compare differences in $\Delta L/L_0$ values for the parallel and orthogonal directions in Figure 3.7. Differences in slopes represent the magnitude of curvature development during glassy-state cooling below the strain-free temperature. This demonstrates how varied fiber orientations affect laminate expansion/contraction properties upon heating/cooling. Direct measurement of laminate thermal properties is a unique capability of elevated temperature DIC and can complement thermal strain calculations based on classical laminate theory.

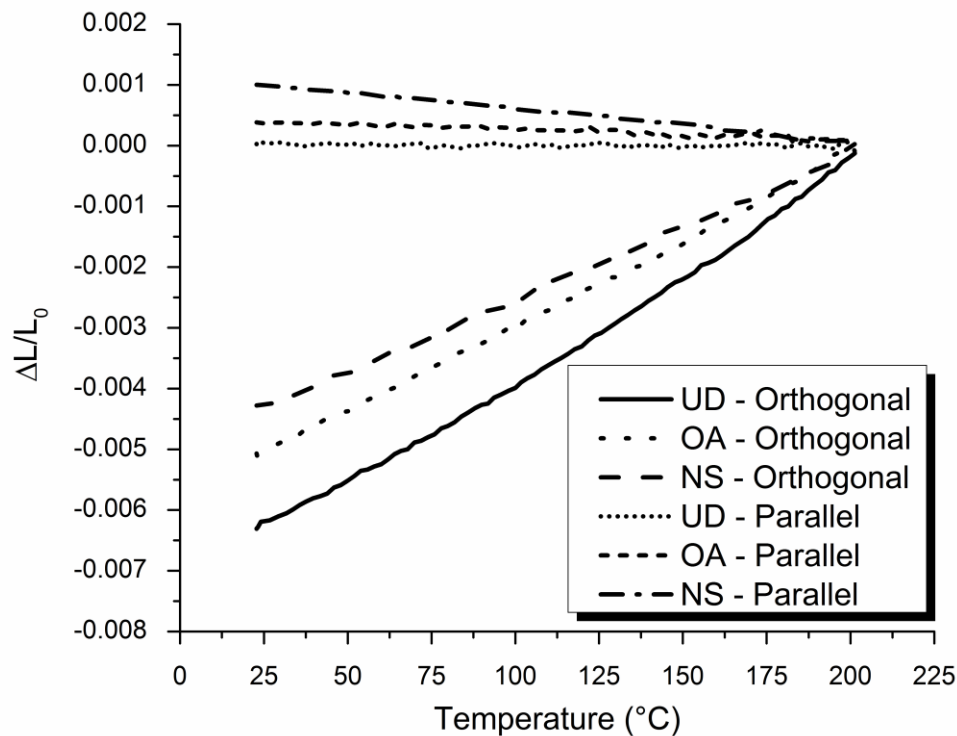


Figure 3.7 Differences in line length changes with temperature.

3.4 Conclusions

The objective of this research was to develop elevated temperature digital image correlation techniques to study the volumetric behavior of glassy polymer networks and composite laminates during thermal expansion/contraction events. A holistic understanding of a composite material's constituent properties is necessary for the proliferation of composites manufacturing and use. Process-induced strains are a challenge to the composites community, yet there persists a lack of standard testing methods. Traditional laminate deformation techniques, which only examine laminate geometry before and after cure, often exhibit unexpected or noisy data. We propose using dimension changes throughout a heating event, such as expansion differences and curvature compensation, as means to probe the residual strain state of composite laminates. Judicious selection of laminate sequences can be used to exhibit differences in matrix and fiber volumetric properties, thus giving insight to their compatibility with respect to process-induced strains. Through the use of software reference tools, we demonstrated elevated temperature DIC is an excellent technique for accurate identification of the strain-free temperature, which is a critical property for simulation of composite processing and performance. Dimensional measurements were taken for multiple directions simultaneously and, in the case of a composite laminate, used to represent local environment on the laminate surface rather than a combined laminate average, as is the case in traditional techniques. This gives the researcher increased insight into the compatibility of the volumetric properties of the constituent components. Critical volumetric properties, such as matrix chemical shrinkage beyond gelation, as well as CTE of the matrix and directional CTEs of the composite laminate, were

quantified and showed excellent correlation to traditional techniques, in some cases offering additional insights. Ultimately we found this technique to be equally advantageous and simple to use as traditional DIC methods, requiring only extra consideration for system calibration and lighting.

CHAPTER IV – EFFECT OF CHAIN RIGIDITY ON THERMAL, PHYSICAL, AND THERMOMECHANICAL PROPERTIES OF GLASSY AMORPHOUS NETWORKS

4.1 Introduction

To improve the ability to predict and model cure-induced strains in composite materials, we must understand how strains are generated and stored within the polymer matrix. This requires an understanding of polymer science and polymer physics and is an immense challenge still very much unanswered in the relatively young age of polymers and associated composite materials. At the core of the challenge is the complication of intramolecular and intermolecular contributions, the complex roles of which separate polymers – specifically glassy amorphous polymers – from more traditional material classes.

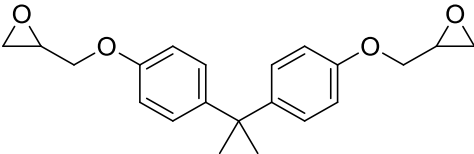
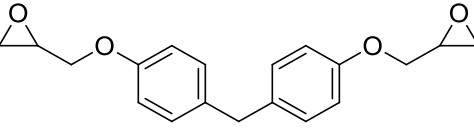
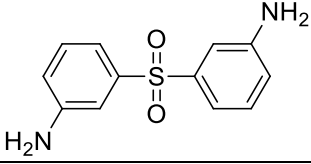
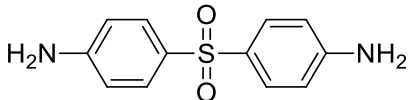
Upon increases in energy state, via thermal or mechanical means, molecular motions are increased in frequency and magnitude. The molecular architecture of a polymer determines the motions available to it through intra- and intermolecular interactions. Small changes in chemical structure, such as structural isomerism, correlate with sizeable differences in thermal and mechanical properties. Isomers do not differ chemically, thus we expect most secondary intermolecular interactions (hydrogen bonding, dipole-dipole interactions, and van der Waals forces) to be very similar, with differences arising from chain rigidity and packing (bulk density). Here we investigate the role of intramolecular contributions, specifically chain rigidity, in amorphous polymer network thermal properties, architecture, glassy state molecular relaxations, and mechanical performance.

Chain rigidity is defined as resistance to conformational changes of chains or chain segments. In thermoplastics, this is commonly referred to as how “rod-like” or “worm-like” polymer chains are in the solution state, indicative of the ability for chains to adopt various conformations along its length. Rigid polymer chains frustrate chain packing, leading to increased micro-porosity and free volume.¹²² In common thermoplastics, thermal, mechanical, and physical properties attributed to chain rigidity are often discussed in terms of “effective” rigidity due to the prominent role of secondary interactions in chain behavior. The polymer network isomers investigated here offer the benefit of being chemically-similar, and also able reach effectively full conversion. This allows us to probe the effect of chain rigidity on properties of interest while minimizing variation and confounding contributions from secondary interactions, chain ends, etc.

Considering diglycidyl ether of bisphenol F (DGEBF) and diglycidyl ether of bisphenol A (DGEBA) epoxy networks, the idealized epoxy prepolymer structures differ only by the molecular bridge between phenyl rings, with DGEBF incorporating a methylene bridge compared to the isopropylidene bridge in DGEBA (shown in Table 4.1). Previous work in our group has shown this substitution of methyl groups on the quaternary carbon in place of smaller hydrogen atoms increases thermal properties such as T_g and physical quantities such as fractional free volume and average free volume hole size.⁹⁴ Because hydrogen and methyl groups share similar polarity or lack thereof, the substitution does not significantly change the intermolecular forces acting between adjacent chain segments. Beyond this, the aromatic diamine structural isomers 33DDS and 44DDS have been shown to lead to significantly different thermal and mechanical properties. This creates a unique research space to probe effects on thermal, architectural,

Table 4.1

Epoxy prepolymers and diamine curatives.

Chemical Structure	Abbreviation	Molecular Weight (g/mol)
	DGEBA	350-360 EEW: 175-180
	DGEBF	330-346 EEW: 165-173
	33DDS	248.3
	44DDS	248.3

EEW: Epoxide equivalent weight.

and mechanical properties controlled by chain rigidity. This work will expand upon previous research by the Wiggins Research Group to establish the role of chain rigidity and its impact on key properties of glassy amorphous polymer networks. For the remainder of this dissertation, abbreviations will be used to denote the specific epoxy-amine network being discussed, listed in Table 4.2.

Table 4.2

Epoxy-amine network isomer nomenclature.

Epoxy	Amine	Abbreviation
DGEBF	33DDS	33F
DGEBF	44DDS	44F
DGEBA	33DDS	33A
DGEBA	44DDS	44A

4.2 Results and Discussion

4.2.1 Effect of Structural Isomers on Network Thermal Properties

From the family of polymer networks created by the building blocks shown in Table 4.1, the effect of chain rigidity is perhaps most pronounced in measurements of the glass transition temperature. To ensure networks were completely cured, and also shared similar thermal histories prior to testing, samples were subjected to a heat-cool-heat-cool-heat DSC cycle. During the first heating, an exotherm was prominent in 44F, 33A, and 44A, suggesting the highest T_g systems were under-cured after the academic cure cycle. Additionally, some thermograms showed peculiar behavior above T_g due to thermal histories involving annealing and extended room temperature aging. Shown in Figure 4.1 are two DSC thermograms of a fully cured 44F sample. The solid curve was generated from the sample which had been slowly cooled from the ultimate cure temperature (225 °C) in the oven and allowed to age at room temperature for several days. The dashed curve shows the same sample after its thermal history was first erased by quenching from the rubbery state (250 °C) and reheated. The endothermic step at T_g is effectively equal in both curves, suggesting the sample did not cure further between heating cycles; however, the aged sample shows a gradual exotherm above T_g which typically signifies residual curing. The refreshed sample, which was quenched from the rubbery state by cooling at 10 °C/min, does not show the same rubbery state behavior upon subsequent reheating. This behavior was present to some extent in all four network isomers investigated here and suggests the glassy networks are susceptible to aging, which causes changes in chain packing and heat capacity. This behavior is quite different from more traditional aging behavior, which involves an extended endotherm at T_g . We suspect the deviation from

typical aging behavior is arises from the highly crosslinked, rigid nature of the networks, though additional studies will be needed to explain this.

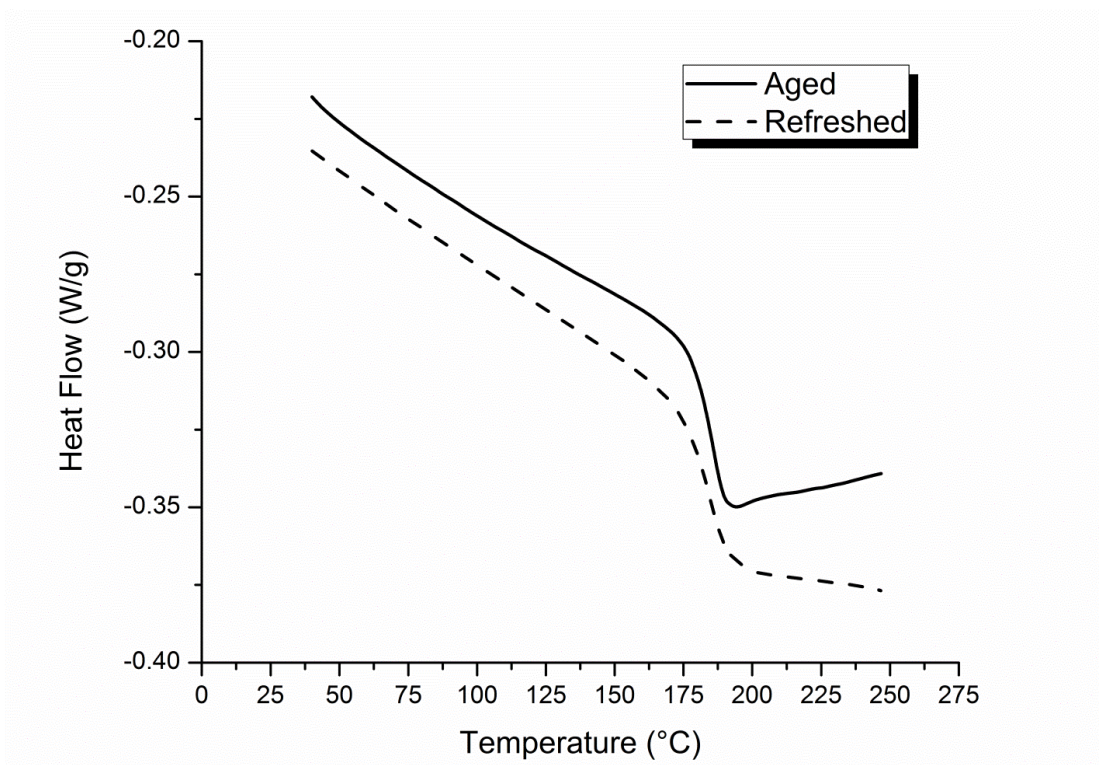


Figure 4.1 DSC thermograms of 44F with and without thermal quenching.

The solid curve represents a sample of 44F which had been slowly cooled and aged below T_g for several days, while the dashed curve represents the same sample after quenching from the rubbery state.

While typically defined as the resistance to conformational changes, rigidity of a polymer chain can also be defined as resistance to cooperative, long-range motions (which are understood to involve conformational changes). The variation in chain rigidity of the studied network isomer series causes the chemically-similar polymer networks to have a range of 67 °C in T_g as measured by DSC. Shown in Figure 4.2 are DSC

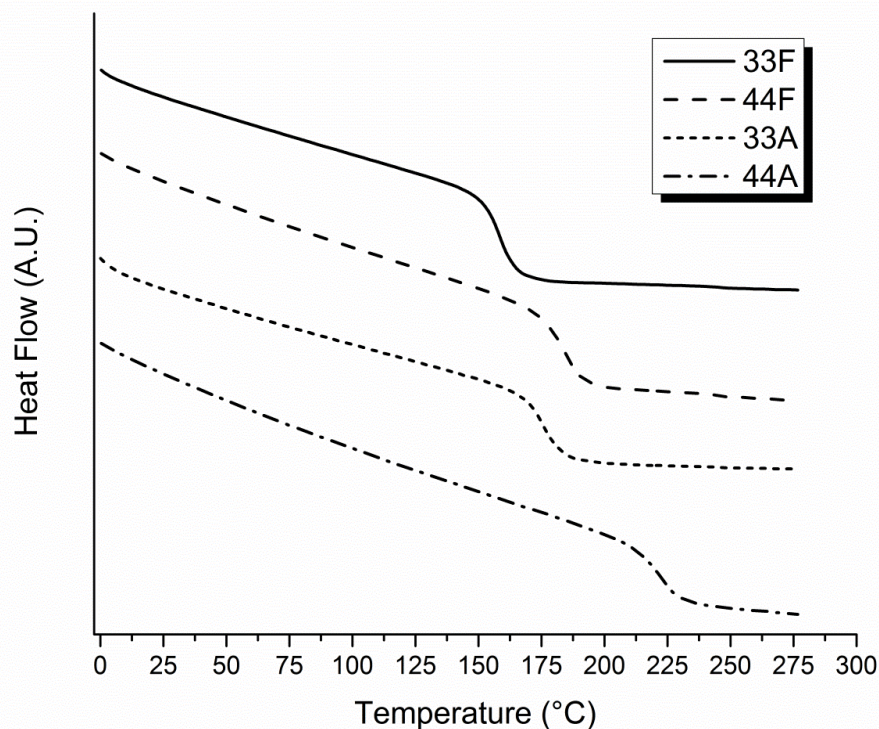


Figure 4.2 DSC thermograms showing T_g s of network isomer series.

DSC thermograms of T_g s show increasing rigidity from top down. Endotherm down.

thermograms of DGEBF and DGEBA network isomers during a heating scan at 10 °C/min. There is a clear trend in T_g value between meta- and para-substituted diamines. For DGEBF and DGEBA networks, the para-substituted network isomer increases the T_g relative to the meta-substituted networks by 25 and 50 °C, respectively. This isomer effect on T_g has been observed in many linear amorphous polymers such as polyethylene terephthalate vs. polyethylene isophthalate,¹²³ polysulphones,¹²⁴ and polyimides.¹²⁵ With increased rigidity caused by the para-substituted backbone, T_g values are consistently greater than those of the meta isomer. The trend is consistent when comparing DGEBF isomers with DGEBA isomers, with DGEBA networks exhibiting increased T_g ,

suggesting differences in chain segment rigidity within the epoxy prepolymer as a result of the two methyl units. A comparison of 33F with 33A, and 44F with 44A shows the substitution of isopropylidene for a methylene bridge is accompanied by an increase of T_g of approximately 20 and 40 °C for meta- and para-substituted networks, respectively (see Table 4.3).

Table 4.3

T_gs of networks formed from structural isomers.

Network	DSC T_g (°C)
33F	157
44F	182
33A	177
44A	224

Beyond rigidity arguments, explanations of the increased T_g in para-substituted polymers can also consider configurational entropy. The relation of configurational entropy to the glass transition was first proposed by Adam and Gibbs theory of T_g , stating T_g occurs when the entropies of the molten/rubbery and solid states are equal, termed excess entropy.¹²⁶ In studies of glassy polymer network isomers, Kaushik suggested networks formed from meta-substituted diamines possessed increased configurational entropy in the uncured state, which continues throughout network formation and cooling into the glassy state.⁹³ While a meta-substituted isomer has cis and trans conformers, as shown in Figure 4.3, the para isomer has significantly smaller configurational entropy and is restricted to simple motions such as ring flips along a single axis. Applying the thermodynamic theory of T_g , Kaushik proposes the increased configurational entropy present in a cured, meta-substituted network requires additional cooling to approach the

minimum entropy state (theoretical $S=0$), accounting for the lower T_g in comparison to para-substituted network isomers.

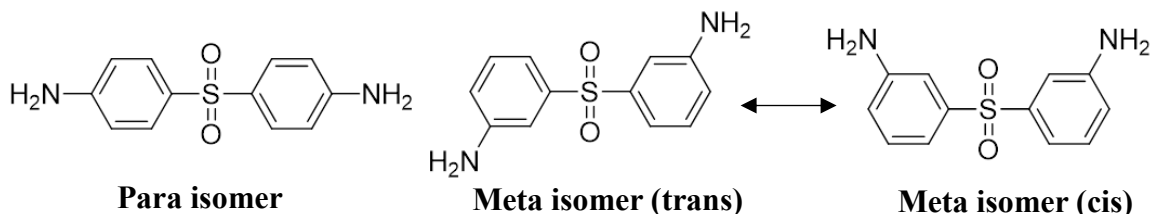


Figure 4.3 Diaminodiphenyl sulfone structural isomers.

DDS meta isomers has the ability to adopt cis and trans conformations, while the para isomer is fully extended and has no additional conformations.

4.2.1.1 Polymer Fragility Considerations

The fragility of an amorphous glass characterizes the rate at which a material's relaxation dynamics decrease upon cooling through the glass transition temperature. A material is classified as "strong" if its relaxation dynamics change relatively slowly upon cooling through T_g . Conversely, materials with increased fragility have a relatively narrow glass transition range, and relaxation dynamics change rapidly upon cooling through T_g . The relationship between polymer chain structure and fragility is complicated when considering organic materials which undergo hydrogen bonding (liquid crystalline polymer behavior, for instance) and/or have varying backbone rigidity.¹⁰² When examining chemically-dissimilar materials, authors have attributed differences in fragility to "effective" chain rigidity, influenced by side chain and intermolecular interactions.¹²⁷ Bartolotta and coworkers showed increasing network connectivity of heterocyclic polymer networks while maintaining chemical structure, was accompanied by a decrease in thermodynamic fragility. Thermodynamic fragility differs from traditional fragility in

that it is derived from changes in heat capacity through the glass transition, as compared to relaxation dynamics, and is calculated as the ratio of heat capacities below and above T_g . In this case, more change in heat capacity at T_g (i.e. larger ratio) results in a greater thermodynamic fragility (i.e. more fragile than strong). Bartolotta attributed the decrease in thermodynamic fragility to fewer degrees of freedom with increased crosslinking, originating from a decrease in configurational entropy of the system.⁸⁵ We propose a similar decrease in thermodynamic fragility due to differences in configurational entropy between the meta- and para-substituted diamine isomers. As shown via thermodynamic fragility values in Table 4.4, this is indeed the case, with 33F and 33A exhibiting greater values than the 44F and 44A networks. The rate at which the amorphous networks undergo changes in heat capacity through T_g can also be shown by its breadth. In Figure 4.4, a comparison of 33A and 44A heat flow and heat flow derivatives shows the step size and breadth of T_g differ due to the diamine isomer. Considering the increased configuration entropy available to 33A in the rubbery state, this strongly indicates the molecular motions available in the rubbery and glassy states are dependent on the diamine structural isomer, and therefore chain rigidity. The dependence of glassy and rubbery state degrees of freedom on chain rigidity can be further probed through comparison of the two most structurally dissimilar networks, 33F and 44A, shown in Figure 4.5. This comparison yields an even greater difference in the step size and breadth of T_g , further demonstrating the relationship between chain rigidity and thermodynamic fragility. T_g breadth (FWHH) and thermodynamic fragility measurements are shown in Table 4.4. The peak onset and offset of the derivative curve was used to determine glass

transition onset and offset temperatures (glassy and rubbery state, respectively) for thermodynamic fragility calculations.

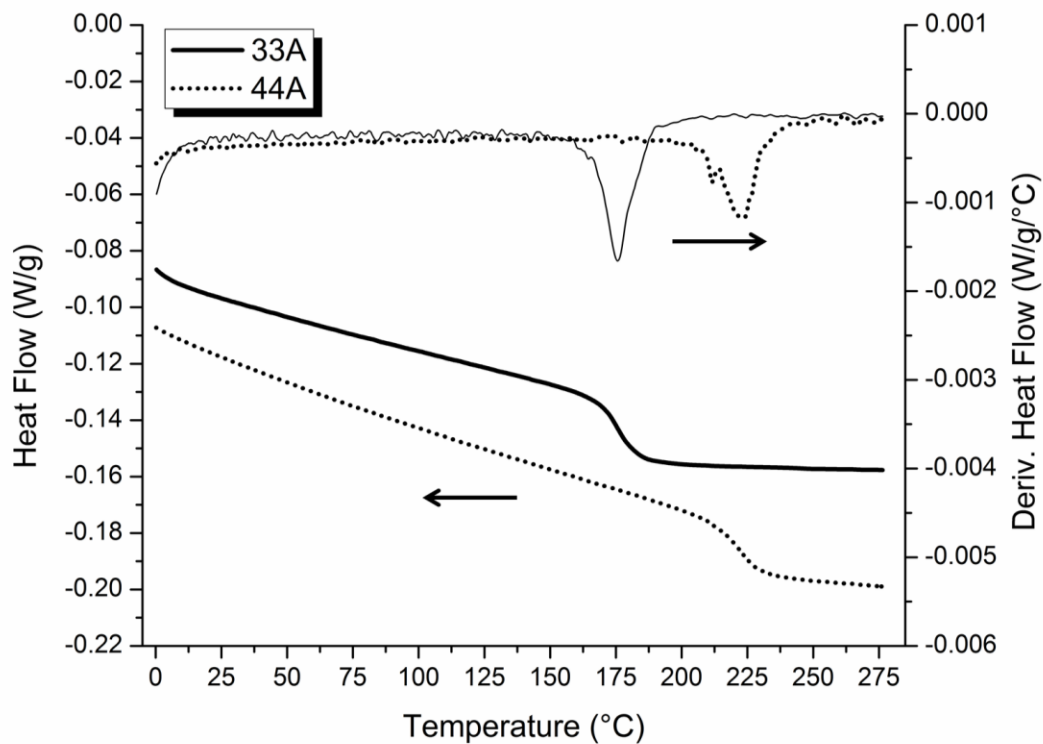


Figure 4.4 Heat flow and heat flow derivatives of DGEBA isomers.

Larger endothermic step at T_g shows the increased fragility of 33A. 44A also shows increased T_g breadth by the derivative peak.

Arrows point to corresponding vertical axes. Endotherm down.

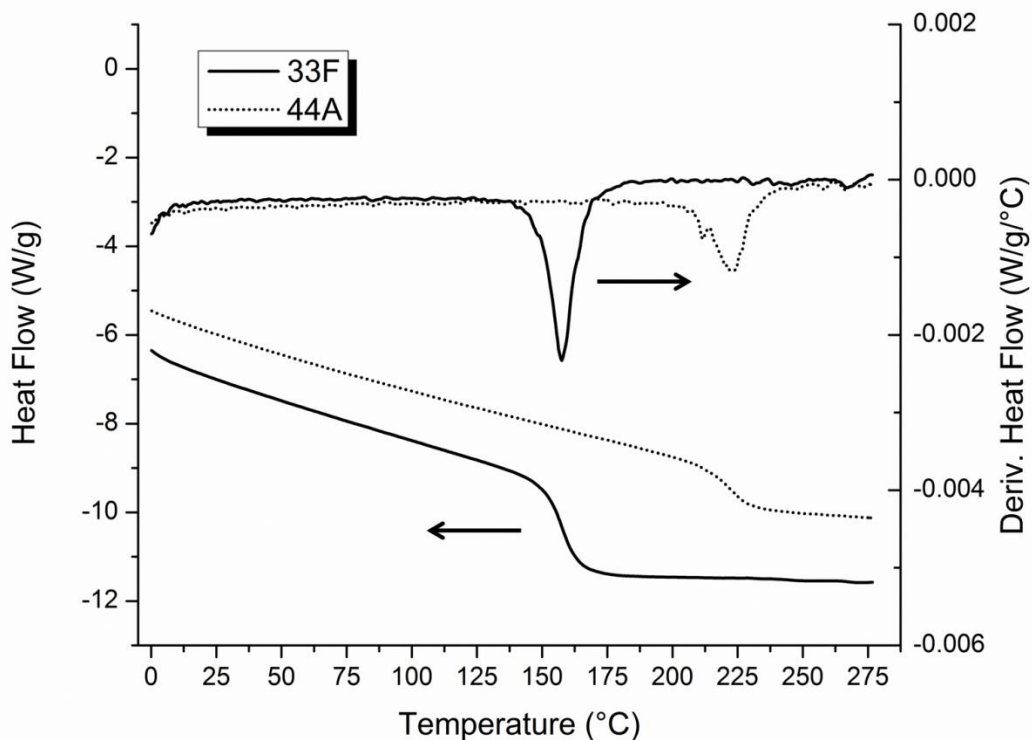


Figure 4.5 DSC thermograms of 33F and 44A.

Arrows point to corresponding vertical axes. Endotherm down.

Table 4.4

Differences in thermodynamic fragility via DSC measurements.

Network	DSC T_g (°C)	Thermodynamic Fragility	Peak Intensity (mW/g/°C)	FWHH (°C)
33F	157	1.256 ± 0.003	2.247 ± 0.05	9.5 ± 0.2
44F	182	1.190 ± 0.003	1.654 ± 0.05	13.5 ± 0.1
33A	177	1.194 ± 0.002	1.553 ± 0.03	11.6 ± 0.5
44A	224	1.140 ± 0.001	1.112 ± 0.06	17.4 ± 0.5

In the network isomer series investigated here, the meta-substituted diamine networks possess increased configurational entropy but decreased rigidity compared to their para-substituted counterparts evidenced by their T_g s. Similarly, DGEBF network

isomers have decreased rigidity to their DGEBA counterparts. This increase in chain rigidity causes a decrease in thermodynamic fragility. Changes in heat capacity, representing changes in degrees of freedom, upon exceeding T_g are greater for the less rigid networks, as evidenced by the thermodynamic fragility of the meta-substituted diamine networks. Shown in Figure 4.5, the heat flow derivative curve also shows a sharper peak for 33F relative to 44A, suggesting the abruptness of the glass transition is controlled by chain rigidity. This is also supported in FWHH measurements, which trend with T_g s and thus rigidity. Composed of the least rigid epoxy prepolymer and diamine curative, 33F has the most abrupt glass transition. This suggests the available degrees of freedoms (i.e. molecular relaxations) are very different between the glassy and rubbery states. The rigid, symmetrical backbone in 44A promotes additional degrees of freedom in the glassy state, such as local mobility of chain segments.

Differences in thermodynamic fragility calculations suggest the degrees of freedom available in the glassy and rubbery states are increased with chain rigidity, with 44F and 44A showing decreased thermodynamic fragility compared to their meta-substituted counterparts. Further, the breadth of the glass transition is increased between network isomers, and also epoxy prepolymers, in the same trend as T_g and therefore network rigidity. This establishes that network rigidity holds a prominent role in the glass transition of amorphous glassy polymer networks. Molecular mobility requires more than backbone symmetry and stiffness, however, and will be dependent on nearby chain segments and available space. To probe this, we will next investigate network architecture through density and free volume measurements, discussed in respect to chain rigidity.

4.2.2 Role of structural isomers and chain rigidity in network architecture

4.2.2.1 Effect on Chain Packing

Upon cooling from elevated temperature, network chain segments reduce in volume as chain segments find a more favorable equilibrium and free volume decreases. This causes a significant bulk densification, and can be measured through thermal expansion/contraction experiments. The ability of network chain segments to adopt multiple configurations upon cooling will largely influence the ability to efficiently pack. The rigidity of a polymer chain inhibits conformational changes, which can decrease packing efficiency in some cases. Chain packing can be represented via bulk density measurements for materials with identical atomic compositions, such as the epoxy network isomers studied here. The room temperature densities, average free volume hole size (V_H), and fractional free volume (FFV) of the network isomer series is listed in Table 4.5. A comparison with bulk density and free volume with T_g of meta- and para-substituted networks shows the higher T_g para-substituted DGEBF and DGEBA network isomers is paired with decreased packing efficiency, evidenced by the decreased density and increased V_H . The rigid, symmetrical backbone of the para-substituted diamines causes local chain segments to resist conformational changes upon network formations and/or cooling, inhibiting their ability to adopt the alternating (for example) cis, trans, and gauche conformers necessary for efficient packing, thereby decreasing density. Although para-substituted networks pack less efficiently, they also resist configuration changes upon heating which increases T_g .

Table 4.5

Thermal and physical properties of difunctional epoxy network isomers.

Network	DSC T _g (°C)	Density (g/cm ³)	Average hole size (V _H) at 23 °C (Å) ³	Fractional Free Volume (%)
33F	157	1.274 ± 0.001	67	3.8
44F	182	1.266 ± 0.004	76	4.2
33A	177	1.236 ± 0.002	77	4.6
44A	224	1.231 ± 0.001	82	4.8

An understanding of chain packing supports prior considerations to thermodynamic fragility, with more rigid networks showing less efficient packing and decreased thermodynamic fragility. With increased average free volume hole size and fractional free volume, the rigid, symmetrical backbone and relatively loosely-packed chain segments in 44F and 44A promote additional degrees of freedom in the glassy state, such as local short-range mobility, compared to 33F and 33A. It makes sense, therefore, that upon entering the rubbery state the relative increase in mobility would be less so for para-substituted networks than the less rigid, more densely-packed meta-substituted networks whose relative gain in degrees of freedom is greater. This relationship continues across DGEBF and DGEBA networks, with comparisons between 33F and 44A showing the largest differences in T_g and thermodynamic fragility as well as free volume.

4.2.2.2 Free Volume Considerations

The contribution of free volume to the specific volume of polymers was originally conceptualized in 1962 by Simha and Boyer, and shown in Figure 4.6.¹²⁸ The rate of contraction of the specific volume on cooling undergoes an observable slope change near

the glass transition, which is attributed to changes in the compression of free volume as the glass is trapped in a non-equilibrium state. The occupied volume (V_{Occ}) is comprised of the van der Waals volume (V_{vdW}) and interstitial free volume, the former of which is usually assumed to be temperature independent. In addition, the specific volume includes excess free volume, which is represented as the difference between the V_{Occ} and measured volume curves. The most basic consideration of the free volume theory of the glass transition states that upon reaching some critical minimum value of total free volume (V_F) in cooling from the rubbery state, long-range molecular rearrangements effectively cease and the material enters the glassy state.⁶⁵ Materials of similar or identical chemical composition and melt/rubbery state densities should correlate in free volume and T_g .

There has been relatively little research on systematic alteration of chain rigidity to study its effect on chain packing and free volume. Yang and coworkers connected free volume with chain rigidity through variation of aromatic and aliphatic content in the epoxy and amine backbones, showing increases in rigidity correspond with increased free volume.²² Kaushik studied linear polymer isomers (polyethylene terephthalate and polyethylene isophthalate) as well as 33F and 44F network isomers and found in each scenario the para-substituted backbones exhibit increased T_g , FFV, and V_H attributed to increased rigidity.⁹³ A minimum excess free volume (or a minimum % free volume) is

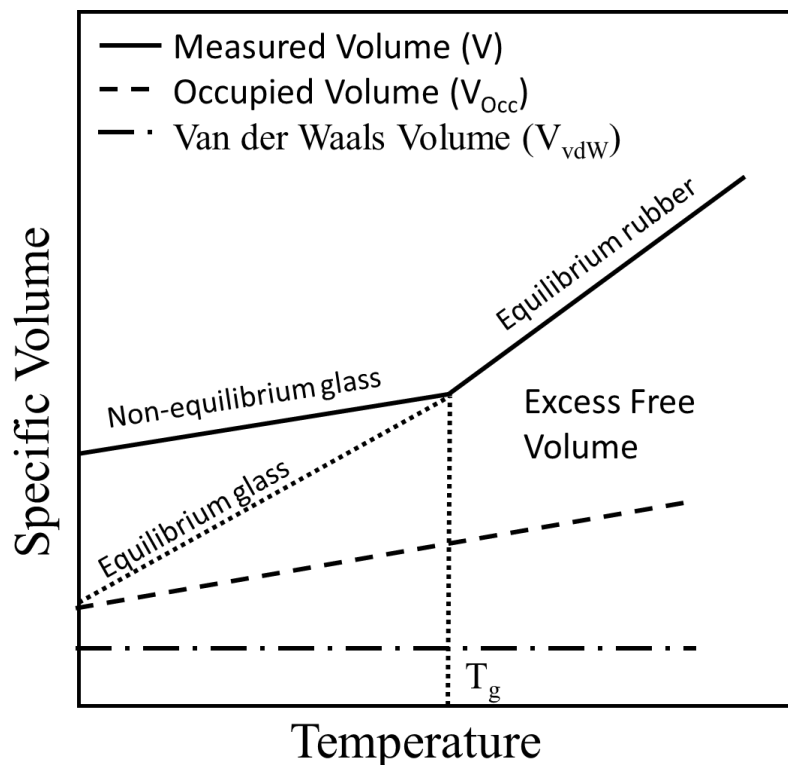


Figure 4.6 Components of specific volume vs. temperature.

required to keep the polymer in the rubbery state upon cooling (or conversely, a maximum upon heating). More rigid polymers, which also exhibit higher T_g s, require more free volume to retain the rubbery state. The polymer networks studied here benefit from chemical similarity, similar crosslink density, thermal stability, and the ability to reach effectively complete cure, affording us a research space to specifically consider the role of rigidity.

Table 4.5 shows a clear trend of chain packing and total free volume with network rigidity. For each epoxy network, the order of T_g is shared with V_H and FFV. The rigid, extended para-substituted networks possess increased V_H , FFV, and T_g s, and decreased density. The meta-substituted network isomers each exhibit a decreased V_H , FFV, and also decreased T_g compared to the para-substituted counterparts. With additional

conformers and thus configurational entropy, meta-substituted networks cool in the rubbery state to lower temperatures before undergoing the glass transition. This allows the chains to pack more efficiently, causing increased bulk density and decreased free volume. The para-substituted networks have less configurational entropy, thus undergoing the glass transition at higher temperatures, packing somewhat inefficiently due to their rigidity, and causing a higher amount of free volume to be frozen into the network. This is clear in comparisons between 33F and 44F and also 33A vs. 44A.

Recently authors connected the Adam and Gibbs theory of vanishing excess entropy with similarly decreasing excess free volume upon cooling, proposing T_g occurs at a minimum free volume and equal glassy and rubbery state configurational entropies.¹²⁹ In cooling from very high temperatures where configurational entropies can be considered equal, chains with additional configurational entropy are able to cool further before minimum configurational entropy is reached causing a lower T_g . This is accompanied by continued chain packing and densification of the less rigid chain segments, accounting for decreased free volume at and below T_g . Increased packing, with decreased average free volume hole size, has been shown to improve resistance to solvent ingress in the glassy state.¹³⁰ Therefore while network rigidity is favorable for increasing thermal stability vis-à-vis the glass transition, expected reduction in chain packing causes other properties to decline.

Structural differences across the network isomer series are very minor, yet cause significant thermal and architectural differences as shown here. The highest T_g is accompanied by the largest V_H , and the lowest T_g by the smallest V_H . Interestingly, 44F and 33A show very similar values of each despite clear structural differences in network

constituents. In the case of 44F a more rigid diamine in combination with a less rigid epoxy to form a network with comparable architecture and thermal properties to a network composed of a less rigid diamine and more rigid epoxy. Even more, thermodynamic fragility calculations are also quite similar, thus the available degrees of freedom are very similar in the glassy and rubbery states despite structural differences. This suggests the combination of a more rigid epoxy and less rigid diamine, or vice versa, creates a network with an averaged rigidity parameter. To probe this concept, we will investigate further using thermal expansivity measurements.

4.2.3 Influence of Network Rigidity on Thermal Expansion

The relationship of chain rigidity and chain packing has profound impacts on a polymer's thermal and physical properties. Density and free volume data suggest chain rigidity dictates the efficiency of chain packing, leading to decreased density and increased V_H and FFV. Similarly, T_g , breadth of T_g , and thermodynamic fragility measurements suggest increased chain rigidity delays the onset of cooperative long-range motions upon heating through the promotion of glassy state molecular motions. Additional degrees of freedom in the glassy state decrease relative gain in translational freedom at T_g and also increase its breadth. The coefficient of thermal expansion (CTE) describes the dimension changes a material exhibits as a function of temperature. Linear CTE (α_L) is described in Equation 4 below. In polymeric materials, CTE varies greatly with temperature, with significant changes in its value occurring at state transitions, such as the glass transition. As temperature increases polymer chains in the glassy state increase in mobility and occupied volume, accompanied by increases in free volume.^{20,21} This causes polymers to have a large CTE compared to other condensed matter materials.

Except for a few specialty polymers, such as liquid crystalline polymers, thermal expansion is isotropic; however, the relationship between polymer molecular structure and CTE is not well understood, particularly regarding polymer networks.¹³¹

$$\alpha_L = \frac{\Delta L}{L_0} * \frac{1}{\Delta T} \quad (4)$$

In addition to magnitude, the CTE of polymers is more complex compared to other condensed matter materials. Specifically, the CTE is highly sensitive to the temperature range at which it is calculated, specifically the proximity of the polymer's T_g . As a polymer is heated, increasing the energy of the system, the frequency of molecular motions increases. Also upon heating, free volume within the polymer expands, with large increases occurring at the glass transition.¹³² Variations in polymer CTEs can be attributed in part to intramolecular variables controlling molecular motions, such as chain segment rigidity and symmetry. Polymers with symmetrical molecular structure, for example, promote thermally-activated local chain motions. Solid-state NMR spectroscopy studies show the para-substitution of the 44DDS linkage in 44A promotes a thermally-activated ring flipping that is sterically-hindered in 33A at temperatures well below T_g .⁸¹ The steric hindrance stems from the non-symmetric meta-substituted diamine linkage, and also the increased efficiency of chain packing. Therefore intermolecular variables such as chain packing also affect a polymer's expansivity.

Heating a polymer through its T_g does not cause a discontinuity in volume, as first-order phase transitions such as boiling do; however, T_g does cause a change in the relationship volume shares with temperature. This is clearly exhibited in Figure 4.7, wherein a 33F cylinder was heated from approximately $T_g - 150$ °C to $T_g + 100$ °C. The abrupt change in slope near 150 °C suggest T_g is a second-order phase transition with

respect to volume.⁶⁵ The derivative of sample length with respect to temperature represents the second-order phase transition with a step change at T_g . To represent CTE, however, the sample's dimension change must be normalized to its original length. The change in length normalized to original length ($\Delta L/L_0$) is plotted in Figure 4.8, along with the first and second derivatives with respect to temperature. The second derivative peak represents the breadth of the glass transition as observed by expansivity measurements, which will be discussed in the subsequent section. Note the secondary Y axis is shared between the first and second derivative curves, which have units of $(^\circ\text{C})^{-1}$ and $(^\circ\text{C}^2)^{-1}$, respectively.

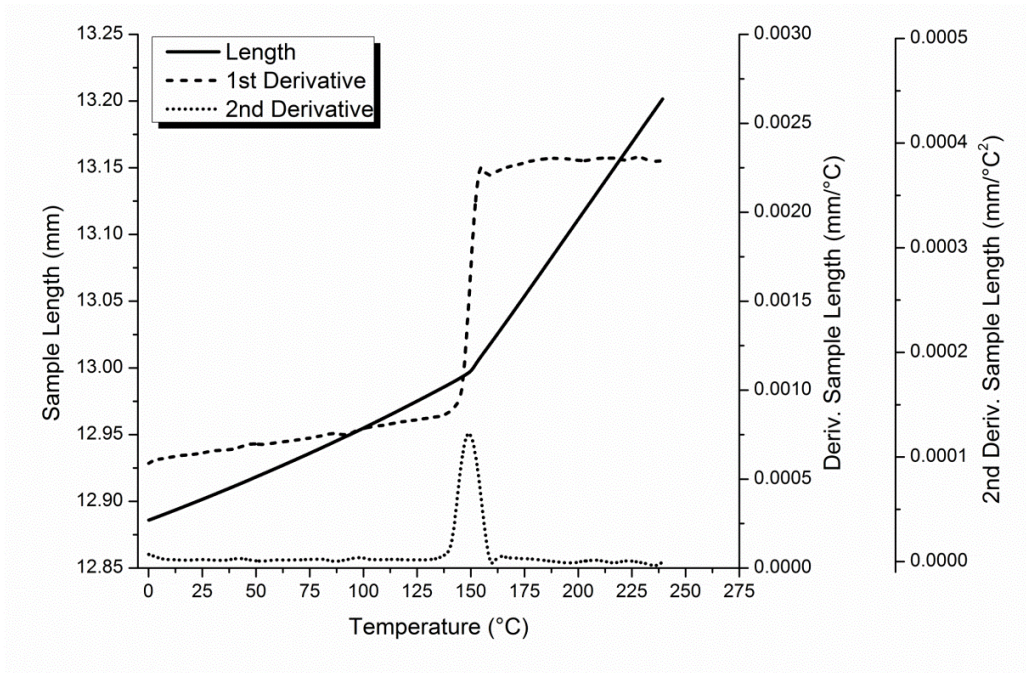


Figure 4.7 TMA plot of 33F sample length, first and second derivatives.

Cylinder dimensions were approximately 12.88mm height x 8.60mm diameter

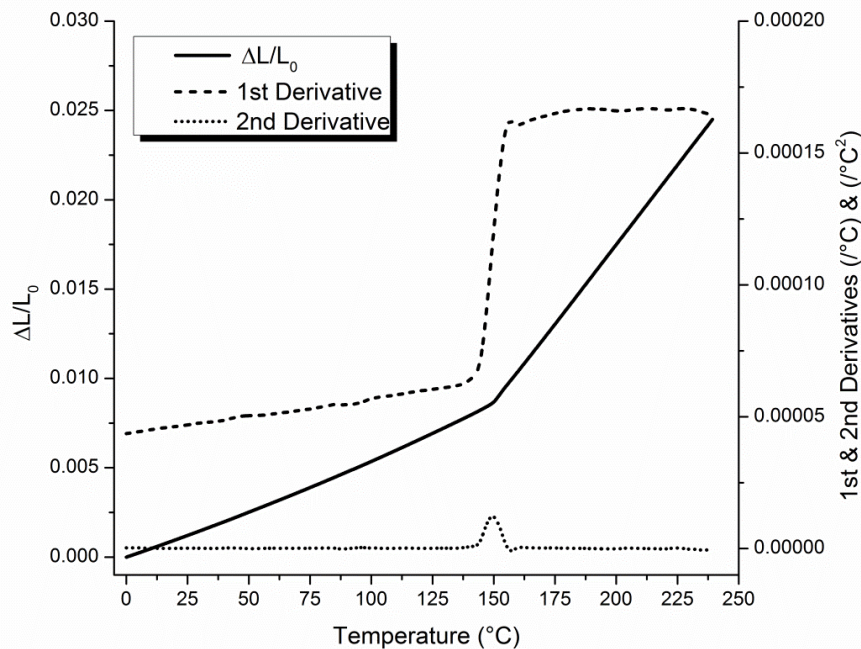


Figure 4.8 Dimension change and derivatives with respect to temperature.

Sample: 33F cylinder. Cylinder dimensions were approximately 12.88mm height x 8.60mm diameter

Shown below in Figure 4.9 is the thermal expansion behavior of the network isomer series upon heating to 240 °C. Table 4.6 lists the glassy and rubbery state CTEs for the network isomers series. Glassy state CTEs were taken from 50 °C to 100 °C, while rubbery state CTE was calculated from 225 °C to 250 °C. The trend of glassy state CTE with both density and average V_H suggests thermal expansion is primarily attributed to chain packing, with more loosely-packed networks undergoing accelerated expansion. Simulated experiments have suggested local chain motions, such as those active in sub- T_g relaxations, largely dictate the magnitude of the CTE in the glassy state.²⁸ Local sub- T_g motions are promoted through favorable molecular structural (i.e. axis of symmetry) and sufficient free volume. If CTE was attributed to simple vibrational motions of atoms and small chain elements, we would expect the meta-substituted diamine networks to exhibit

larger CTEs due to increased chain packing. Instead, the more rigid, loosely-packed para-substituted diamine networks show increased expansion coefficients in each case. This is attributed to their molecular structures which promote local glassy state motions and decreased chain packing. With increasing frequency and magnitude of local motions, chain segments occupy more volume, causing accelerated thermal expansion.

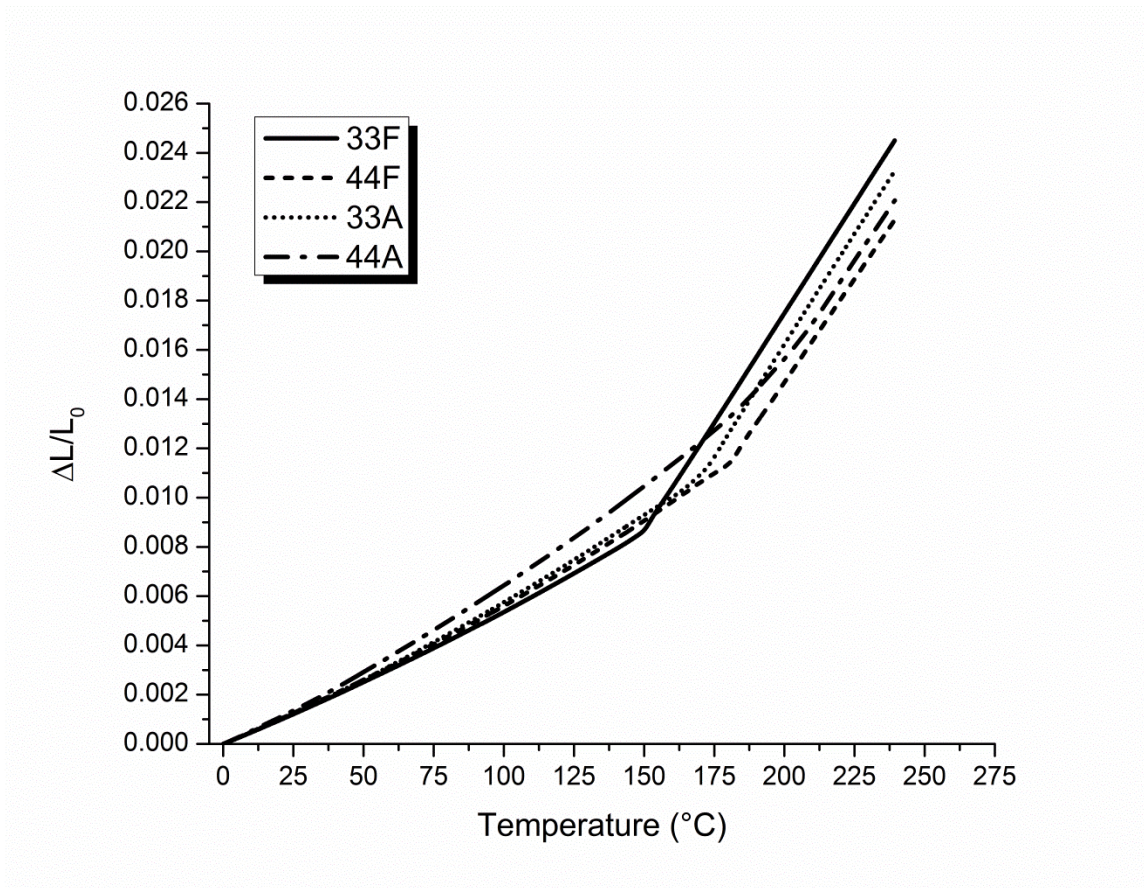


Figure 4.9 Thermal expansion of network isomer series.

Table 4.6

Thermal and architectural property relationships of network isomers.

Network	TMA T_g (°C)	Average hole size (V_H) at 23 °C (Å) ³	Linear Glassy CTE ($\mu\epsilon/^\circ\text{C}$)	Linear Rubbery CTE ($\mu\epsilon/^\circ\text{C}$)
33F	150 ± 2	67	57.2 ± 1.0	170.8 ± 2.9
44F	182 ± 1	76	59.3 ± 1.0	165.1 ± 2.0
33A	172 ± 2	77	62.1 ± 1.3	171.1 ± 2.4
44A	198 ± 3	82	70.0 ± 0.7	163.5 ± 3.3

The CTE of 44A is the greatest of the epoxy network series, explained by its rigid, symmetrical chain segments in conjunction with a high amount of free volume due to disrupted chain packing. Decreasing rigidity via a meta-substituted diamine, as in 33A, leads to increased chain packing which hinders local chain motions, thereby decreasing the glassy state CTE. This rigidity trend continues for 33F and 44F. The least rigid 33F network, which exhibits the lowest T_g , also has the lowest free volume and lowest glassy state CTE. This is irrespective of the fact that the temperature range of CTE calculation was nearest its T_g . An increase in rigidity caused by the para-substituted diamine in 44F corresponds with a measurable decrease in chain packing, and increases in T_g , free volume, and glassy state CTE. As with T_g and V_H , the glassy state CTEs of 44F and 33A are very similar. This further suggests their respective epoxy and amine components, while differing in structure, combine to form networks with similar rigidity. Through comparison of chemically-similar networks, this work establishes a clear effect of chain packing, which is heavily influenced by rigidity, on glassy state expansion behavior.

Network rigidity controls the efficiency of chain segment packing upon cooling from the rubbery state to below T_g . It is expected, therefore, that chain rigidity will also

influence network properties within the rubbery state. Indeed, additional isomeric differences can be observed in the rubbery state CTE, with networks cured with 44DDS showing decreased values. As discussed in regards to the glass transition, para-substituted networks have decreased configurational entropy relative to the meta-substituted networks. In the rubbery state, with sufficient energy allowing cooperative, long-range molecular motions, 33DDS network junctions allow for increased configurations that are not possible for the 44DDS networks. From prior discussion regarding free volume above and below T_g , molecular motions can only proceed with sufficient free space. As differences in free volume of structural isomers are limited to temperatures less than or equal to T_g , we propose increased configurational entropy is responsible for the increased rubbery state CTE in meta substituted networks. The finding of para-substituted isomers exhibiting lower expansivity in the rubbery state was also reported by Kaushik for DGEBF epoxy networks.⁹³ The trend of chain rigidity in the rubbery state CTE does not hold true in comparisons of DGEBF and DGEBA, however. The rubbery state CTE measurements show negligible differences in this temperature range, suggesting the DGEBA unit does not promote rigidity within the rubbery state as observed in the glassy state. Differing only by a methylene vs. isopropylidene bridge, the epoxy units have very similar configurational entropy and rubbery state rigidity, and therefore expansivity. Another possible explanation for this is the mixture of isomers present in the commercially-supplied DGEBF epoxy prepolymer investigated here. While an isomer distribution is not supplied, mixtures of para-para, ortho-para, and ortho-ortho are likely, while DGEBA is reported in much higher isomeric purity.^{133,134} Through ^1H nuclear magnetic resonance spectroscopy, mixtures of structural isomers were confirmed, with

para-para and ortho-para isomers as the primary components, and ortho-ortho present as a small fraction. This would lead to increased configurational entropy of DGEBF epoxy networks as compared to DGEBA. Differences in rubbery state CTEs did not reflect this, and overall differences between the epoxy networks were small and showed increased variability compared to glassy state measurements. Additional trials will be necessary to better understand the role of rigidity on rubbery state expansivity.

4.2.3.1 Polymer Fragility Considerations

Calorimetry experiments showed the glassy epoxy networks studied here differ in thermodynamic fragility, which we attributed to chain rigidity. The enthalpy change at T_g is greatest for 33F, the least rigid system with the lowest free volume is the most fragile. Through its relatively “flexible” backbone, it efficiently packs and hinders glassy state degrees of freedom, which brings about a large change in degrees of freedom upon entering the rubbery state. This was accompanied by the lowest glassy state CTE, regardless of proximity of the measurements temperatures to T_g . The most rigid epoxy-amine network, 44A, gains the fewest degrees of freedom as it undergoes the glass transition, giving it decreased thermodynamic fragility and more “strong” behavior. This was paired with the largest expansivity, attributed to promoted glassy state molecular motions. Despite structural dissimilarities, 44F and 33A show similar T_g , free volume, thermodynamic fragility, and glassy state CTE, suggesting they share similar network rigidities. The trend here shows that for chemically-similar materials, more rigid, symmetric structures shift the T_g to higher temperatures and limit chain packing. It also seems with sufficient free volume and symmetrical backbone linkages promote glassy state degrees of freedom through thermally-activated molecular motions, as evidenced by

thermodynamic fragility and further supported by glassy state CTE. The role of chain rigidity in thermally-activated molecular motions can be further probed with expansivity experiments.

Thermal expansion stems from increases in both free volume and thermally-activated molecular motions, with a small contribution from increased occupied volume. From the positive slope of the first derivative vs. temperature curve in Figure 4.8, it is clear the expansivity of 33F is not constant throughout the glassy state but rather increases with increasing temperature. We have established the network isomers studied here pack with varying degrees of efficiency, which we attribute to chain rigidity. These chain packing parameters scaled with glassy state CTE, allowing us to relate packing efficiency to expansivity behavior. Changes in CTE with temperature ($\delta\alpha/\delta T$) can offer additional insight to the role of chain packing and molecular structure in the thermally-activated molecular motions which influence thermal expansion.

From calorimetry and glassy state expansivity experiments, we hypothesize materials with greater thermodynamic fragility have suppressed changes in molecular motions in the glassy state. We note that increased degrees of freedom at $T > T_g$ would also increase thermodynamic fragility, though this was not supported by thermal expansion measurements. This leads to the hypothesis networks with hindered glassy state motions would be less sensitive to changes in CTE with temperature. This would correspond to an inverse relationship of $\delta\alpha/\delta T$ with thermodynamic fragility for $T < T_g$. Shown in Table 4.7 are CTE calculations for a single specimen of each network isomer over three $T < T_g$ temperature intervals. The sensitivity of CTE to temperature is represented by the glassy state CTE range, which correlates well with thermodynamic

fragility experiments. Although the temperature ranges are constant at 50 °C, the calculated CTEs show significant variation.

Table 4.7

Temperature dependence of network CTEs by TMA measurements.

Network	Thermodynamic Fragility	CTE 0-50 °C (μ ϵ /°C)	CTE 25-75 °C (μ ϵ /°C)	CTE 50-100 °C (μ ϵ /°C)	CTE Range (μ ϵ /°C)
33F	1.256 ± 0.003	50.1	53.5	56.5	6.4
44F	1.190 ± 0.003	51.9	55.7	59.7	7.8
33A	1.194 ± 0.002	52.3	56.7	61.2	8.9
44A	1.140 ± 0.001	58.2	65.2	70.1	11.9

The system with the greatest thermodynamic fragility, 33F, is the least sensitive to the CTE calculation temperature range, while the more “strong” 44A network is the most sensitive. Within the glassy state degrees of freedom increase with temperature as additional molecular motions become available and increase in frequency and/or magnitude. Increases in network rigidity disrupt chain packing and promote molecular relaxations. The combination of structurally-promoted sub- T_g motions and increased free volume causes CTE to change significantly with temperature, as additional degrees of freedom continue to develop. 44A shows significant sensitivity of CTE to temperature, while 44F and 33A exhibit similar CTE values and ranges. On the other hand, the CTE of the most fragile network 33F showed less variation with temperature, further suggesting suppressed degrees of freedom in the glassy state.

Shown in Figure 4.8 above are the first and second derivatives of dimension change with respect to temperature for 33F. The first derivative curve shows a positive slope below T_g , representing the temperature dependence of the glassy state CTE ($\delta\alpha/\delta T$).

The slope of $\delta\alpha/\delta T$ vs. temperature represents the rate at which CTE changes with temperature (also by the non-zero value of $\delta^2\alpha/\delta T^2$). This was averaged from 0-100 °C for all four networks, and listed in Table 4.8. The trend for the slope of $\delta\alpha/\delta T$ agrees well with the glassy state CTE ranges shown in Table 4.7, with 33F the having the smallest slope, and increasing with chain rigidity from 44F to 33A to 44A. In a similar manner, the second derivative with respect to temperature produces a peak at T_g , the breadth of which represents the rate at which $\delta\alpha/\delta T$ changes through the glass-to-rubber transition. FWHH measurements of this peak, listed in Table 4.8, suggest the changes in thermal expansivity at T_g also relate to network rigidity. In calorimetry experiments, thermodynamic fragility shared a trend with network rigidity, with the most rigid networks showing lesser gains in degrees of freedom at T_g due to promoted molecular motions in the glassy state. Thermal expansion measurements supported this, with more rigid networks expanding with temperature at a greater rate. Expansivity experiments further support the relationship of network rigidity to changes in molecular motions through the glassy state and glass transition, wherein more rigid networks undergo the glass transition over the broad temperature range. This change in CTE through the glass transition is reflected by thermodynamic fragility measurements, and again trends with network rigidity. Put simply, the CTE at temperatures slightly above or below T_g is more similar for rigid systems. As the most rigid network, the rate change in expansivity of 44A is slow and broad, while the least rigid 33F network changes rapidly and over a narrow temperature range.

Table 4.8

Rate of change of CTE and breadth of glass transition by TMA.

Network	Thermodynamic Fragility	CTE Range ($\mu\epsilon/^\circ\text{C}$)	$\delta\alpha/\delta T$ Slope 0-100 $^\circ\text{C}$ ($\mu\epsilon/^\circ\text{C}^2$)	FWHH of $\delta^2\alpha/\delta T^2$ Peak ($^\circ\text{C}$)
33F	1.256 ± 0.003	6.4	0.131	4.5
44F	1.190 ± 0.003	7.8	0.171	10.3
33A	1.194 ± 0.002	8.9	0.172	9.4
44A	1.140 ± 0.001	11.9	0.238	35.4

From the above comparisons, we have strong evidence to suggest increased chain rigidity disrupts packing and increases free volume. Therefore chain rigidity and chain packing influence the prominence of molecular relaxations in the glassy state and the rate at which network properties change with temperature. Increased chain packing and non-symmetrical molecular linkages suppresses local motions, hindering the rate of expansion in the glassy state, and causing a more abrupt change in expansivity at the glass transition. In these cases, the onset of the α -type process quickly dominates expansion behavior, as observed with the more constant CTE in the glassy state and more rapid change of CTE through the glass transition for 33F, 44F, and 33A. In the case of 44A, we speculate the high rigidity and inefficient packing of chain segments corresponds with local motions contributing heavily to thermal expansion, as shown by low thermodynamic fragility, significant dependence of CTE with temperature, and broad T_g temperature range. Increased chain rigidity causes local β -type motions to continue influencing thermal expansion further into the glass transition as longer range, alpha-type processes develop. The simultaneous occurrence of β and α -type processes is well established for linear amorphous glassy polymers, in which the degree of β vs. α -type

splitting varies with intra- and intermolecular factors.⁸⁸ The convolution of β vs. α -type processes is suggested in 44A by the non-uniform first derivative and bimodal second derivative curves, as shown below in Figure 4.10. The first derivative curve shows a slight undulation near what would be expected to be an inflection point, as observed for the more fragile 33F network in Figure 4.8. Similarly, the second derivative curve is bimodal. While these may be an effect of the linear least squares fitting method, they suggest small changes in the rate of expansivity with temperature through the broad glass transition. It is possible the glass transition of this relatively “strong” polymer network proceeds through multiple mechanisms, such as overlapping β vs. α -type processes, known as $\alpha\beta$ -splitting.⁸⁸ We hypothesize $\alpha\beta$ -splitting behavior also relates to network rigidity and fragility, although additional studies are necessary.

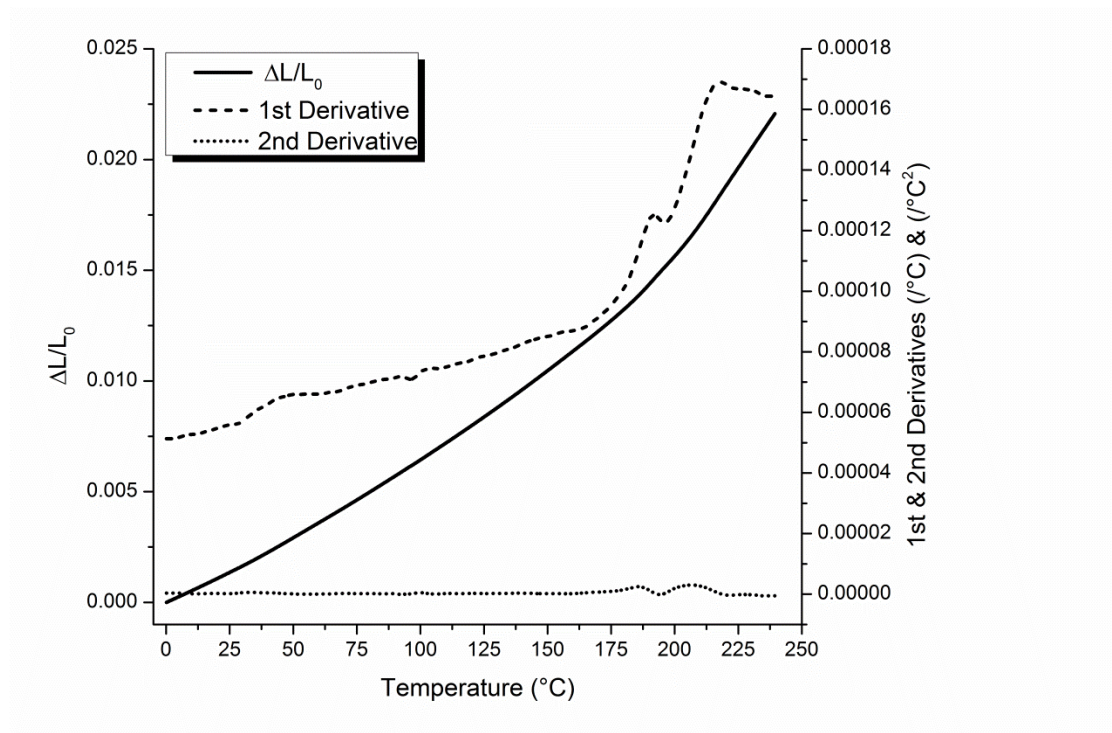


Figure 4.10 Thermal expansion and derivatives of 44A with respect to temperature.

4.2.3.2 Influence of Network Connectivity

4.2.3.2.1 Difunctional vs. Multifunctional Epoxy Prepolymers

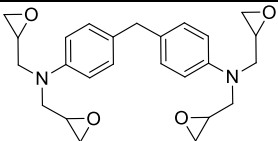
While chain rigidity has received significant interest in linear glassy amorphous polymers,⁹² the role of rigidity in the properties of glassy amorphous polymer networks is less well known.⁹³ The relationship of chain rigidity to T_g is well established, wherein long range molecular mobility is shifted to a higher temperature with more rigid molecules. This suggests thermal energy is dissipated through short range motions in more rigid polymers, shifting the onset of cooperative motions and long-range flow to higher temperatures. In addition to molecular linkages, changes in network connectivity can also bring about changes in chain rigidity.

Chain rigidity dictates molecular motions, especially the ability of chain segments to pack as they cool to the glassy state. Chain packing affects the prominence of glassy state molecular motions, as well as the proximity for intermolecular interactions upon heating. To probe the influence of intermolecular interactions, researchers have studied linear and network polymers of variable crosslink density. In some cases increased crosslink density corresponds to increases in bulk density, though this is not always the case, and alterations in chain packing must be considered when correlating crosslink density to network properties.^{135,136} As shown in density measurements of network isomers, chain packing affects the free volume and thermal expansion behavior. While some studies have correlated CTE with crosslink density,^{137,138} others suggest glassy state expansivity is not significantly different between chemically-similar linear and network polymers.²⁰ The formation of covalent bonds between adjacent chain segments is presumed to increase local chain rigidity, though the length scale of mobility alterations

must be relevant to the properties of interest. As established in the previous section, increased chain rigidity with constant crosslink density decreases packing efficiency. This leads to increased free volume and additional glassy state molecular motions. Chain segment rigidity, therefore, may be influential to CTE insofar as its ability to alter intermolecular interactions via chain packing.

Table 4.9

Multifunctional epoxy prepolymer.

Chemical Structure	Abbreviation	Molecular Weight (g/mol)
	TGDDM	422.5 EEW: 109-116

EEW: Epoxide equivalent weight.

A comparison of DGEBF and a chemically-similar tetrafunctional analogue, tetraglycidyl-4,4'-diamino-diphenyl methane (TGDDM, structure shown in Table 4.9) affords the ability to probe the effect of network connectivity of rigid, highly aromatic polymer networks. While differing in oxygen vs. nitrogen content, the most significant difference between the epoxy prepolymers is their functionality. DGEBF is a difunctional molecule, while TGDDM has oxirane functionality between ~3.9 and 4 per molecule, leading to polymer networks of significantly increased connectivity. With additional crosslinking sites, the polymer chain segments behave more rigidly with respect to T_g , with increases of nearly 100 °C for both DDS networks isomers. Increased network connectivity also correlates to decreases in V_H , suggesting chains are forced to pack more tightly.⁹³ Comparisons between DGEBF and TGDDM network isomers are shown in Table 4.10.

Table 4.10

Thermal property comparison of DGEBF and TGDDM network isomers.

Network	T _g (°C)	Density (g/cm ³)	CTE 0-50 °C (μ ϵ /°C)	CTE 25-75 °C (μ ϵ /°C)	CTE 50-100 °C (μ ϵ /°C)	CTE Range (μ ϵ /°C)
33F	158	1.274	50.1	53.5	56.5	6.4
44F	184	1.266	51.9	55.7	59.7	7.8
33TGDDM	260	1.280	47.6	50.9	55.4	7.8
44TGDDM	284	1.277	51.4	54.9	58.3	6.9

TGDDM networks show the same trend as DGEBF networks wherein the para-substituted diamine corresponds with an increased T_g and glassy state CTE, and decreased bulk density. Despite increased network connectivity, the sensitivity of CTE calculations to temperature range is very similar. Considering DGEBF and DGEBA isomers, CTE dependence on temperature was attributed to chain segment rigidity disrupting chain packing, allowing additional glassy state motions. This was particularly evident in comparisons between the least and most rigid networks, 33F and 44A, respectively. In this case, increased network connectivity is presumed to increase chain rigidity, though this is accompanied by an increase in chain packing.⁹³ Although increased network connectivity increases rigidity, it seems, in this case, increased packing subdues thermal expansion, and causes the two networks to show very similar thermal expansion behavior, despite measurable differences in physical and mechanical properties. It would be interesting to probe differences in expansivity in the rubbery state between these networks; unfortunately, the crosslink density of TGDDM networks is so high that full conversion (100% cure) is not possible without also causing thermal degradation. As the T_g of semi-cured TGDDM networks is approached, the curing

reaction continues, making rubbery state measurements, such as FFV and CTE studies, not possible.

4.2.3.2.2 Alternative curing schedules

The expansivity of polymers involves a complex relationship between chain rigidity, chain packing, and free volume. While comparisons of DGEBF and TGDDM showed increased chain packing caused small, if not negligible changes in glassy state CTE, comparisons of fully cured and under-cured glassy networks show a different relationship. Specifically, 44A cured by an industrially-relevant cure cycle (IC), which involves a 1 °C/min temperature ramp to 177 °C for 3h, shows a significantly higher density, while also having a decreased T_g and glassy state CTE, seen in Table 4.11. At lower conversions of oxirane and amine functional groups, evident by the decreased T_g , on average chain segments are able to better pack, which decreases V_H and inhibits thermal expansion. This has been shown before in highly crosslinked epoxy networks, wherein increases in conversion decreased room temperature density, attributed to fully-cured network topology constraining chain segments in a low-density configuration after cooling to the glassy state.¹³⁹ Additionally at lower conversions, chain segments are less rigid and more chain ends are present which is known to lower the T_g .⁶⁵ Interestingly, 44A cured by this cure schedule shows a similar T_g , average free volume hole size (77 Å³) and glassy state CTE to fully-cured 33A. This suggests the under-cured 44A shares similar network rigidity to fully-cured 33A.

Table 4.11

Thermal property comparison of DGEBF and TGDDM network isomers.

Network	DSC T _g (°C)	Density (g/cm ³)	Average V _H at 23 °C (Å) ³	Linear Glassy State CTE (με/°C)
44A-IC	175	1.264 ± 0.002	77	66.9
44A	224	1.231 ± 0.001	82	70.1

Thermal expansion experiments have corroborated calorimetry and network architecture data with respect to chain rigidity. More rigid chains resist configurational changes during network formation and glassy state cooling, which causes increased free volume (V_H and FFV) compared to less rigid structural isomers. Beyond this, para-substituted networks benefit from a single axis of rotation along the backbone, allowing for additional degrees of freedom through molecular motions within the glassy state. This decreases their thermodynamic fragility, broadens the temperature range of the glass transition, increases the glassy state CTE, as well as $\delta\alpha/\delta T$. Glassy state CTE was shown to depend mostly on chain packing, suggesting increased chain packing and decreased free volume hinder the molecular motions which drive thermal expansion. While these studies have strongly suggested differences in glassy state molecular motions, they have not directly been investigated. The subsequent section will investigate thermomechanical relaxations of the epoxy network isomers through small strain experiments.

4.2.4 Effect of Network Rigidity on Mechanical Relaxations

DGEBA and DGEBF epoxy prepolymers have been well-studied in combination with 3,3'- and 4,4'-DDS regarding various thermal, mechanical, environmental, and volumetric properties. Despite being chemically very similar, we have shown these

polymer networks have very different thermal and physical properties. Previous discussion has focused on the effect of chain rigidity on network architecture and thermal properties. Chain rigidity, defined as the propensity for molecular segments to undergo conformational changes, has been shown to cause significant differences in chain packing efficiency as well as key thermal properties such as T_g and CTE. In a similar manner, we hypothesize the mechanical relaxation response to small strains will depend on chain rigidity.

Chain rigidity influences packing efficiency and similarly influences a material's elastic behavior. The storage (E') and loss (E'') moduli represent the in- and out-of-phase components of the material's response to a sinusoidal stress, respectively (Equations 5 and 6 below). The phase lag between stress and strain, δ , represents the energy dissipation (or dampening) behavior of the material, where $\tan\delta$ represents the ratio of the storage and loss moduli. The relationship of $\tan\delta$ with temperature is, therefore, representative of the material's energy dampening capabilities. Shown in Figure 4.11 is the storage modulus vs. temperature relationship for all DGEBF and DGEBA network isomers. The storage modulus represents the in-phase, elastic response of material to the sinusoidal applied stress. At low temperatures, well below the T_g of all systems, the network isomers have very similar storage moduli values. With increasing temperature, the storage moduli of the para-substituted networks decrease at an accelerated rate,

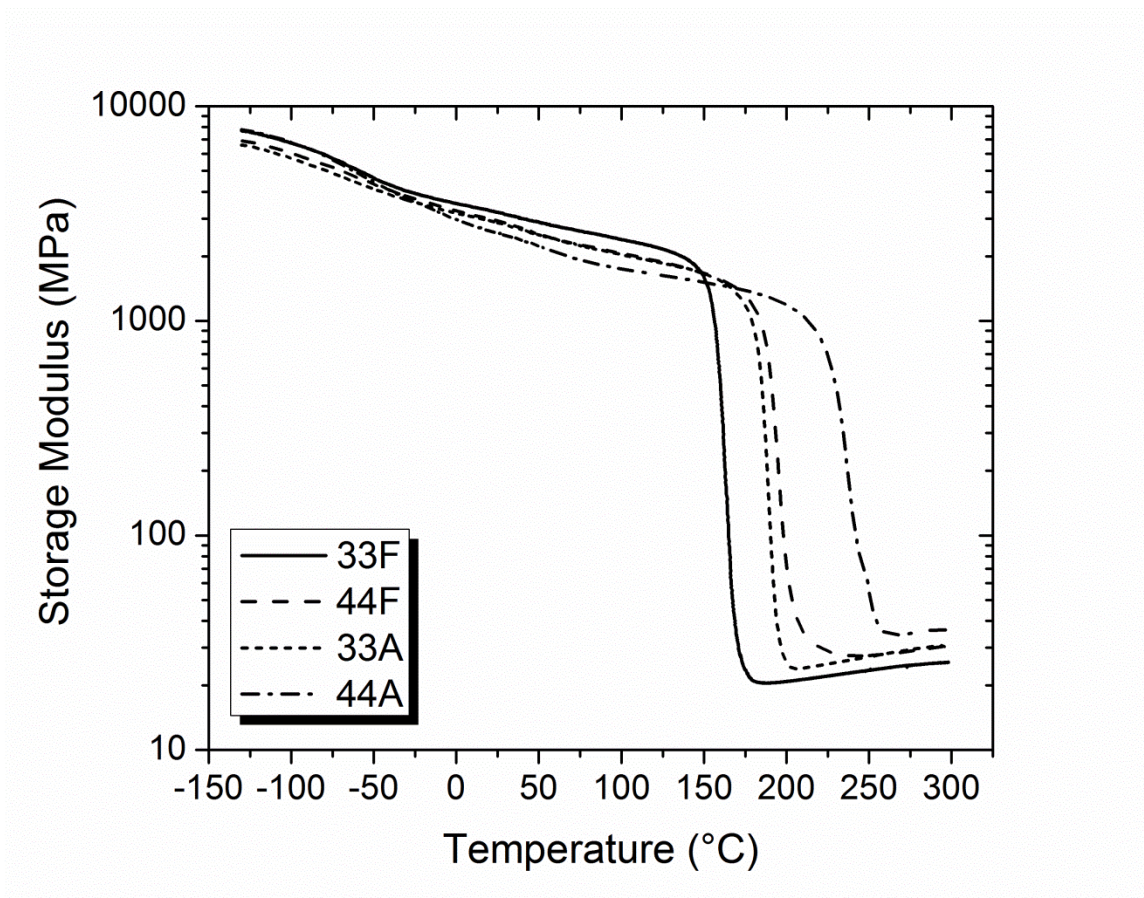


Figure 4.11 Storage modulus curves at 1Hz for network isomer series.

attributed to their decreased chain packing efficiency. As shown in previous analysis, this decline in elastic performance with temperature is not accompanied by a decrease in thermal properties, with para-substituted networks exhibiting larger T_g s. Calorimetry studies suggested the more rigid networks have additional degrees of freedom in the glassy state, which may serve as energy dissipation mechanisms under applied stress. This was further supported by thermal expansion studies, wherein the increased CTE of para-substituted networks was due to their increased rigidity which, in addition to decreased chain packing, promotes glassy state molecular relaxations and therefore more rapid decline of in-phase stress response upon heating.

$$E' = \frac{\sigma_0}{\varepsilon_0} \cos\delta \quad (5)$$

$$E'' = \frac{\sigma_0}{\varepsilon_0} \sin\delta \quad (6)$$

Above T_g , the magnitudes of E' reflects chain rigidity very well, with 33F showing the lowest elastic performance and 44A the most. In the rubbery state, chain packing can be considered equal as all networks have entered an equilibrium state with sufficient energy and degrees of freedom to adopt energetically-favorable conformations. Mechanical elasticity in this region is therefore driven by network rigidity more so than chain packing.

Sub- T_g molecular relaxations such as the γ and β transitions are representative of a material's modes of energy dissipation in the glassy state. By definition, a relaxation involves some form of energy loss or dissipation under an imposed force field. The maximum value of a relaxation peak corresponds to the temperature at which the frequency of an applied stress equals the inverse relaxation time.⁶⁵ At a given temperature molecular motions which occur on the same timescale as the sinusoidal applied stress will appear as a temperature-dependent relaxation in the out-of-phase loss modulus (or $\tan\delta$), causing a peak. Shown in Figure 4.12 are E'' vs. temperature curves for 33A tested at four different frequencies: 0.1, 1, 10, and 100 Hz. Each frequency curve shows a large peak relating to the γ relaxation occurring on the timescale of each inverse frequency (i.e. 10, 1, 0.1, and 0.01 seconds), with the peak maximum increasing with increasing frequency, as listed in Table 4.12. For the timescale of the activated molecular relaxations

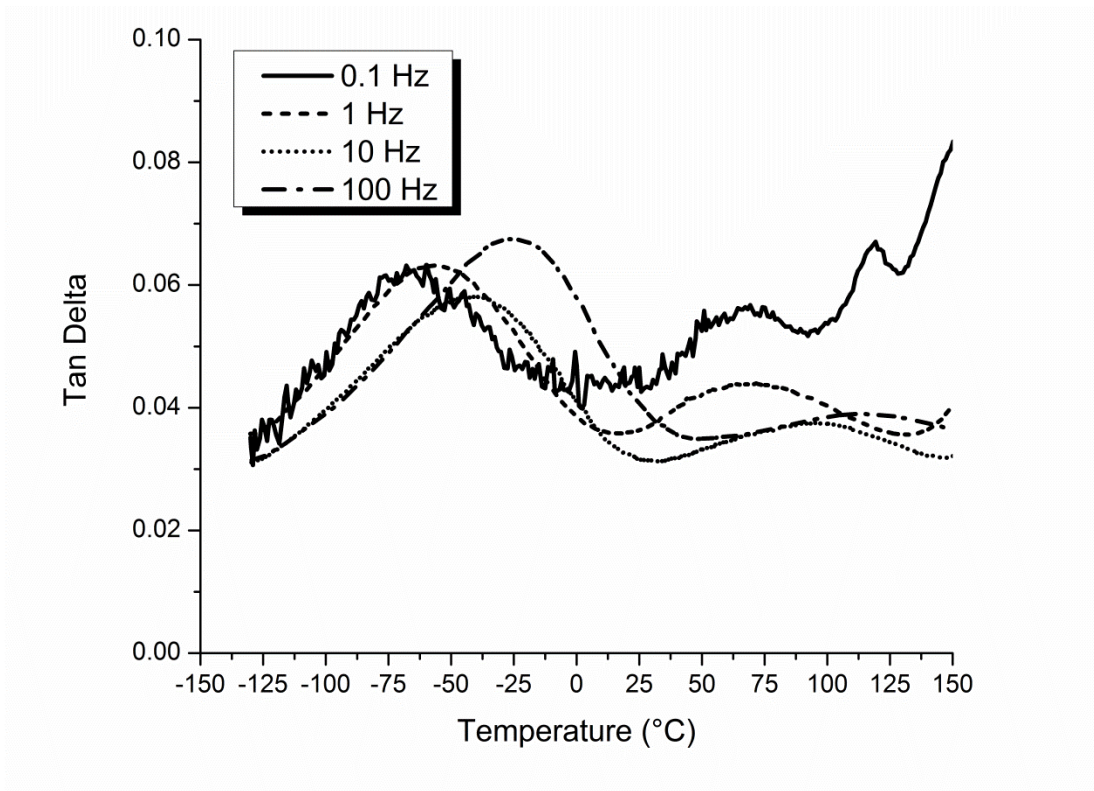


Figure 4.12 DMA frequency sweep for $\tan\delta$ curves of 33A.

Table 4.12

DMA frequency sweep for sub- T_g relaxations from 33A $\tan\delta$ curves.

Frequency (Hz)	γ Peak Max Temperature ($^{\circ}\text{C}$)	β Peak Max Temperature ($^{\circ}\text{C}$)
0.1	-67.9	50.9
1	-56.6	70.5
10	-39.2	95.6
100	-26.9	109.3

to resonate with the frequency of the applied stress, more energy (temperature) is required. Also present in each frequency curve is a small peak indicative of a β transition, with the peak maximum increasing from approximately 50 to 105 $^{\circ}\text{C}$. In amorphous glasses, the β transition is associated with cooperative motions, such as short range

rearrangements between crosslinking sites.^{82,97,140} In contrast, the γ is understood to exist on a much smaller size scale.

The relationship of $\tan\delta$ with temperature is representative of the material's energy dissipation (dampening) capabilities and a common to probe mechanical relaxations over broad temperature ranges. Figure 4.13 shows $\tan\delta$ vs. temperature curves for the network isomer series within the glassy state. Initial comparison of DGEBF and DGEBA isomers suggests the para-substituted networks have a more intense γ peak. This increased viscoelastic response through short, local motions deep in the glassy state is corroborated by previous observations in thermodynamic fragility, CTE, and $\delta\alpha/\delta T$. Further, decreased chain packing compared to meta-substituted networks promotes the molecular relaxations necessary for energy dissipation. Interestingly, the β peak, which occurs near 70 °C, is increased for the 33DDS networks relative to the 44DDS networks. To understand differences in β peak intensities we must consider the change in the storage moduli of the network isomers with temperature, shown in Figure 4.11. Storage moduli magnitudes of para-substituted networks decrease more rapidly with temperature. As the temperature increases to the β transition range, differences in storage moduli between 33F and 44F, and 33A and 44A become significant. Increased storage moduli magnitude decreases $\tan\delta$, the ratio of E'' and E' , which is especially significant for low-intensity peaks, such as the β peak. Due to differences in E' magnitudes in this temperature range, the loss moduli curves allow for more direct comparison of the out-of-phase, energy-dissipating behavior of the network isomers.

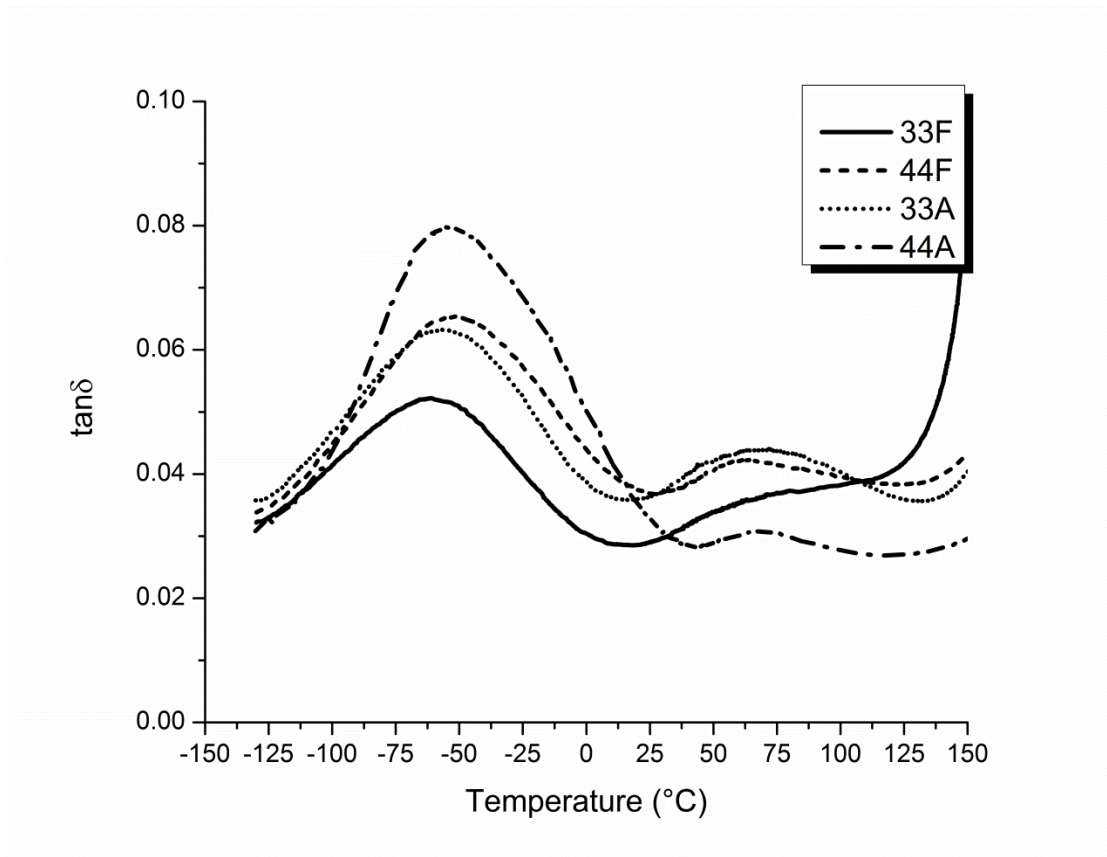


Figure 4.13 Tan δ sub- T_g relaxations at 1Hz for network isomer series.

Figure 4.14 shows E'' vs temperature curves at 1 Hz for the network isomer series over the entire relevant temperature range. From these curves, the prominence of the β transition is low for all networks, though most prominent in 44F and 33A. In fact, the β peak is nearly non-existent in both 33F and 44A curves. As previously mentioned, the β relaxation in glassy polymer networks is hypothesized to arise from molecular motions with some amount of cooperativity, such as involvement of nearby chain segments. With β relaxation peaks absent for the most rigid as well as least rigid networks, it seems there was insufficient energy for cooperative motions to proceed in each case. In the case of 44A, we attribute this to high network rigidity which requires significant energy to insight cooperative motions. In DMA experiments, the applied sinusoidal stress adjusts in

value to maintain a constant strain (0.05%). This causes lower stress levels, and therefore less energy is input into the sample throughout this temperature range. Thus the rigid para-substituted network lacks a prominent β relaxation peak under these conditions. For 33F, we propose cooperative motions are hindered by efficient chain packing, wherein the energy levels are insufficient to overcome this activation barrier.

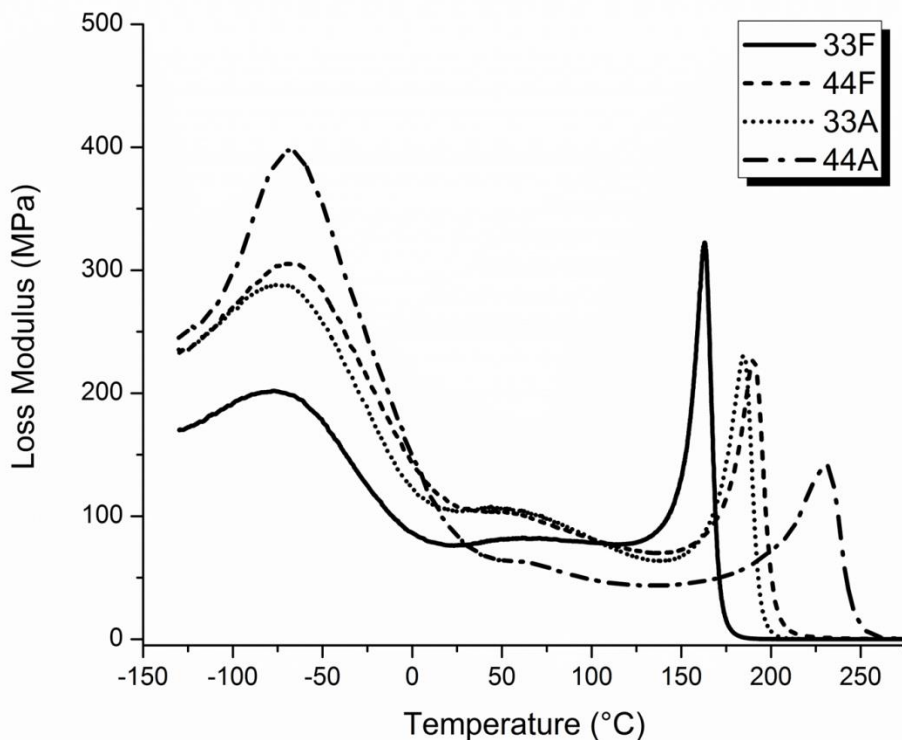


Figure 4.14 Loss modulus sub- T_g transitions of network isomer series.

Sub- T_g relaxations, such as the γ and β transitions shown here, show a frequency-transition resonance (peak maximum) at variable temperatures depending on the frequency of the applied sinusoidal stress. For a molecular relaxation to occur at decreasing timescales, additional energy (i.e. temperature) is required. The relationship of peak temperature and frequency of applied stress follow Arrhenius-type dependence.¹⁴¹

The Arrhenius equation is as follows:

$$\log \frac{f}{f_0} = -\frac{2.3E_A}{R} \left[\frac{1}{T} - \frac{1}{T_0} \right] \quad (7)$$

where T and T₀ are the temperatures (in Kelvin) at which a peak maximum occurs in the E'' (or tanδ) curves for the applied stress at frequencies f and f₀. Variables R and E_A represent the gas constant and apparent activation energy, respectively. Therefore, with the multiple frequencies employed here, and activation energy can be calculated for a given relaxation with respect to a reference frequency and temperature. Peak temperatures shift to higher temperatures with increased frequency, which allows for the calculation of the activation energies for the γ relaxation of the E'' curve, and are listed in Table 4.13.

Table 4.13

Loss modulus γ peak temperatures and apparent activation energies.

Network	0.1 Hz Peak (°C)	1 Hz Peak (°C)	10 Hz Peak (°C)	100 Hz Peak (°C)	E _A (kJ/mol-K)
33F	-72.2	-67.2	-48.1	-38.8	13.6
44F	-77.6	-65.8	-45.6	-32.4	10.8
33A	-78.5	-63.3	-49.7	-36.6	11.8
44A	-71.6	-65.5	-42.2	-18.0	9.6

In this case, 1 Hz was chosen as the reference frequency. Continuing with previous trends, the most rigid network, 44A, shows the lowest apparent activation energy for the γ relaxation, with increasing E_A for more tightly packed networks. This is an expected result, as previous thermal, physical, and thermomechanical experiments have suggested 44A possesses additional degrees of freedom in the glassy state that are significantly hindered in 33F, 44F, and 33A by increased chain packing. We hypothesize the rigid molecular linkages in combination with sufficient free volume necessitates that γ

relaxations occur over longer scales, such as chain segments between crosslinking junctions, facilitating greater energy dissipation at these low temperatures.

Another interesting feature of Figure 4.14 is the magnitude of the α relaxation peak. Showing a similar trend as the E' curves in the rubbery state, the intensity of the α relaxation peak follows that of network rigidity, with 33F showing the highest peak intensity and 44A showing the least, with 44F and 33A exhibiting very similar peaks. Even more, the magnitude of the γ relaxation relative to the T_g α relaxation also reflects network rigidity. The largest γ relaxation peak in 44A is paired with the least intense α relaxation peak, and vice versa for 33F. The γ and α relaxation peaks originate from different molecular events. Deep in the glassy state, the γ relaxation is attributed to short range glassy state motions promoted by inefficient chain packing. Upon entering the rubbery state, however, mechanical relaxation now occurs via longer range cooperative motions which occur to a lesser extent in more rigid networks.

4.2.4.2 Polymer Fragility Considerations

As with calorimetry and expansivity experiments, thermomechanical relaxation also reflects network property changes through the glass transition. DMA is often used as a tool for dynamic fragility measurements, in conjunction with dielectric spectroscopy, to extract segmental relaxation times close to T_g . Relating dynamic fragility to chemical structure remains a challenge, particularly for comparisons between chemically-dissimilar materials. Recently Huang and coworkers established correlations between E' , E'' , and $\tan\delta$ curve features with the traditional dynamic fragility parameter, m .¹⁴² Specifically, they showed relatively “strong” glass-forming polymers show steady changes in E' with temperature as well as increased breadth of E'' and $\tan\delta$ α relaxation

peaks. We observed similar behavior in the epoxy networks studied here, where the most fragile 33F network exhibited a relatively constant E' with temperature, but showed the most intense and narrow α relaxation peak. The E' curve of the relatively “strong” 44A network varied more significantly with temperature and showed a much more broad α relaxation peak. Peak breadths of the E'' α relaxation peaks are listed in Table 4.14, and trend with previous thermodynamic fragility calculations. These comparisons show a clear relationship between chain rigidity and polymer fragility in these glassy amorphous epoxy networks.

Table 4.14

DMA loss modulus α peak analysis.

Network	α Peak Maximum (°C)	α Peak FWHH (°C)
33F	163.0	11.7
44F	190.3	16.8
33A	184.8	15.5
44A	231.2	22.7

Peaks were analyzed from curves generated at a 1 Hz frequency.

While small strain analysis is useful for increased understanding of network responses to applied stress, the energy input into the system is relatively small, and the molecular motions observed in the glassy state are an indirect probe of rigidity. By definition, polymer chain rigidity is the polymer’s resistance to conformational changes. Small strain analysis probes molecular relaxations of increasing length scales from γ , to β , to α through simultaneous variation of temperature with applied stress, with the α relaxation correlating to long range molecular motions and conformational changes associated with T_g . To probe network rigidity within the glassy state, we will next explore the network series by means of mechanical testing. Through studies of network strain

performance in compression and tension, at ambient and elevated temperatures, we will observe deformation processes which directly relate to chain rigidity.

4.3 Conclusions

The epoxy network isomers investigated here offer a unique research space to probe thermal, architectural, and thermomechanical properties which arise from the complex interaction of intra- and intermolecular factors. Chain rigidity at the molecular level has profound influences on polymer properties, including T_g and chain packing. More rigid molecular backbones, especially those with a single axis of symmetry, possess a higher T_g . Researchers have attempted to explain this through various approaches. Additional glassy state degrees of freedom, for example, may allow polymer networks to dissipate thermal energy through simple, local molecular motions, such as ring flips of phenylene groups, delaying the onset of T_g upon heating. Alternatively, upon cooling from an equilibrium rubber state chain segments with additional configurational entropy, such as the meta-substituted networks studied here, are able to cool to lower temperatures before the configuration entropy of the glassy and rubbery states becomes equal and T_g is realized. Even more, researchers have shown more rigid polymers require a greater minimum percent free volume to remain in rubbery state and thus on cooling undergo the glass transition at higher temperatures. These studies have strongly supported the theory that T_g is primarily determined by chain rigidity.

Also affected by rigidity is chain packing, which determines network architecture and thermomechanical properties. Increases in chain rigidity corresponded with decreases in chain packing, evidenced by bulk density and V_H of network isomers. The packing efficiency, in turn, affects the molecular motions available to the polymer networks

within the glassy state. Glassy state CTE scaled well with free volume measurements, which suggests the relationship between local molecular motions and CTE is complex. Sufficient free space is required for molecular motions to occur, the frequency and magnitude of which influence thermal expansivity. More rigid chain segments with less efficient packing promote glassy state molecular motions upon heating, which causes accelerated thermal expansion compared to more densely packed networks. The rate at which CTE changes with temperature supports this as well, wherein the least rigid, most densely-packed network showed the lowest and most constant glassy state CTE despite calculations at temperatures near its T_g . This study established a clear role between glassy state CTE and chain packing, which is heavily influenced by chain rigidity. Interestingly throughout all studies performed, structurally-dissimilar networks shared very similar behavior suggesting the combination of their constituents forms a similar network in regards to rigidity as evident by calorimetric, free volume, and thermomechanical measurements.

Throughout *Chapter IV*, we have made some bold claims regarding chain segment rigidity, though we have not conducted, in any exhaustive manner, experiments which directly probe resistance to conformational changes. To better probe this network rigidity, we need to explore the strain performance of the glassy epoxy networks. The following chapter will employ mechanical and strain recovery experiments wherein the material's response offers additional evidence to chain rigidity differences within the network isomer series. Further, we will continue establishing relationships which relate directly to chain rigidity, and others which are secondarily affected through chain packing efficiency.

CHAPTER V – ROLE OF CHAIN RIGIDITY IN GLASSY STATE DEFORMATION

PROCESSES OF AMORPHOUS POLYMER NETWORKS

5.1 Introduction

Aromatic epoxy-amine polymer networks are common building blocks for structural composite matrices due to their high thermal and mechanical properties. It is, therefore, critical to understand their mechanical performance and modes of deformation for the advancement of composites science and engineering. Depending on the architecture of the polymer network, the molecular motions and deformation mechanisms associated with energy storage or dissipation can differ greatly. *Chapter IV* discussed at length the role of chain rigidity in the thermal, architectural, and thermomechanical properties of highly crosslinked epoxy network isomers. Numerous relationships were established regarding properties driven primarily by molecular structure and rigidity. By the definition of resistance to configurational changes, rigidity of chemically-similar amorphous network yields sizeable differences in T_g s. Network architecture corroborated this, showing increased network rigidity decreased chain packing efficiency, which in turn caused thermomechanical properties to reflect promoted glassy state motions. This lead us to conclude that certain properties are primarily driven by chain rigidity, while others are driven more by network architecture (i.e. chain packing) as a consequence of rigidity. To more concretely establish these roles, this chapter will probe the strain performance of the epoxy network isomer series.

Gamma (γ) and beta (β) relaxations have been correlated via solid state NMR spectroscopy, dielectric analysis, and DMA to local glassy state motions specific to the chemical isomers of DGEBA network isomers studied here.⁸¹ A number of molecular

motions have been proposed to relate to γ relaxation, including crankshaft motions of the hydroxypropyl ether groups and phenylene ring flips. While there is strong evidence for their occurrence, it is argued that mechanical energy dissipation cannot proceed to any significant extent via simple motions such as phenylene ring flips, considering the identical configurational states before and after flipping.⁸⁷ The energy barriers associated with such simple motions cannot account for the large stress fields applied during mechanical loading. Higher energy motions, such as those relating to the β relaxation, have been attributed to larger, more cooperative cone-like motions of chain units, such as a cone-like rotation of the DGEBA unit of DGEBA-DDS networks. While these molecular relaxations may hold a role in the polymer deformation mechanisms at hand, under high-stress situations, additional motions are likely activated which cannot be observed in tests which apply small (or zero) stress. Mechanically-activated relaxations will likely arise from flexible chain segments which may undergo local rearrangements and configurational changes.

In-situ techniques which probe activated molecular motions in high-stress situations are not possible, making the assignment of high-stress mechanically-activated motions complicated. Because of this, post-deformation analysis is an appropriate approach to identification of polymer deformation pathways. From their associated energy barriers, strains can be separated into components recoverable immediately upon load unloading, at extended time at the deformation temperature, upon heating to temperatures above the deformation temperature, and upon heating to T_g . The distribution of these strain components sheds light on energy storage and dissipation mechanisms active during a deformation event. The works of this chapter will use calorimetric,

mechanical, and thermomechanical techniques to probe differences in performance which can be attributed to chain segment rigidity within highly crosslinked glassy polymer networks.

5.2 Results and Discussion

5.2.1 Effect of Network Rigidity on Mechanical Properties

As discussed in *Chapter IV*, DGEBF and DGEBA epoxy network isomers form measurably different network architectures due to chain rigidity. This is manifested in the decreased bulk density as well as increased free volume (V_H and FFV) in more rigid networks which pack relatively inefficiently. Chain packing has a significant effect on mechanical properties such as the elastic modulus and yield strain of the glassy polymer networks. Previous work in our group has shown measurable differences in the mechanical properties of DGEBA network isomers.⁷⁰ Here we will continue evaluation of these systems, as well as the additional DGEBF network isomers, to elucidate additional physical and mechanical properties which arise from chain segment rigidity.

5.2.1.1 Relationship of Chain Rigidity and Elastic Modulus

Due to the chemical similarity of the investigated epoxy networks, differences in mechanical properties are more easily understood than comparisons between traditional polymer glasses such as PS, PC, PET, and PMMA. Their ability to reach full cure is further indication the intermolecular interactions, which are known to contribute to deformation properties, are effectively constant. Shown in Figure 5.1 are LVDT-generated stress-strain curves for the DGEBF and DGEBA network isomers in compression. All networks were able to undergo ductile deformation up to 32.5% engineering (global) strain, beyond which lead to brittle failure of some samples. The

four networks show clear differences in secant modulus of elasticity (hereafter referred to as elastic modulus). At low strains (e.g. < 4%), 33F shows the greatest slope, 44F and 33A are nearly equal, and 44A exhibits the least. Table 5.1 lists the elastic moduli of the epoxy network series, calculated as the average slope from 0.5-1.0% strain. There is a clear trend of moduli with T_g , as well as average free volume hole size. In *Chapter IV* which explored thermal, architectural, and thermomechanical properties of the epoxy networks, we suggested a direct correlation between chain rigidity and T_g . In this case, the trend with elastic modulus and proposed network rigidity is reversed. Modulus is an intermolecular phenomenon; therefore this trend serves as further confirmation that chain rigidity disrupts packing, and thus serves as a secondary factor to modulus.

The difference in elastic moduli of DGEBF network isomers is decreased as compared to 33A and 44A networks. This dilution of the isomer effect in DGEBF networks may be attributed to the isomer mixture of epoxy prepolymers present in the commercially-supplied material. As mentioned in *Chapter IV*, as-supplied DGEBF contains a mixture of the ideal para-para isomer as well as some para-ortho isomer. In comparison, DGEBA is reported in much higher isomeric purity.¹³⁴ Additionally, DGEBA and DGEBF each contain trace amounts of chain extended dimer and trimer analogues, thus causing ranges in epoxide equivalent and molecular weights.

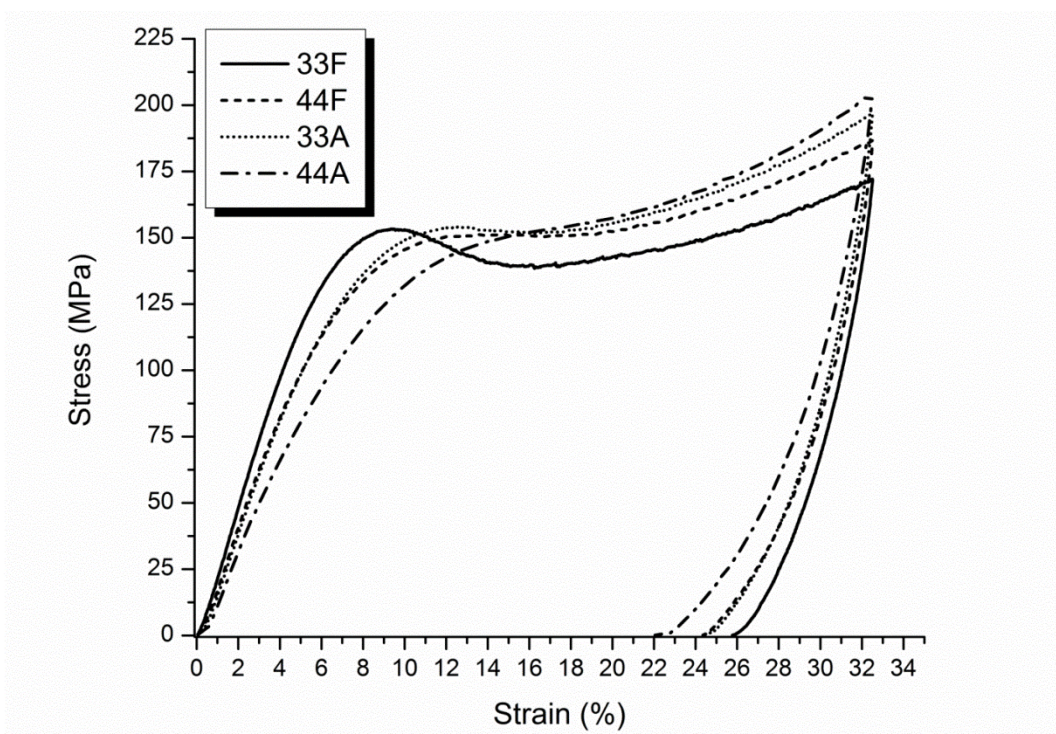


Figure 5.1 Stress-strain curves of epoxy network isomers in compression.

Table 5.1

Elastic properties as compared to thermal and architectural properties.

Network	DSC T_g (°C)	Average V_H at 23 °C (Å) ³	Elastic Modulus (MPa)	Yield Stress (MPa)	Yield Strain (%)
33F	158	67	2469 ± 31	150.0 ± 0.5	10.3 ± 0.23
44F	184	76	2178 ± 45	150.5 ± 1.1	13.9 ± 0.53
33A	176	77	2148 ± 104	151 ± 1.5	12.9 ± 0.52
44A	227	82	1611 ± 97	-	14.6 ± 0.34

Additional differences in compression behavior are clearly exhibited in Figure 5.1. In comparison to the para-substituted networks, the meta-substituted networks display measurable stress-drops near the traditional yield point. A stress-drop is typically associated with yielding behavior, wherein an energy barrier is overcome for the onset of viscoplastic flow, and less energy is required for deformation to proceed in this regime.

As deformation continues beyond this regime, the network undergoes strain-hardening, which necessitates additional energy input. This transition in deformation regimes is clearly exhibited by 33F, which shows a significant stress-drop near 9% strain, a broad stress-strain “valley,” and finally significant strain-hardening. On the contrary, the more rigid 44F network approaches a plateau in the stress-strain curve before the onset of strain-hardening. This suggests the networks advance through the yielding process via different deformation mechanisms. Albeit a small difference, the degree of strain-hardening (slope of the stress-strain curve at high strains) is greater for 44F, further evidencing deformation advancement via different mechanisms or distribution of mechanisms. A similar relationship is observed in DGEBA network isomers, where 44A shows the absence of a stress-drop and an early onset of strain-hardening behavior. Conversely, 33A exhibits a stress-drop near 12%, an abbreviated stress-strain valley, and finally strain-hardening. In a similar way to DGEBA network isomers, 44A displays strain-hardening to a greater extent than does 33A.

The maximum global strain attainable for all networks without fracture was 32.5%. Interestingly 44A, the network with the lowest modulus and highest yield strain – two parameters often associated with “toughness” – was the first to undergo fracture, which occurred at global strains near 33-34%. Conversely, 33F, 44F, and 33A could be strained to 35% consistently without fracture. This led us to hypothesize the distribution of deformation mechanisms of the epoxy network series varied significantly as a function of network rigidity. Differences in strain development between network isomers has been a focus of our research group in previous works.^{69,130} Specifically of interest has been the accurate identification of the yielding process of epoxy network glasses from the stress-

strain relationship, as this is a necessary parameter for theoretical failure models.

Through network rigidity variation, the stress-strain relationships and apparent yield behaviors change significantly.

5.2.1.2 Role of Chain Rigidity on Yield Stress and Strain

Glassy amorphous polymer networks undergo ductile deformation in compression significantly beyond yield imparting large magnitudes of plastic strain. As deformation proceeds, the energy storage and dissipation mechanisms shift depending on the mechanisms available at the testing temperature and rate. At low strain values in compression, the polymer deforms via elastic and anelastic strain storage mechanisms and can be completely recovered (with sufficient time) at the deformation temperature. At increasingly high strains, however, residual strains become irrecoverable at the deformation temperature and require significant time (or elevated temperature) to achieve recovery. This transition of deformation mechanisms is typically considered to occur at the yield point, though interpretation of molecular level events from a stress-strain relationship is complicated.

Defined by the traditional local maximum in the stress-strain relationship, the yield point can be determined from Figure 5.1, with the associated stress and strain values listed in Table 5.1. As discussed in *Chapter I*, this definition of yield is somewhat problematic in and of itself. 33F shows a clear local stress maximum followed by strain softening, while 44F and 33A near a plateau. The yield stress of 44A is missing from Table 5.1 due to the complexity of the stress-strain curve, which exhibits strain-hardening behavior in lieu of a stress-drop or plateau. This makes the yield point, by traditional definition, especially difficult to extract from this plot. Alternative methods for yield

determination are not trustworthy in this case. The 0.2% offset method, for example, gives a yield stress of 91 MPa and a corresponding yield strain of 5.4%, both values far lower than expected. This was verified through loading-unloading cycles, where strains were completely recoverable well beyond this point. Due to the similar yield stresses of 33F, 44F, and 33A, the yield strain of 44A was taken as the strain associated with a stress value of 150.0 MPa.

Regardless of the challenge for yield identification in 44A, these stress-strain relationships show all epoxy networks possess very similar peak stress values prior to strain-hardening and thus plastic deformation. Comparable yield stresses is an important observation to make for the epoxy network series as it confirms their intermolecular interactions are quite similar.¹⁴³ As a glassy material undergoes yield, viscoplastic flow proceeds which alters the spatial arrangement of polymer chains. Within a network, this has been correlated to an increase in the size and density of free-volumes, attributed to the deviatoric stress causing distortion.¹⁴⁴ As volume is maintained throughout the deformation, it has been shown the yielding process does not significantly affect V_H , which is controlled by the internal hydrostatic pressure of the polymer.

The yield strain shows a reverse trend from elastic modulus, wherein the highest elastic modulus network, 33F, gives a peak stress value at the lowest strain. 44A, on the other hand, shows the lowest modulus, lack of strain-softening, and the greatest yield strain. As with thermal and network architectural properties, 44F and 33A show very similar yield strains. This data continues to support the proposition of their shared (or highly similar) network rigidity influencing all relevant network properties.

5.2.1.3 Relating Chain Rigidity to Elastic Recovery

Beyond yield and strain-hardening, Figure 5.1 shows an interesting relationship regarding recovered strain upon unloading. All networks were strained to 32.5% engineering strain at 1.27 mm/min and unloaded at the same rate. The strain recovered upon unloading is considered to be elastic and completely recoverable. This behavior will be studied further in coming sections, though the trend observed here is clear in that it aligns with the yield strains and is the opposite trend of the elastic moduli. Due to its rigid chain segments promoting increased short-range molecular relaxations, 44A deforms in such a way that it has the greatest yield strain. In the same manner, it shows increased recoverable (elastic) strains upon loading well beyond the yield point. This corroborates the thermal and thermomechanical behavior discussed in *Chapter IV*, wherein additional glassy state degrees of freedom contribute to the decreased thermodynamic fragility of 44A and increased its CTE and $\delta\alpha/\delta T$. We attributed the increased elastic strain to glassy state energy storage mechanisms that are prominent in more rigid, loosely packed networks. Demonstrated by decreased glassy state expansivity, degrees of freedom, and relaxation mechanisms, more tightly packed networks store less energy in a recoverable manner, causing a decrease in elastic strain upon load release.

While the stress-strain relationship suggests differences in yield-type behavior and recoverable energy storage mechanisms, more advanced analysis is needed to further probe the various deformation mechanisms. Recent efforts have attempted to aid yield identification through molecular dynamics simulations, relying on a strain recovery approach to identify yield.⁶⁷ Quantification of residual, or irrecoverable strains makes strain recovery experiments advantageous for the identification of yielding behavior. To

define yield as the mechanically-induced analogue to long range molecular flow (T_g), we must increase our understanding of the relevant deformation processes. Further analyses using elevated temperature strain recovery experiments will allow us to directly probe the role of chain rigidity in glassy state deformation processes.

5.2.2 Effect of Network Rigidity on Deformation Mechanisms

5.2.2.1 Observing Deformation Mechanisms by Calorimetry

While disagreement persists within the community regarding the assignment of molecular motions to mechanical processes, there is consensus with respect to glassy state deformation consisting of two separate energy barriers. Energy is stored or dissipated during a deformation event via combinations of molecular relaxations of various length scales corresponding to their activation energies. Boyce and coworkers suggested two distinct deformation processes, each occurring once its energy barrier has been overcome, first via a lower energy process and at greater stress levels a higher energy process.¹⁴⁵ The first, lower energy process relates to local chain segment rotations, or shear transformations, which proceed with a wide distribution in activation energies. This process was attributed to energy storage and supported by calorimetric studies which show a glassy state exotherm present over a broad temperature range in deformed amorphous polymers relating to enthalpically-driven recovery. At higher strains, they observed a second, post- T_g exotherm, which they attributed to related to a longer range, anisotropic process associated with chain alignment and thus entropically-driven recovery. These motions are activated when energy can no longer be stored through shorter range motions, and arise from longer range, cooperative motions, and conformational changes. In their study of glassy amorphous linear polymers, the authors

suggested the first process relates to initial yield and strain softening behavior, while the second process corresponds with chain alignment and strain-hardening of the glassy amorphous polymers.

We observed similar behavior in the series of glassy epoxy network isomers. Small 1:1 precision-turned cylinders were able to undergo significant deformation (up to 50% global strain without fracture) and were subsequently heated within the DSC cell without further modification to the specimens. This allowed us to detect the two distinct deformation processes proposed by Boyce. Shown in Figure 5.2 are thermograms of a 33F cylinder at various deformation levels. Curves have been vertically shifted for clarity, though the relative heat flow values (W/g) were not changed, allowing for comparison of endothermic and exothermic intensities.

At an engineering strain of 20%, an exothermic process occurs well within the glassy state, indicative of energy storage during deformation. The absence of a glassy state exothermic peak for the 10% curve suggests strain was elastically stored during the deformation event, or relaxed prior to the start of the experiment. The onset temperature remains constant near 40 °C as does the broad peak breadth, while the peak intensity increases with increasing strain. The constant onset temperature suggests additional strains were stored by this process but were relaxed prior to the start of the experiment. A certain amount of deformation proceeded via the low energy process that could not be recovered at the deformation temperature in the short timespan between deformation and the start of calorimetry experiments, and could only be recovered upon heating.

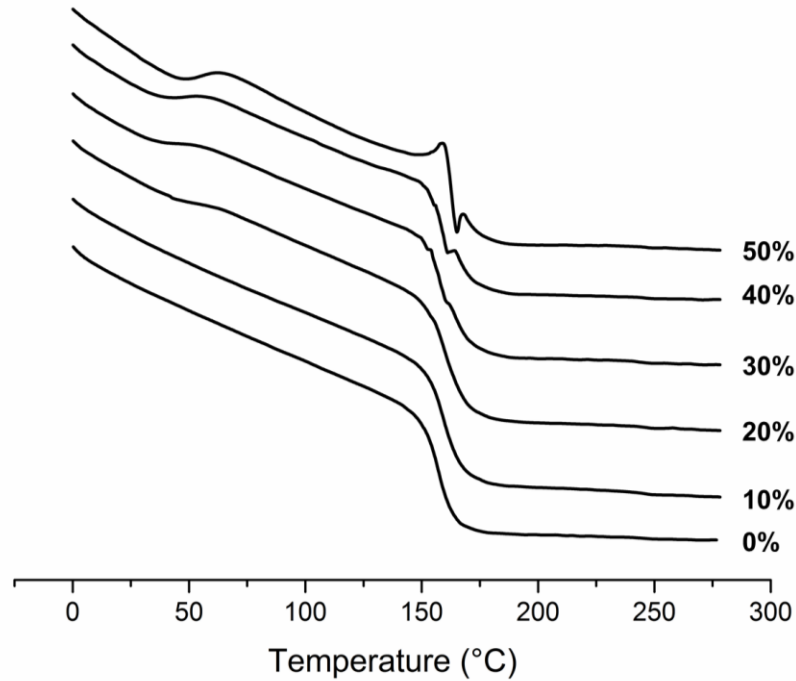


Figure 5.2 Vertically shifted DSC thermograms of deformed 33F cylinder.

Endotherm down.

At 30% engineering strain, a slight peak or undulation at the T_g endothermic step appears the intensity of which increases in the 40% and 50% curves. This endothermic peak, which occurs concurrently with the glass transition, represents the second, high energy barrier process described by Boyce. Energy which could not be stored during the deformation event (i.e. beyond the threshold of the low energy barrier process) is instead dissipated through a high energy process relating to conformational changes and chain segment alignment. The endothermic peak in the middle of the T_g step is representative of the regaining of entropy as aligned chain segments revert to their preferred disordered states.¹⁴⁵ Boyce et al. suggested this threshold occurs once strain softening during deformation has brought the glass to some “preferred maximum degree of disorder.” Beyond this point, further deformation imparts order in the form of chain alignment,

which is correlated with the strain-hardening features in the stress-strain relationship. At the highest engineering strain a short, intense exothermic peak occurs immediately prior to the T_g endotherm. This suggests an intense release of stored energy occurs upon sufficient mobility as the rubbery state is approached and chain segments have sufficient mobility.

The energy storage and dissipation behaviors of 44F and 33A in calorimetry experiments are fairly similar. Each 44F and 33A show exothermic peaks appearing at an engineering strain of 20%, indicating strain storage via the lower energy barrier process, as shown in Figures 5.3 and 5.4 (endotherm down). The onset of this peak falls at a similar temperature to 33F at ranging from 44 to 46 °C. The temperature delta from the deformation temperature suggests strain recovery continues to occur at the deformation temperature and is therefore missed by the calorimetry experiments. 33A shares more similar features to 33F than it does 44F, which is contrary to the findings of several other characterization techniques and requires further investigation. For example, the prominence of the exothermic feature at T_g is significant for 33A at an engineering strain of 30%, while the feature is highly suppressed in 44F. Indeed, the exothermic peak at T_g begins at 30% for 44F, grows in prominence at 40%, but is absent from the 50% curve. This will require replication, as the high energy deformation process is expected to increase in intensity at larger strains.

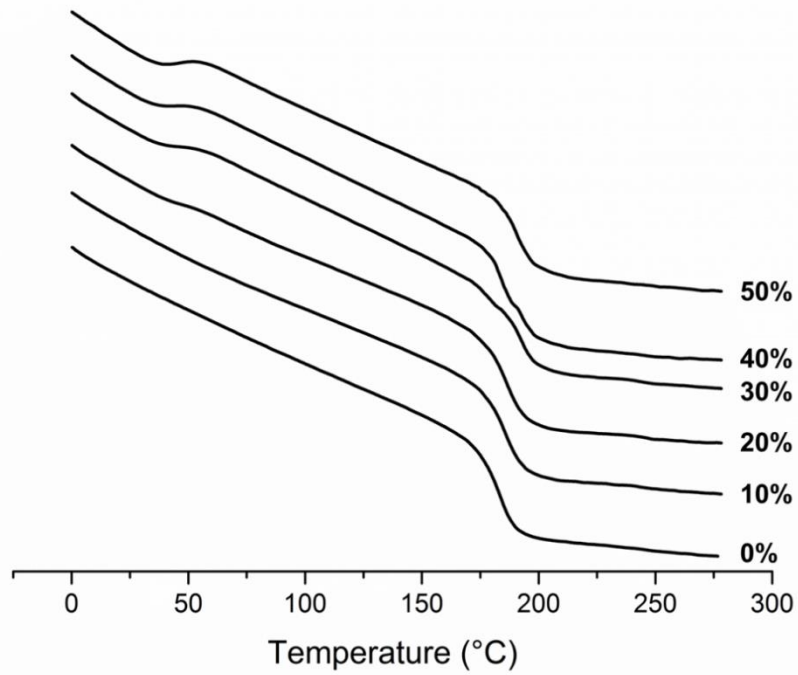


Figure 5.3 Vertically shifted DSC thermograms of deformed 44F cylinder.

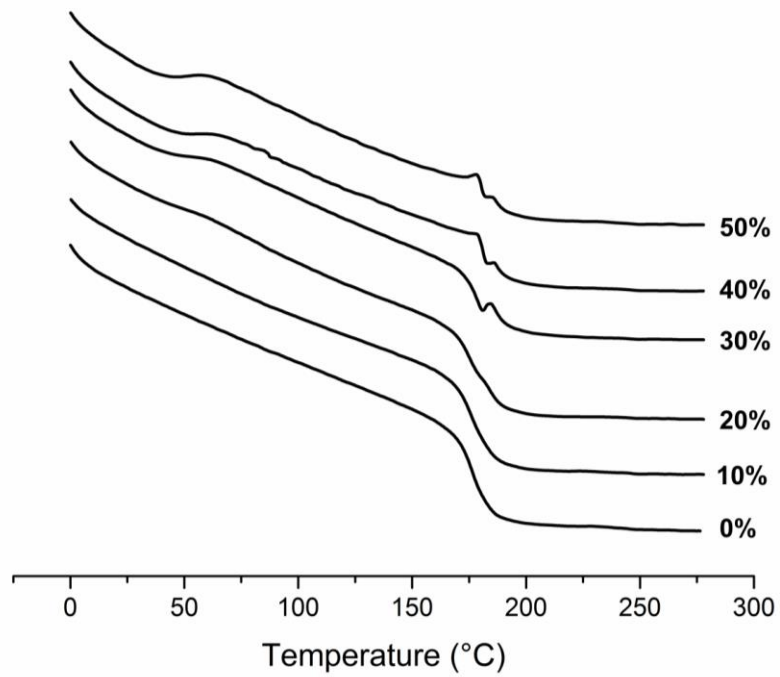


Figure 5.4 Vertically shifted DSC thermograms of deformed 33A cylinder.

In the case of 44A, Figure 5.5 shows the sub- T_g exothermic peak is not clearly present until a global strain of 30% and the peak intensities are less so than for 33F, 44F, and 33A curves. This finding is corroborated by the thermal and thermomechanical studies of *Chapter IV*, which indicated the rigid 44A network possesses additional glassy state degrees of freedom due to its rigid nature and inefficient chain packing. These relaxations allow for elastic storage of strains to a greater extent than 33F, 44F, and 33A, which are recoverable upon unloading (or recovered at the deformation temperature prior to the start of the calorimetry experiments). Additionally, all curves lack an endothermic feature at T_g indicative of the high energy barrier deformation mechanism. This suggests 44A is able to deform to greater strains via elastic and low energy barrier mechanisms throughout the strain range investigated as compared to 33F, 44F, and 33A.

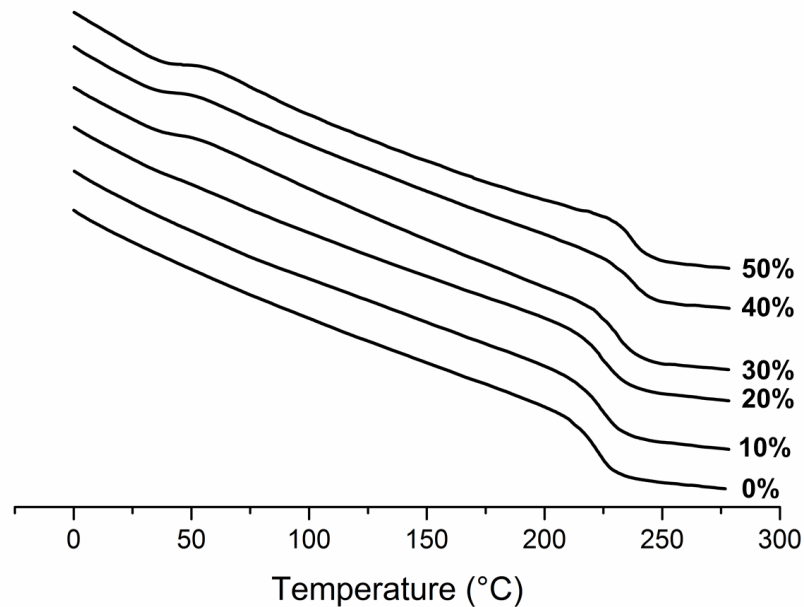


Figure 5.5 Vertically shifted DSC thermograms of deformed 44A cylinder.

Endotherm down.

Discussed in the previous section, the glassy epoxy network isomer series differ in recovery of elastic strains, evidenced by the stress-strain relationships during unloading. As conducted, the calorimetry experiments fail to capture all relevant deformation mechanisms, in particular missing strains recovered upon unloading and room temperature recovery prior to analysis. To better understand the distribution of deformation mechanisms, direct observation and quantification of strain components is necessary.

Previous work by our research group has separated strains into elastic, anelastic, and plastic components.⁶⁹ In this, strains recoverable at temperatures $T < T_g$ (i.e. $T_g - 20$ °C) were regarded as anelastic, while strains recovered at $T \geq T_g$ were considered termed plastic; however, as shown by the calorimetry plots, the release of stored strains occurs over a broad temperature range up to T_g , suggesting a lower energy barrier process remains prominent right up to the onset of long-range molecular translation and detection of the higher energy barrier process. Further, the assignment of anelastic strains at the temperature limit of $T_g - 20$ °C is rather arbitrary, especially considering materials with variable T_g breadths. As shown via calorimetry and expansivity experiments in *Chapter IV*, the networks investigated here differ significantly in the breadth of their glass transition, attributed to their differences in thermodynamic fragility. This makes discernment of anelastic and plastic strains problematic. The goal of this research is to understand the distribution of deformation mechanisms relative to network rigidity, which have been systematically varied through chemically-similar epoxy prepolymers and isomeric amine curatives. Next, we will use strain recovery experiments to separate

strain components for each of the investigated epoxy networks to allow for direct comparisons of network rigidity.

5.2.3 Separating Deformation Mechanisms via Strain Recovery Experiments

An advantage of glassy polymer networks is their ability to undergo thermal rejuvenation following a deformation event. The epoxy networks studied here allowed for complete recovery upon heating to temperatures above T_g . Behavior during strain recovery, specifically recovery progress as a function of temperature, gives insight into the energy storage/dissipation mechanisms contributing to a deformation event. Shown in Figure 5.6 are strain recovery curves of 33A cylinders after various deformation states. Samples were strained to the denoted engineering strain (controlled by the test frame LVDT) and allowed to recover at room temperature for 1h prior to heating in the TMA. The reference length (L_0) was taken at the beginning of the heating cycle for facile comparison. The first noteworthy feature of the plot is all curves are parallel and increase in a linear manner above 175 °C, just above the T_g as determined by TMA. This suggests within the rubbery state, regardless of deformation history, the networks are fully recovered and share expansivity properties. While behavior above T_g is the same, the curves show very different features at lower temperatures, with strained samples undergoing significantly greater length changes compared to the unstrained sample. This is indicative of strain recovery proceeding within the glassy state via the low-temperature process described by Boyce and coworkers. Although tests began at 20 °C, samples do not undergo significant changes in length until 30-35 °C. In the case of strain recovery by TMA, samples were allowed to recover at room temperature for 1h. As observed in calorimetry experiments, glassy state recovery only continues upon heating to

temperatures above the deformation temperature (approximately 23 °C) due to recovery at room temperature having already occurred.

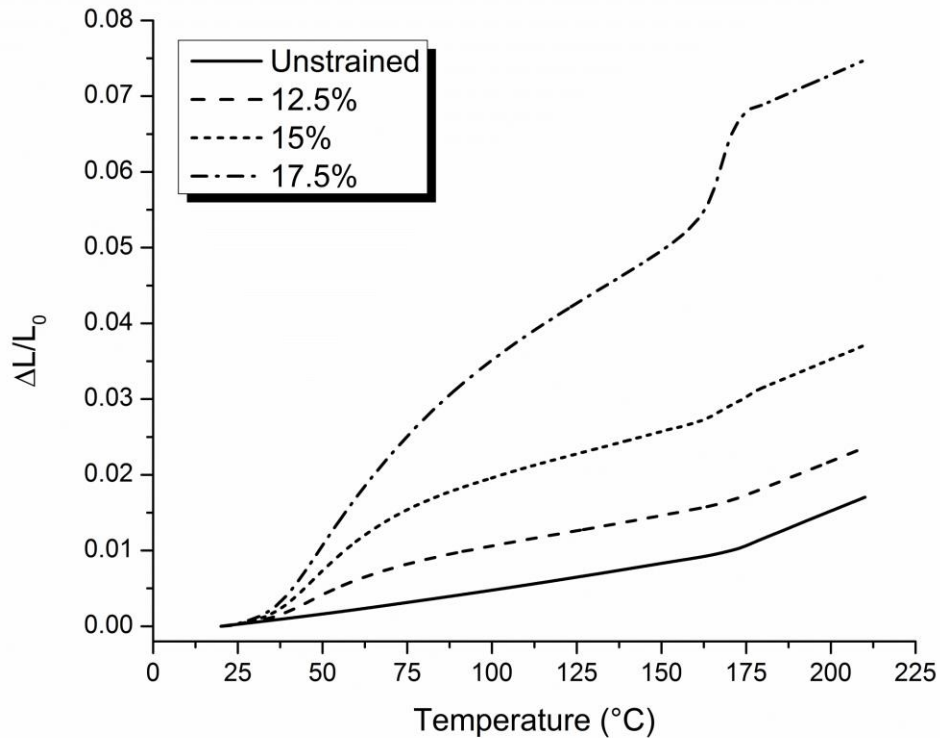


Figure 5.6 TMA strain recovery of 33A after deformation.

The 12.5, 15, and 17.5% curves show very different recovery features, which represents differences in deformation behavior. Progressing from the unstrained to the 17.5% sample, there is a clear increasing trend of change in sample length with respect to temperature, indicating a low temperature, glassy state recovery process (low temperature recovery, LTR). Samples strained to higher engineering strains have increased residual strains, and upon heating the LTR process proceeds at a rate proportional to the deformation. By approximately 100 °C, the 12.5% curve shows a similar slope of length change vs. temperature to the unstrained sample, suggesting full recovery of residual

strains. The 15 and 17.5% curves, on the other hand, display continued recovery throughout the glassy state. This supports the finding of Boyce et al. wherein the LTR process occurs over a broad temperature range as activation energy barriers continue to be overcome with heating to the glass transition.¹⁴⁵

In addition to an increase in slope, the 15% curve shows a small near T_g at 167 °C. This step is attributed to the entropy-driven, high temperature recovery (HTR) process described by Boyce, as sufficient mobility is realized at T_g , and chain disorder is regained.¹⁴⁵ At larger global strains, the size of this step is further increased as deformation proceeds through the HTR process, as shown by the 17.5% curve. The prominence of the LTR and HTR processes are better visualized by taking the derivative of length change with respect to temperature, shown in Figure 5.7. These were generated using the linear least squares method over 10 °C intervals.

The absence of a peak near T_g in the 12.5% curve in Figure 5.7 suggests deformation proceeded in the absence of the HTR process. From the previous section, the yield point of 33A (defined by a local stress maximum) occurs at 12.9%. This correlates well with strain recovery behavior, with the HTR process occurring between global strains of 12.5 and 15% as indicated by the increase in length change in Figure 5.6, and the appearance of a peak in the 15% derivative curve. Comparing peak intensities between 15 and 17.5% curves, the HTR process occurs to a significantly greater extent, though the LTR process does as well. This suggests that while a higher energy barrier process has begun to occur, the strain storage mechanisms related to the LTR process have not yet been saturated. This is contrary to deformation mechanisms proposed by Boyce, where it was suggested a higher energy barrier process would occur once the

polymer glass reached a maximum degree of disorder.¹⁴⁵ While the linear polymers in their study suggested a threshold value for the LTR process, the glassy epoxy network studied here appears to continue deforming via both processes simultaneously.

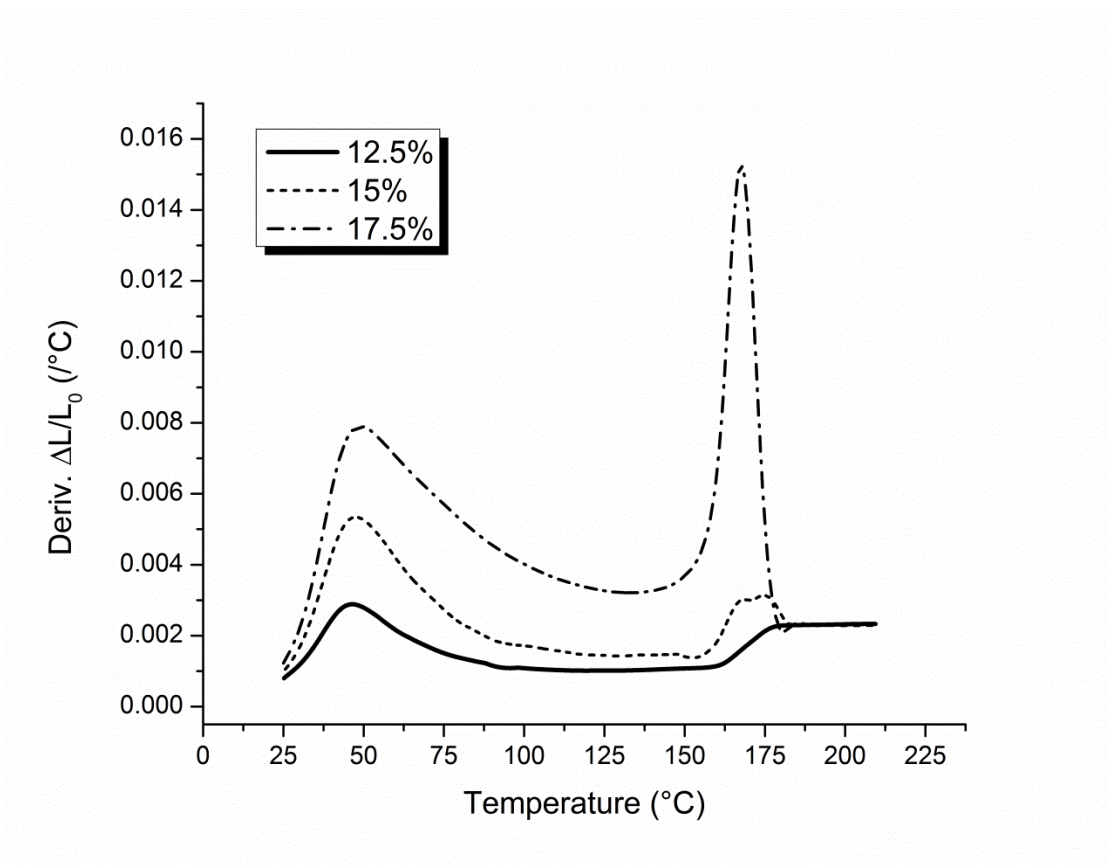


Figure 5.7 Derivative curves during thermal recovery of strained 33A cylinders

The rate at which strain recovery occurs upon heating can be particularly useful in the discernment of deformation behaviors of the epoxy network isomer series. Shown in Figure 5.8 are length change derivative curves for deformed epoxy networks upon heating from room temperature through T_g . As in Figure 5.7, there are two distinct peaks for each network, representing the LTR and HTR processes. In this case, all networks were deformed to the maximum tested strain of 32.5%, thus the HTR peak shows significant intensity. In comparisons of network isomers, 33F shows a significantly more

intense peak than 44F, and the same is true of 33A relative to 44A. This serves as evidence to para-substituted diamines imparting increased network rigidity, which suppresses the cooperative molecular motions associated with the HTR process. The intensities of the LTR peaks are significantly less, however, they extend over a broad temperature range. This is especially the case for the LTR peak of 44A which begins at 25 °C and extends to the onset of the HTR peak at 175 °C. Interestingly, the HTR peak breadth qualitatively compliments prior thermodynamic fragility considerations.

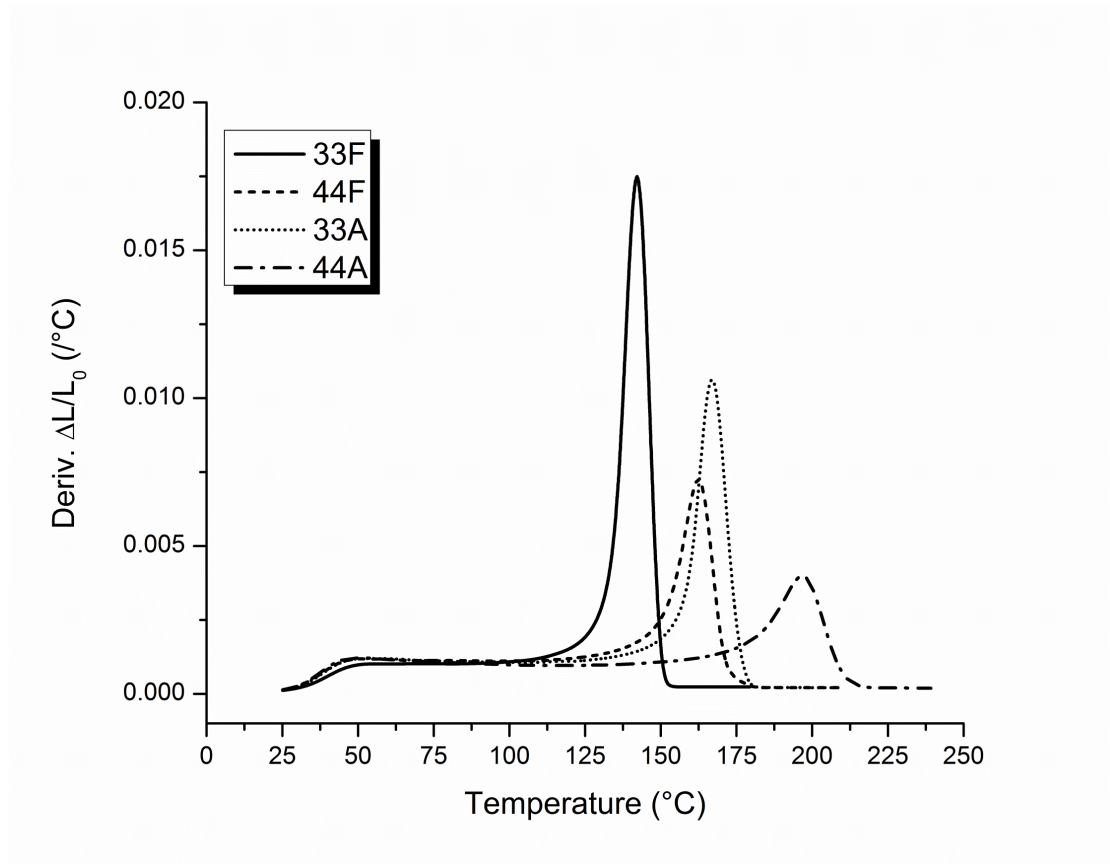


Figure 5.8 Length change derivatives for samples deformed to 32.5%.

To visualize the progression of deformation via the LTR and HTR processes, we consider the length change derivative curves as probability density functions, the integrations of which can be set equal to one. This allows us to calculate a cumulative

distribution function for each probability density function as a representation of recovery progress as a function of temperature. In this, the integral of the derivative curves for each network over the entire temperature range is set equal to one, to which a running integration can be normalized. This is represented by Equations 8 and 9 below:

$$1 = \int_a^b f(T) \delta T \quad (8)$$

$$F(T) = \begin{cases} 0, & t < a \\ \int_a^t f(T) \delta T, & a \leq t \leq b \end{cases} \quad (9)$$

where $F(T)$ is the recovery progress, a and b are the onset and offset temperatures of the LTR and HTR peaks, respectively, t is some temperature such that $a \leq t \leq b$, and $f(T)$ is the first derivative of length change with respect to temperature. Therefore when $F(T)$ is equal to one, complete recovery has been realized (note some values for $F(T)$ are greater than 1 due to length changes associated with thermal expansion, not strain recovery) This relationship is visualized in Figure 5.9.

The greater slope of 44F and 44A relative to their meta-substituted counterparts marks the promoted LTR process by a more rigid backbone. This process is not only extended over a broader temperature range – attributed to their increased T_{gs} – but their increased rigidity also accelerates the recovery progress to a greater extent to all temperatures in the glassy state. With comparable LTR and HTR process distributions, 44F and 33A exhibit very similar recovery progress attributed to their shared network rigidities and demonstrated by their nearly overlapping curves. Comparing the two meta-substituted networks, the more rigid 33A network shows accelerated glassy state recovery, further supporting the correlation of chain rigidity to a promoted LTR process. This difference in recovery behavior between the meta-substituted networks also serves

as an indication that simple glassy state motions (i.e. ring flips) do not hold significant roles in mechanical performance. The step size at T_g reflects network rigidity, where more rigid networks deform with less contribution of the HTR process. For direct comparison of the contributing deformation processes between the epoxy network series, we will next investigate their development at several strain intervals. This will allow us to understand how rigidity controls the ability of the networks to undergo shear transformations and conformational changes under identical deformation conditions.

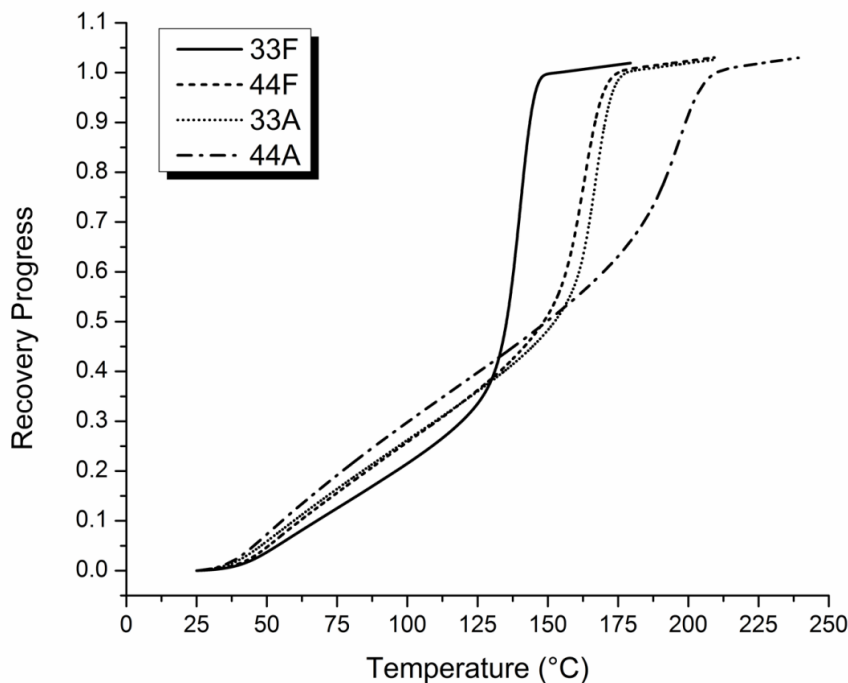


Figure 5.9 Recovery progress of network isomer series upon heating through T_g .

5.2.3.2 Deformation Components of Network Isomer Series

For comparison of the network isomer series, recovered strains were separated into elastic, LTR process, and HTR process components. To increase sensitivity, elastic strains were taken by caliper measurements immediately upon load release (as compared

to test frame LVDT measurements). Samples were then equilibrated at the deformation temperature for 1h before heating within the TMA. Room temperature recovery was combined with glassy state recovery during TMA experiments. The LTR and HTR processes were separated by the onset of the HTR peak in the length change derivative curves. All networks underwent complete strain recovery upon heating above T_g , and thus demonstrated shape memory behavior. In attempt to minimize experimental scatter, a single test cylinder of each network was re-used for as many iterations as possible – in some cases all trials – provided cylinders did not show edge chipping or other degradation to quality. Thermal stability of the epoxy networks was verified via thermogravimetric analysis (TGA) to ensure network stability within the necessary temperature range through iterative reheating cycles. Figure 5.10 shows all networks are thermally stable to above 300 °C, with degradation onset temperatures ranging from 323 to 338 °C. This confirmed the temperature limit of 240 °C for strain recovery studies did not impart significant sample degradation. This was further verified via TGA through repeated heat-cool-heat cycles to 250 °C, wherein all networks showed complete weight retention.

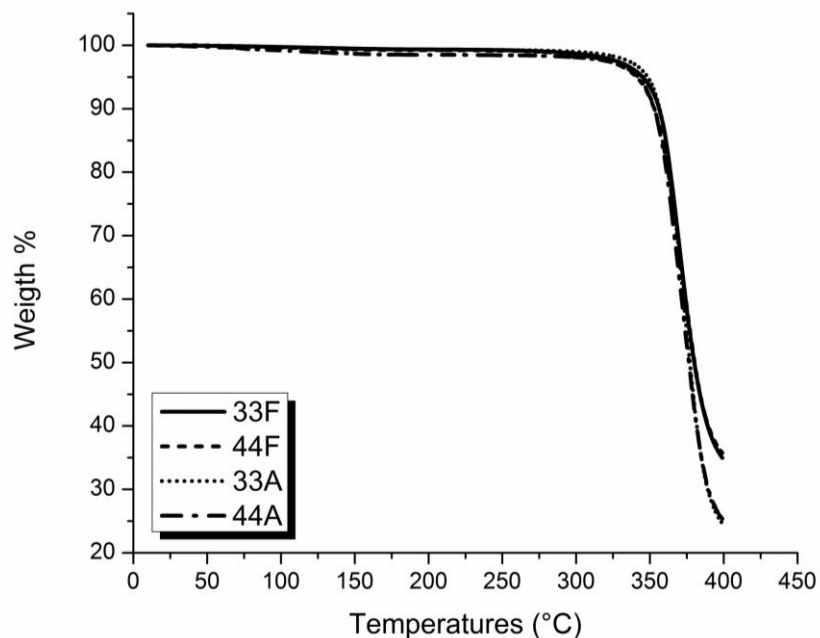


Figure 5.10 Weight % vs. temperature for network isomers.

The LTR and HTR processes are fundamentally different in their driving forces, size scale, and level of molecular cooperativity. The LTR process is an isotropic, enthalpically-driven energy storage process, and is proposed to relate to shear transformations or bands.¹⁴⁶ Stored energy is released once the network has sufficient energy to overcome the broad range of activation energy barriers, as evidenced by the broad glassy state recovery processes detected via calorimetry and thermomechanical experiments. The HTR process, on the other hand, is an anisotropic process which relates to chain alignment making its recovery entropically-driven. The epoxy networks studied here afford the ability to probe the role of chain rigidity in the distribution of these processes. Plotted in Figures 5.11 through 5.14 are the distributions of elastic, LTR, and HTR processes for each of the four epoxy networks overlaid with their respective stress-strain curves.

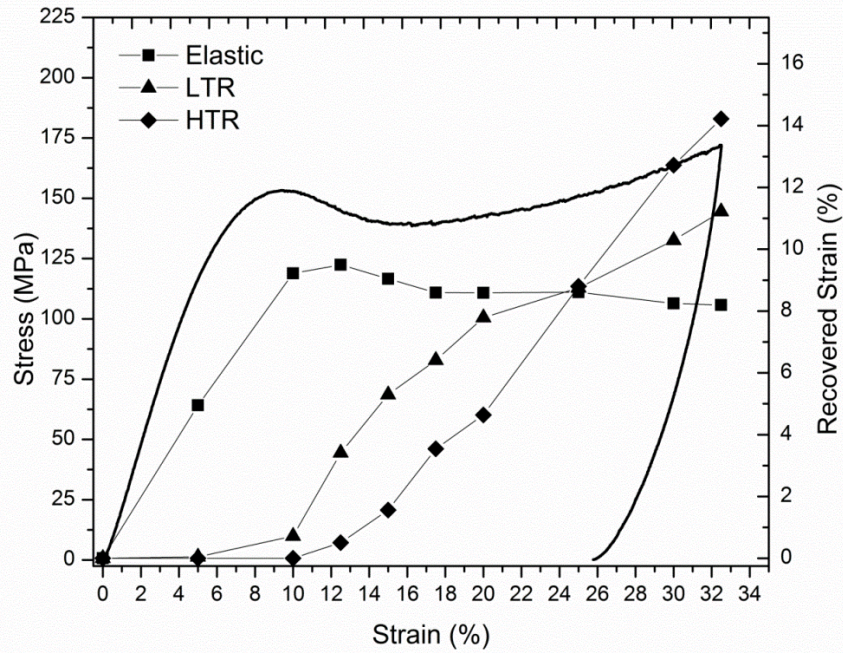


Figure 5.11 Strain components of 33F through progressing deformation.

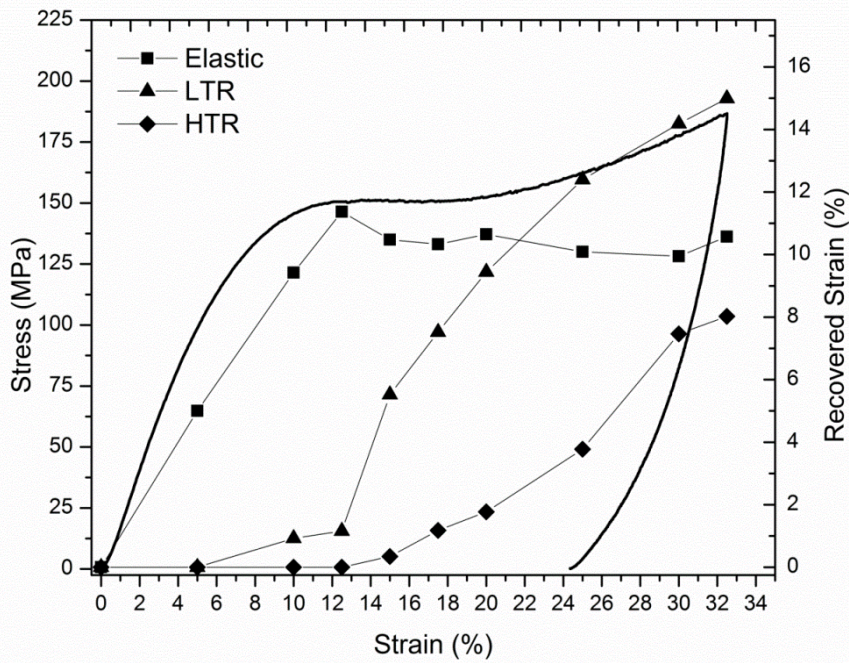


Figure 5.12 Strain components of 44F through progressing deformation.

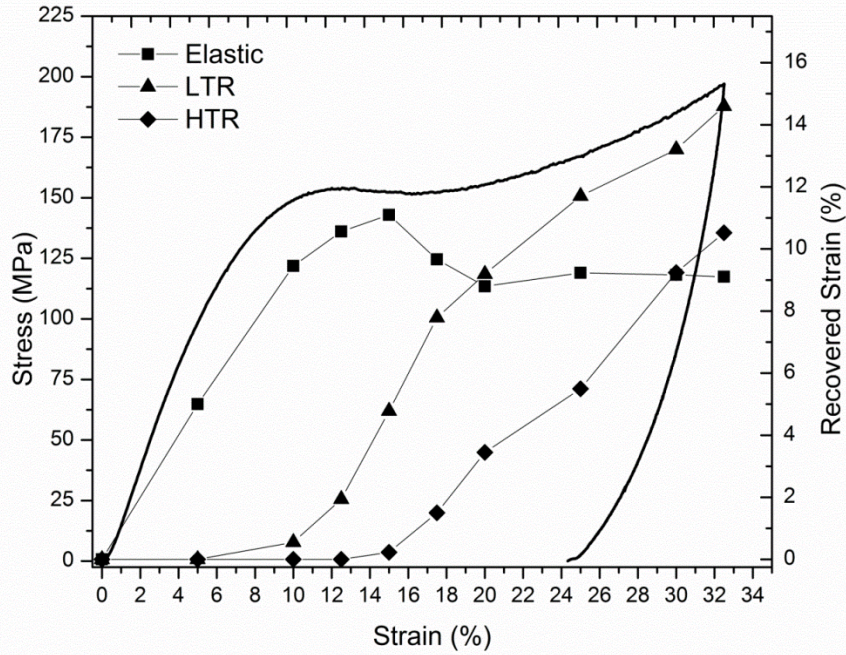


Figure 5.13 Strain components of 33A through progressing deformation.

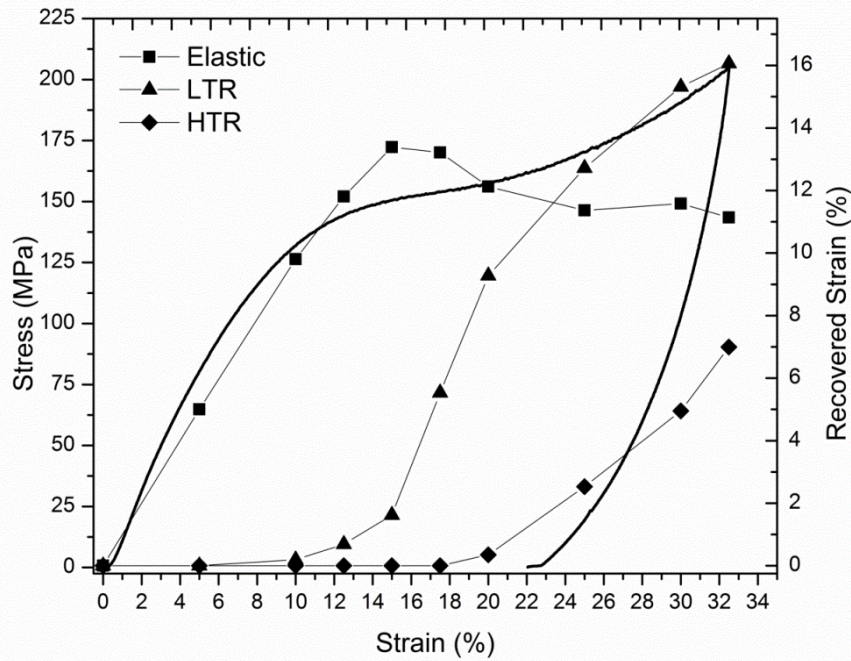


Figure 5.14 Strain components of 44A through progressing deformation.

In each plot, the elastic, LTR, and HTR strain components sum to the engineering strain depicted on the horizontal axis (plus a small contribution, typically < 1%, due to thermal expansion). Differences in network rigidity are directly represented by the distribution of elastic, LTR, and HTR processes. Specifically, chain rigidity is defined as the resistance to configurational changes. Therefore rigidity is best represented by the HTR process – strains recovered at T_g – the onset of which occurs at increasing engineering strains for increasing network rigidity from 33F to 44F and 33A to 44A.

In *Chapter IV*, we proposed 33F as the least rigid network of the series due to its low T_g and high efficiency of chain packing. This is supported by the distribution of its strain components, shown in Figure 5.11. At a global strain of 12.5%, the elastic strain curve shows a peak contribution of 9.5%, after which it decreases slightly to a plateau of about 8.5%. The LTR and HTR processes develop at slightly different global strains (10% and 12.5% respectively), but progress in a similar manner, indicated by the similar slopes of the LTR and HTR curves from 12.5% to 20%. As observed in the previous section, 33F also deforms simultaneously via the LTR and HTR processes, contrary to prior studies of linear polymer glasses. Beyond 20%, the LTR process contributes less and less to the deformation until the HTR process becomes the major contributing process at 25%. This crossover behavior is unique to 33F, as 44F, 33A, and 44A deform predominantly via the LTR process within the strain range of the study. Because the HTR process is understood to associate with a high energy barrier process relating to conformational changes and chain alignment, the tendency to undergo deformation predominantly via this process confirms 33F as the least rigid network.

As rigidity is increased from 33F to 44F via the fully extended para-substituted diamine, significant differences arise in the distribution of strain components, as seen in Figure 5.12, and similarly with 33A in Figure 5.13. In 44F, increased network rigidity causes a larger contribution of elastic strains, with a peak value of 11.4% and a plateau at 10-10.5% as rigid network segments store energy via reversible mechanisms to a greater extent. Increased network rigidity in 33A shows a similar increase in elastic strain contribution, with a peak value of 11.1%. While elastic contribution peaks at a global strain of 12.5% for 33F and 44F, the peak elastic contribution of 33A is shifted to 15%. Surprisingly, while increased rigidity from 33F to 33A increases elastic strain contributions, the two networks show very plateau values near 9%. This suggests the elastic strain threshold is largely controlled by conformational changes within the DDS unit, though additional studies are needed to confirm this. Relative to 33F the increased chain rigidities of 44F and 33A disrupt chain packing and allow deformation to proceed via local, non-cooperative mechanisms to greater energy levels before the onset of more cooperative motions. Further, this cooperative, high energy barrier process never exceeds the magnitude of the LTR process for either 44F or 33A, attributed to their increase rigidity relative to 33F. Figures 5.12 and 5.13 show the development of the LTR and HTR processes are quite similar for 44F and 33A networks, reflecting their similar rigidities.

Comparisons of 33F with 44F and 33A suggest increased chain rigidity is accompanied by increased elastic contributions to deformation and delayed occurrence of the HTR process. This trend holds true in the most rigid epoxy network of the series, 44A. Figure 5.14 shows the elastic strain curve of 44A shows a peak contribution at

13.4%, with a plateau at 11.5-12.0%, each feature measurably higher than the three less rigid networks. Through increased elastic contribution, which reaches its maximum at a global strain of 15%, delays the onset of the LTR process to 12.5% and the HTR process to 20%. The distribution of strain components differs greater in 44A in comparison to the less rigid networks. Upon straining more rigid chain segments resist configurational changes to higher deformations, requiring very large energy levels to bring about configurational changes. Thus chain rigidity necessitates deformation to proceed via local, short range molecular processes to a greater extent (both elastic and LTR processes) than the less rigid comparisons. It is interesting to note the development of the HTR process of 44A occurs at a global strain of 20%, which aligns well with an increase in strain-hardening behavior, as shown by the stress-strain relationship. This is not the case for the other networks, however, which undergo deformation via the HTR process prior to significant strain-hardening. We propose the unique stress-strain relationship of 44A (i.e. lack of strain-softening) is due to its rigid nature which limits deformation mechanisms to short range motions throughout the anelastic region and well into the plastic deformation region.

5.2.3.3 Network Architecture Considerations

In addition to chain rigidity, we hypothesize network architecture also holds a significant role in the distribution of elastic, LTR, and HTR processes. For instance, the maximum contribution of elastic processes within the network isomer series shows an opposite trend to elastic modulus. Loosely-packed network proceed to deform via short range, fully recoverable motions to a greater extent without significant cooperativity. With tightly packed chains, 33F exhibits the greatest stiffness due to the intermolecular

nature of the elastic modulus; however, the tightly packed and less rigid chains impart earlier and increased cooperative mechanisms of deformation. Under load, nearby chains are more likely to dissipate energy via cooperative motions due to proximity. Increased rigidity causes poor packing efficiency, which allows the local relaxation processes to proceed to higher deformation levels without imparting cooperative motions with adjacent chain segments. This causes 44F and 33A to deform elastically to greater global strains and also delays the onset of the cooperative HTR deformation process relative to 33F. With the greatest free volume, 44A shows the lowest elastic modulus but deforms to very high strains via short, non-cooperative mechanisms evidenced by the large contribution of the elastic and LTR components. Recalling behavior of the network isomer series in small strain analysis in *Chapter IV*, this trend was also observed in sub- T_g relaxation peaks. The γ relaxation is understood to arise from short length scale, non-cooperative motions. The rigid chain segments and poor packing of 44A led to a more prominent γ relaxation compared to 33A and 44F. The 33F network, with the greatest packing, showed the lowest intensity γ relaxation in the E'' and $\tan\delta$ curves. This leads us to conclude the cooperative nature of deformation mechanisms depends heavily on the complex contribution of chain rigidity and chain packing. In the epoxy network series investigated here, increased chain rigidity disrupts packing; however, further work is necessary in this to probe additional scenarios, such as rigid chain segments which are also able to pack efficiently.

5.2.3.4 Effect of Deformation Temperature

In polymers, deformation behavior is highly temperature and rate dependent, making temperature differential from T_g an important consideration. In *Chapter IV*, proximity to T_g was found to especially affect the CTE of more rigid networks. To probe the effect of temperature on the distribution of deformation mechanisms, 44A was tested at an elevated temperature such that the temperature difference from T_g was identical to that of 33A. The T_g of 33A by DSC for 33A is 177 °C, meaning a deformation at room temperature occurred at a temperature difference of approximately 154 °C. To create the same temperature differential for 44A, an environmental chamber was used to allow for a deformation temperature of 70 °C.

Figure 5.15 shows the derivative of length change upon reheating a 44A cylinder deformed to an engineering strain of 25% at 23 °C and 70 °C, as well as a 33A cylinder deformed at 23 °C for comparison. The shifted onset of the LTR peak to 60 °C for the cylinder deformed at 70 °C represents the role of the deformation temperature on the deformation processes available during loading and unloading. Increased thermal energy allows additional deformation modes to occur during loading, but also additional recovery upon load release thereby shifting the onset of LTR peak temperatures nearer the deformation temperature. With increased temperature, the intensities of the 44A LTR and HTR peaks increases significantly. Although peak intensities are increased, 44A deformed at elevated temperatures behaves very differently than 33A despite similar proximity of the deformation temperature to T_g . This further verifies the role of chain rigidity as the dominant factor in deformation mechanisms of chemically-similar glassy epoxy networks.

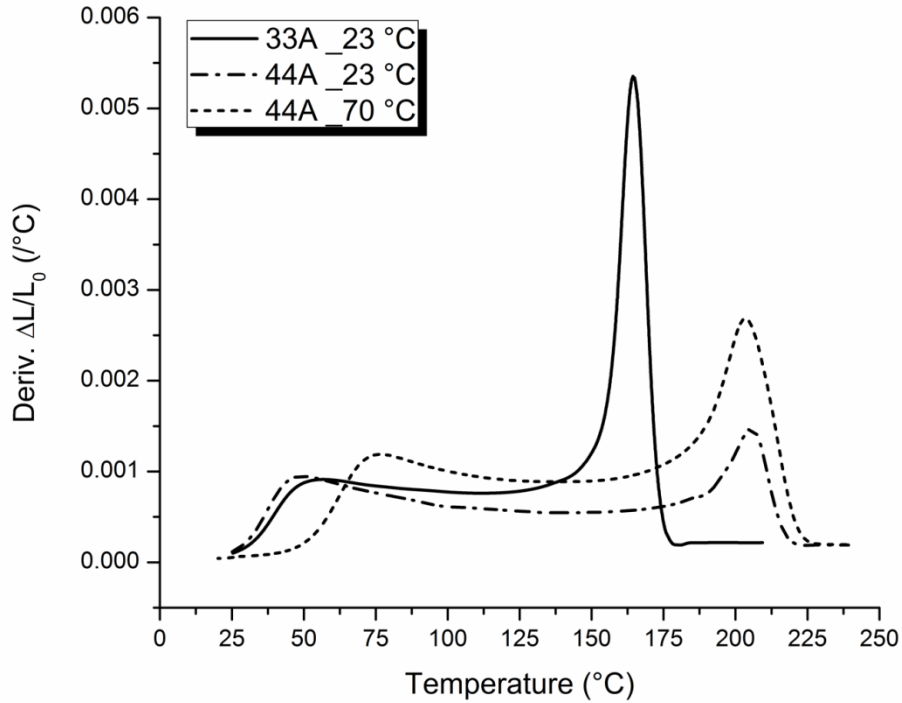


Figure 5.15 Recovery behavior of 44A tested at room and elevated temperatures.

LTR and HTR processes compared to standard 33A and 44A trials by length change derivative curves.

5.2.3.5 Correlation of Deformation Processes with Yield

As shown by the strain component plots in Figures 5.11 – 5.14, the occurrence of specific deformation processes cannot be unambiguously interpreted from the stress-strain relationship. The LTR process is shown to contribute significantly to the deformation of 33F, 44F, and 33A networks upon straining to an engineering strain of 10%. This aligns well with the yield strain of 33F but is significantly lower than the yield points of 44F and 33A. In the case of 44A, small contributions (0.2%) of the LTR process begin at 10% global strain, which corresponds with a shoulder of the stress strain curve, though the curve lacks a clear yield point which significantly convolutes its deformation behavior.

The detection of the HTR process (e.g. non-zero value) occurs after the defined yield strains of each epoxy network. Denoted on the stress-strain curves in Figure 5.16 are the engineering strains which coincide with the onset of the HTR process for each epoxy network. In this case, the HTR onset is taken as one strain interval (2.5%) prior to the detection of the HTR. The HTR process onset occurs at a similar stress value for all networks at approximately 150-152 MPa. This strongly supports the notion that yield does not necessarily correspond with cooperative long-range motions associated with the HTR process. Instead, this suggests yielding of these glassy epoxy networks is comprised mostly of local shear transformations relating to the LTR process reaching some critical magnitude. The HTR process develops in each network immediately beyond the yield point, however, suggesting yielding process relates to a critical threshold of shear transformations, requiring deformation to proceed through a new pathway. As previously mentioned, Boyce and coworkers proposed deformation proceeds via the high energy barrier process once the low energy barrier process reaches a threshold, representing a preferred maximum state of disorder. This work showed this threshold does not apply to these glassy epoxy networks wherein the HTR process develops in the absence of a plateau in the LTR curve; rather, the onset of the HTR process begins once a critical energy level has been applied by mechanical stress. The associated global strains at which the HTR process (yield-type deformation) occurs, however, are quite different between the network isomer series, reflecting their rigidity.

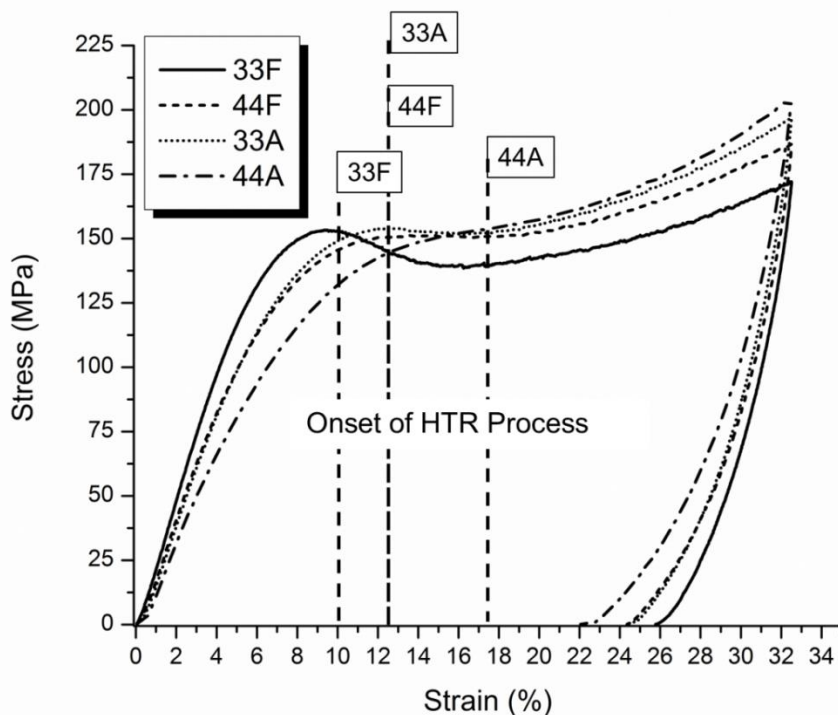


Figure 5.16 Onset of the HTR process relative to stress-strain relationships.

5.2.3.6 Network Deformation Scheme

Across the epoxy network isomer series, there are a number of similarities between the strain component plots. Each plot shows a peak in the elastic curve near the respective yield point, followed by a plateau indicating saturation or a threshold value of the elastic mechanism was reached. The LTR curve increases rapidly as the elastic curves begin to plateau, signifying the shift in primary deformation pathway. It is interesting that the elastic curve maximum precedes the initiation of the LTR processes in each case. This suggests the LTR process, which is associated with localized shear transformations, begins before the network has exhausted the elastic (reversible) deformation capability. Also the case for all networks, the HTR curve begins as the elastic curve declines from the local maximum and approaches the plateau. The HTR process develops in the absence of a plateau in the LTR curve, suggesting conformational changes and chain

alignment may occur in isolated regions of the material while other regions continue to deform via shear transformations.

The concurrence of increasing elastic and LTR processes, as well as the alignment of the HTR process onset with the elastic plateau, lead us to propose the following deformation scheme. Upon loading, the network deforms in a homogenous manner, with localized shear transformations occurring as the stress-strain relationship enters the nonlinear viscoelastic regime. This is visualized in Figure 5.17 as Deformation State I, comprised of small pockets of shear transformations homogeneously dispersed throughout the sample. These regions are sufficiently small such that upon unloading, they are completely relaxed. Upon further deformation, the shear transformations reach a critical size and can no longer fully relax upon unloading, requiring sufficient time at the deformation temperature or increased temperature for recovery. This time-dependent anelastic recovery is manifested as the LTR process. The yield point is observed in the stress-strain relationship once locally deformed regions reach a critical size or volume fraction, represented by Deformation State II. Post-yield, the development of sufficiently large deformed regions can no longer deform by the LTR process, necessitating the onset of the HTR process for continued deformation. This is shown by the increased size of deformation pockets in Deformation State III. As the stress-strain curve displays strain-hardening behavior (or increased slope showing accelerated strain-hardening), deformation proceeds primarily via the HTR process, visualized by the large fraction of large deformation pockets in Deformation State IV

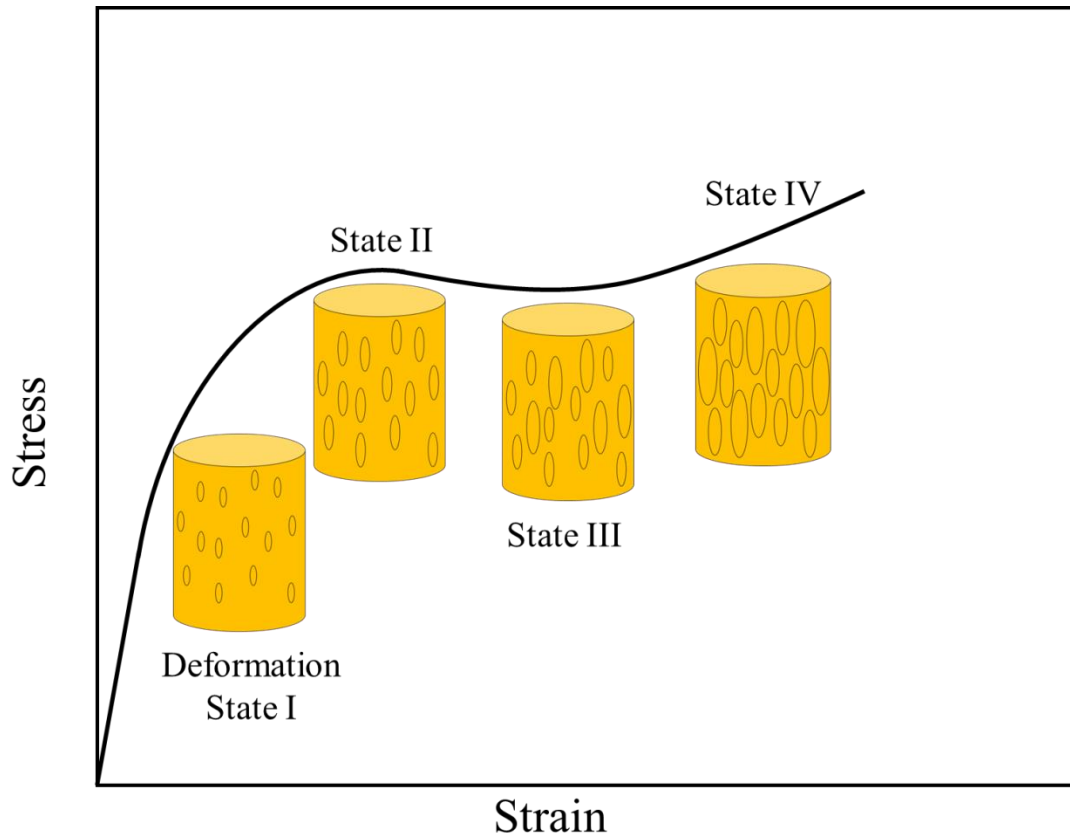


Figure 5.17 Proposed deformation scheme for deformation mechanism development.

To test the efficacy of the proposed model, we performed partial recovery experiments in attempt to alter the deformation pathway to some degree. A 44A cylinder was strained to a global strain of 25%, allowed to recovery for 1h at room temperature, and heated to the onset of the HTR process (175 °C). By quickly cooling the cylinder, we make the assumption that recovery included little-to-no strains relating to the HTR process, but instead all deformation due to the LTR process. The cylinder was then re-strained to the same global strain, allowed to recover for 1h, and heated to through the T_g . Our hypothesis was the residual strains would serve as initiation points for deformation to proceed, thereby altering the LTR and HTR process distribution. The derivative of the

sample's change in length upon heating is plotted in Figure 5.18, with comparison to a standard trial. The LTR peak is slightly suppressed in the restrained sample, while the HTR peak shows greater intensity and occurs at a lower temperature. This behavior supports our proposed model, wherein upon the HTR process is effectively “seeded” after the relaxation of shear transformations after initial straining. Upon deformation of the partially-recovered sample, regions which underwent the HTR process remain and further deform via this mechanism. The reemergence of the LTR peak in Figure 5.18 suggests the sample's “memory” was erased from certain regions which could again deform via the shear transformation mechanism.

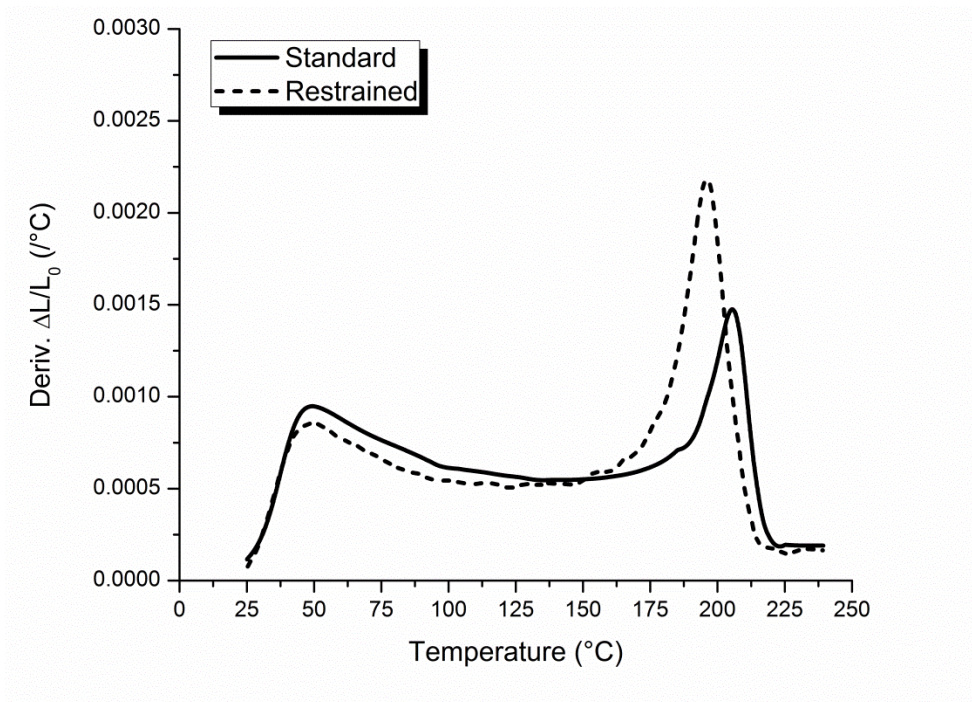


Figure 5.18 Length change derivatives of standard vs. restrained specimens.

Sample: 44A compression cylinder.

Differences in deformation mechanisms are further shown by integrating of the length change derivative curves as a probability density function, whereby setting the

integrations of curves in Figure 5.18 equal to one signifies full recovery in each case. This cumulative distribution function with respect to temperature is shown in Figure 5.19. The step at T_g , caused by the onset of the HTR process, is significantly larger for the restrained sample compared to the standard. In this case 34% of the recovery process occurs via the HTR mechanism compared to 17% for the standard specimen.

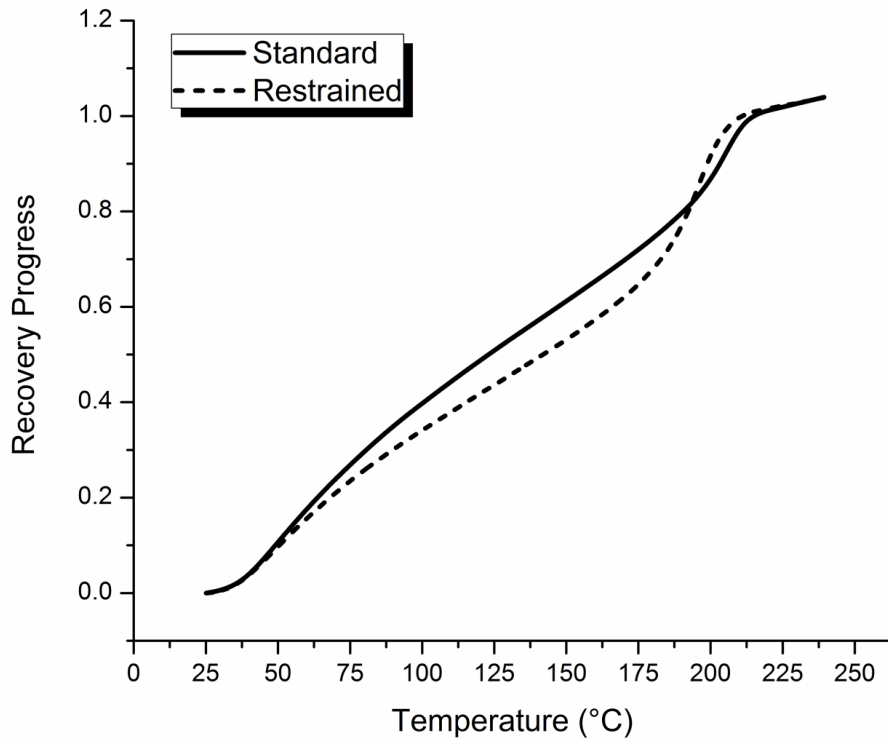


Figure 5.19 Recovery progress for restrained and standard 44A specimens.

As previously discussed and shown in 5.14, 44A deforms via the HTR process to relatively low contributions even at high engineering strains. This led us to hypothesize that decreased network rigidity may be more sensitive to the partial recovery and restraining procedures. Figure 5.20 shows the recovery progress of two 33A cylinders which were strained to 25% global strain, one per the standard procedure while the

second was restrained following partial recovery and restraining procedures. In this case, the deformed 33A cylinder was heated to 150 °C at 2 °C/min to achieve partial recovery and restrained to the same global strain. As with 44A, the restrained 33A network deforms via the HTR process to a greater extent as evidenced by the increased step size at T_g . The standard procedure for strain recovery shows onset of the step at T_g at a recovery progress of 0.58, meaning 42% of strain recovery proceeded via the HTR process. This is increased to 57% in the restrained specimen. This further shows deformation is promoted via the HTR process by the presence of previously deformed regions and serves as further validation for the proposed deformation scheme.

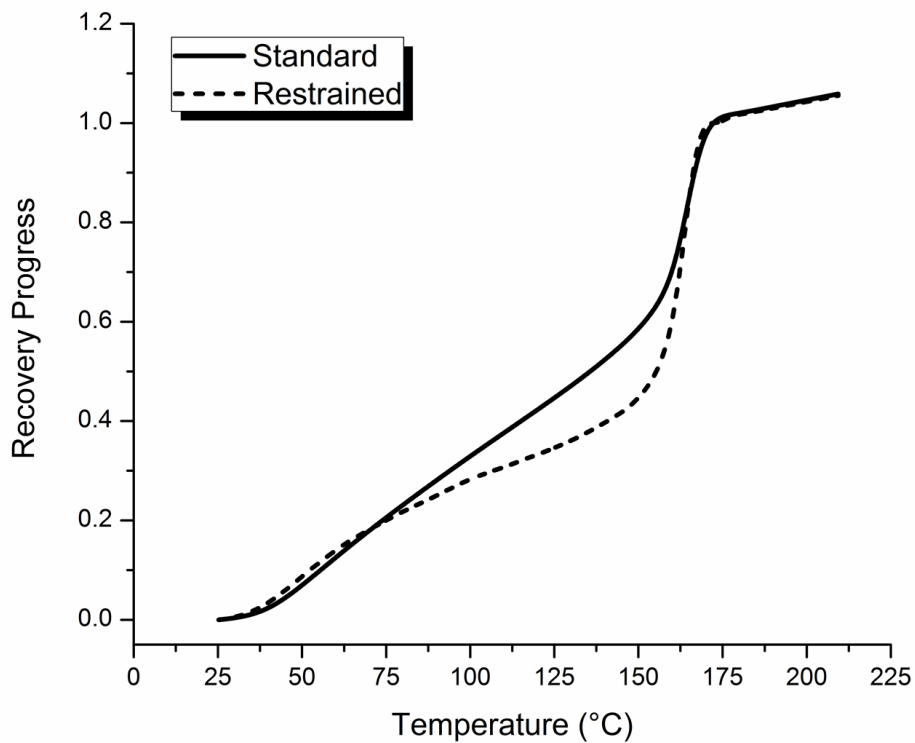


Figure 5.20 Recovery progress for restrained and standard 33A specimens.

5.2.3.7 Network Rigidity and Deformation Mechanism Limits

Throughout this study, the maximum testable global strain was 32.5%. This restriction arose specifically from 44A, which consistently underwent brittle failure at global strains of 33% to 34%. Recalling the distribution of strain components in Figure 5.14, at the maximum global strain of 32.5% the HTR process has reached a value of 7.0%. Brittle fracture upon further straining suggests the rigid nature of the 44A network limits the HTR process to some maximum value. This is a very interesting result that is contradictory to suggestions by Boyce et al.¹⁴⁵ They proposed the occurrence of the HTR process once the LTR process reached a threshold relating to a theoretical maximum state of disorder prior to deformation via the order-forming chain alignment process. Rather, our results show the LTR process continuing to develop alongside the HTR process in all four networks, never reaching a plateau within the available strain range. Further, the brittle fracture of 44A at low contributions of the HTR process suggests it had reached its maximum. This leads us to hypothesize a glassy polymer network is able to reach a deformation process threshold contingent on chain rigidity. More flexible networks will allow for a maximum state of disorder (LTR process) through ductile deformation, while more rigid networks will realize maximum deformation via conformational changes (HTR process) prior to brittle fracture. The former scenario would lead to a plateau in the LTR process, requiring the glass to deform solely via the HTR process beyond this point. We propose latter scenario was observed in 44A, where the rigid network deformed via conformational changes to threshold before brittle, catastrophic failure. Keeping all else equal (namely intermolecular interactions), a network of less rigidity than 33F is expected to reach a maximum LTR process contribution and exhibit a plateau; similarly,

a network of greater rigidity than 44A would undergo the HTR process to an even lesser extent prior to brittle fracture. Chain rigidity, therefore, dictates which deformation process realizes its maximum contribution under high loading, high energy situations.

5.2.4 Elevated Temperature Tensile Testing

To validate further the differences in network rigidities, the epoxy networks were tested in tension in the rubbery state. In the glassy state, chain packing holds a significant role in network properties such as elastic modulus, expansivity, and small strain mechanical relaxation. In the rubbery state, well above T_g , the networks can be considered equilibrium rubbers which pack very similarly, as evidenced by average hole size at elevated temperature.⁹³ Without significant differences in chain packing, deformation behavior in tension of these highly crosslinked networks in the rubbery state is driven by chain rigidity. We would expect, therefore, the more rigid, elongated chain segments to resist tensile deformation more so than a network which contains chain segments which can adopt additional configurations, represented by an increased modulus. Table 5.2 shows the secant tensile moduli for the glassy epoxy networks tested at $T_g + 50$ °C, as well as T_g s and room temperature compression moduli for comparison. In the rubbery state, the trend of modulus with chain rigidity is reversed, with the most rigid 44A network having the greatest modulus, nearly double that of 33F, with again similar values for 44F and 33A. A representative plot for each network is shown in Figure 5.21. It was observed that all networks fail in a brittle manner prior to showing yielding or strain-hardening behavior. This is consistent with failure mechanisms in the glassy state, due to their highly crosslinked nature.⁷⁰ Also listed in Table 5.2 are the

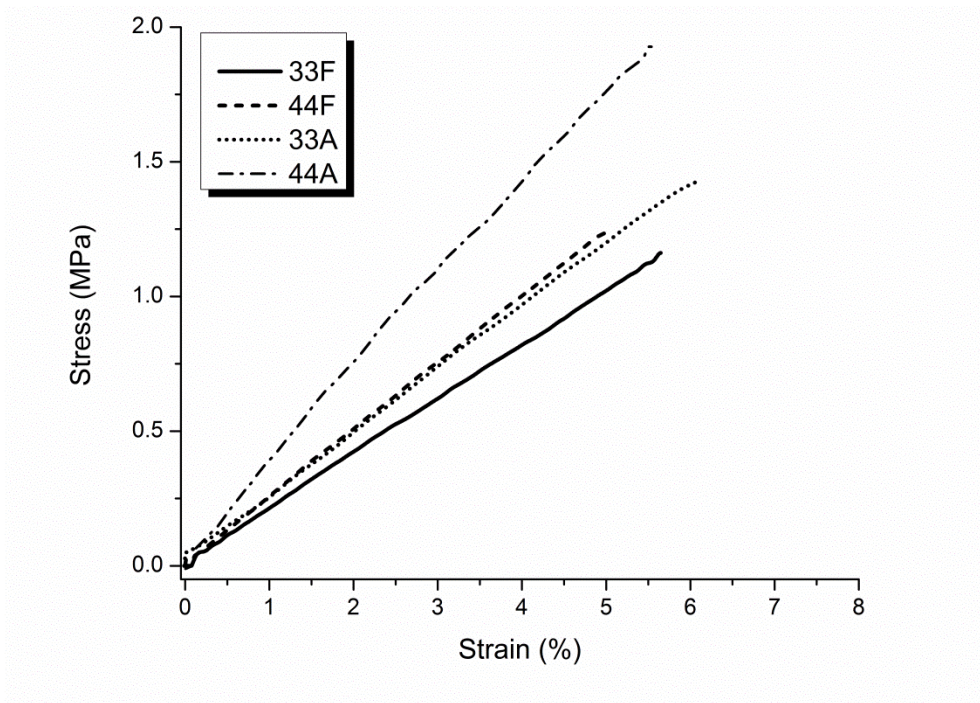


Figure 5.21 Elevated temperature tension curves at $T_g + 50\text{ }^\circ\text{C}$.

Table 5.2

Mechanical properties of network isomer series.

Network	Compressive Elastic Modulus (MPa)	Tensile Modulus at $T_g + 50\text{ }^\circ\text{C}$ (MPa)	Tensile Modulus at $270\text{ }^\circ\text{C}$ (MPa)
33F	2469	20.8 ± 0.60	21.4 ± 0.63
44F	2231	28.9 ± 0.75	29.2 ± 1.33
33A	2218	31.4 ± 1.46	30.5 ± 0.62
44A	1730	40.2 ± 1.56	40.2 ± 1.56

tensile moduli of all networks tested at $270\text{ }^\circ\text{C}$. The continued trend at equal temperatures validates moduli differences are attributed to chain rigidity rather than the contribution of temperature, which is known to increase the tensile modulus of traditional Gaussian-type rubbers.⁶⁵ We would expect the strain at break to also trend with network rigidity, with the most rigid networks unable to experience viscoplastic flow under tension.

Unfortunately, there was significant scatter in these experiments, which is likely due to

the fragile nature of the highly crosslinked rubbers, and additional testing with sufficient sample populations is needed.

5.3 Conclusions

Significant work, by our research group and others, has explored the isomerism effect in glassy amorphous epoxy networks. Prior work in this space has probed thermoplastic polymer glasses, which are susceptible to forming crystalline domains during deformation or possessing differing degrees of chain entanglements. Epoxy-amine networks offer a unique materials class which allows for completely amorphous, highly crosslinked networks which share strong similarities in chemical structure and connectivity. This work employed combinations of epoxy and amine components to form chemically-similar glassy networks which varied significantly in rigidity. We have shown that systematic variations in component rigidity – through either the epoxy or the amine – creates significant differences in overall network rigidity. Differences in polymer thermal, physical, and mechanical properties between structural isomers can, therefore, be attributed to rigidity differences rather than an “isomer effect.” This was made evident by the similar thermal, architectural, and thermomechanical properties of 44F and 33A discussed in *Chapter IV* and supported further here by mechanical testing and strain recovery experiments. Increases in network rigidity correspond with increased T_g and free volume, which in turn affects properties driven by chain packing and intermolecular interactions. Specifically, decreases in chain packing efficiency promote local molecular motions in the glassy state increasing CTE and the intensity of the short range sub- T_g mechanical relaxations but also decreases the glassy state elastic modulus. Conversely, the rubbery state modulus shares a positive correlation with network rigidity. Rigidity

similarly drives deformation mechanisms, where increased rigidity corresponds with greater elastic and LTR process contributions attributed to local chain relaxations and shear transformations. Networks comprised of less rigid components undergo more efficient chain packing, which increases intermolecular interactions and glassy state elastic modulus, but are more susceptible to conformational changes and cooperative motions upon heating or loading, as evidenced by decreases in T_g and early onset of plastic deformation. Finally, rigidity is not driven by a specific component, but rather an average parameter which defines nearly all related network properties. Therefore, networks which share a similar rigidity will exhibit highly similar behavior in thermal, architectural, thermomechanical, and mechanical properties.

CHAPTER VI CONCLUDING REMARKS AND FUTURE WORK

Polymer thermal, architectural, and mechanical properties are critical to all potential applications, and understanding how they interrelate due to chain rigidity and chain packing is crucial for the design of next-generation materials. The ability to tune properties such as T_g , thermal expansion, free volume, and elastic modulus via molecular design would bring a paradigm shift to the materials science community. While thermal and architectural properties of amorphous networks suggest several trends attributable to the rigidity of chain segments, these are indirect methods which probe behavior in the bulk. Many relationships established in linear polymers have been applied or presumed valid regarding the role of chain rigidity in polymer properties, though its role in crosslinked polymer networks has remained relatively unknown. Understanding the contribution of chain rigidity to relevant properties is complicated by inconsistent intermolecular interactions when comparing chemically-dissimilar polymer glasses, as is often the case. The family of polymer networks studied here offers a unique research space to probe the role of chain rigidity caused by subtle differences in molecular linkages without significant alterations in intermolecular interactions.

There has been significant research into polymer glasses in attempt to understand their structure-property relationships. Numerous studies have investigated the thermal and deformation behavior of thermoplastic polymer glasses such as PS, PC, PET, and PMMA; unfortunately, it is difficult to draw general conclusions from comparisons of chemically dissimilar thermoplastic polymer glasses, which can vary in their degree of chain entanglement or form crystalline domains during deformation. Prior research by our research group and others has explored the effect of structural isomerism on the

thermal, physical, and mechanical properties of polymer glasses. This allows for comparisons of chemically-similar materials, but it is difficult to attribute property differences to an isomer effect which cannot translate to other materials. The research presented in this dissertation exploited the common materials class of epoxy-amine networks which created a unique research space to systematically alter chain rigidity to investigate its role in structure-property relationships of amorphous polymer networks. We created a series of fully-cured, highly crosslinked glassy amorphous networks from a selection of aromatic, chemically-similar epoxy prepolymers and aromatic diamine isomers. The epoxy network series varied significantly in network rigidity, which has a profound influence on important properties. Properties and material behavior driven primarily by chain rigidity were: T_g , free volume, distribution of deformation mechanisms, yield behavior, and rubbery state tensile modulus. As a result of increased rigidity, chain packing efficiency is greatly affected, which in turn controls: elastic modulus, thermal expansion, and glassy state molecular relaxations. Further considerations involved polymer fragility, whereby increased chain rigidity corresponded with more “strong” behavior, causing broad glass transitions and gradual changes in network properties.

Future work is needed to further understand the interplay of intramolecular parameters and intermolecular interactions. To continue establishing themes, we have two proposed expansions based on the experimental procedures followed here. First, our findings suggested a limit in conformational changes in the most rigid network. To probe this limitation, a fully-curable network of increased aromatic content is needed. Benzoxazine chemistry offers a unique family of materials with modularity similar to that

of epoxy-amine networks. A Benzoxazine network based on bisphenol-A is chemically-similar to the DGEBA component studied here, and expected to be more rigid.

Deformation and strain recovery experiments may elucidate the existence of deformation process limitations, such as a highly extended, rigid network incapable of deforming via the conformational changes. A second approach involves the addition of polymer networks which vary only slightly in chemical identity, such as polar atoms in place of the methyl groups at the isopropylidene bridge in DGEBA. This substitution will alter intermolecular interactions through changes in hydrogen bonding, which are expected to alter network properties. It would be interesting to explore differences in mechanical properties, which are known highly driven by intermolecular interactions, especially through the yielding regime. Finally, correlation of chain rigidity and intermolecular interactions with dynamic fragility, in addition to thermodynamic fragility, would be a valuable contribution to the field.

APPENDIX A – Molecular Dynamics Simulation

A.1 Introduction

The materials science community is on the cusp of realizing truly complementary experimental and theoretical approaches to complex problems. As simulation efforts continue to proliferate, supporting these efforts with carefully-performed physical experimentation is crucial. Outlined in this appendix are collaborative efforts between The University of Southern Mississippi and The Boeing Company to achieve complimentary simulated and experimentally-measured material quantities. Specifically of interest were volumetric properties of highly crosslinked polymer networks. Described in *Chapter II*, 33F was used for this effort and compared to the multifunctional epoxy prepolymer TGDDM (shown in *Chapter IV*) which was also combined with 33DDS.

A.2 Experimental

A.2.1 Simulation

The computations from this work were performed on an in-house, 96-core, Linux cluster using software programs from Dassault Systèmes Biovia Corp. The molecular dynamics calculations were performed using Materials Studio 8.0, and a custom script was used for the creation of polymer networks at various stages of conversion. A second custom script allowed for the simulation of annealing from an elevated temperature to well below room temperature, during which the density of the polymer networks was tracked. Interatomic forces and associated energies were calculated using the Biovia's proprietary COMPASS II force field, while temperature was simulated using both Andersen and Parrinello thermostats. Crosslinking simulation was performed at a medium quality setting, with charge group-based interaction cutoffs. All simulations in

this work maintained 1:1 stoichiometry in correlation with experimental studies. Simulated networks of various levels of conversion were then annealed from 800 to 100 K at a fine quality setting, during which the density was measured in increments of 20 K. Density values were used for calculation of chemical shrinkage as well as glassy state CTE.

A.2.2 High Pressure Mercury Dilatometry

High pressure dilatometry experiments, commonly referred to as pressure-volume-temperature (PVT), were conducted using a GNOMIX high pressure mercury dilatometer. In this method, one variable is treated as the response, while a second is varied, and the third is kept constant. In this work, the specific volume of uncured epoxy-amine mixtures were monitored while temperature was varied and pressure was kept constant. Densities of uncured systems which were amorphous glasses at room temperature were calculated using the aforementioned method, while liquid mixture densities were measured using standard weight per gallon cups and converted to g/cm^3 values. The uncured materials were heated at the instrument's maximum heating rate (approximately $5\text{ }^\circ\text{C/min}$) to $180\text{ }^\circ\text{C}$ and held for 3 h. Chemical shrinkage was taken as the change in specific volume from the beginning of the isothermal hold until the specific volume reached a constant plateau.

A.3 Results and Discussion

Through a collaborative effort between The Boeing Company and the Institute for Mathematics at the University of Minnesota, two custom scripts were written for the simulation of polymer network properties. Additional modifications to the scripts were made through continued collaboration with Cytec Engineering Materials. The scripts require users to first create a periodic simulation cell, called an amorphous cell within Materials Studio, which contains monomers at a desired ratio and loading such that the total number of atoms numbered approximately 4000. The first script takes the amorphous cell through a series of reaction steps to simulate the crosslinking reaction between the epoxy and amine components to a predetermined percent conversion, creating a polymer network. The second script calls a non-reactive, annealing process which cools the amorphous cell stepwise in user-determined temperature increments. Throughout the annealing process density of the amorphous cell is calculated. Density serves as a representation of the volumetric properties of the polymer networks, and correlates well with experimental results.

Crosslinking simulation was performed at a group-based medium quality setting. Charge groups are created by the force field based on the electronics of the molecules within the amorphous cell. A charge group is a small group of atoms close to one another that has a net charge of zero (or near zero). The creation of charge groups can be performed automatically by the software, or manually by the user. Materials Studio provides two different algorithms for automatically assigning charge groups. The first uses repeating units (or other hierarchy) within a molecule and checks the charge of each subunit. If the charge is neutral (or near neutral) the subunit is made into a charge group.

The second method, known as divide-and-conquer, divides a molecule in two pieces, each of neutral charge. This division continues in a repetitive manner, creating smaller and smaller groups of atoms of neutral charge until cannot proceed further. The remaining groups become the charge groups. In most cases, charge groups are identical to common chemical functional groups (e.g. carbonyl, methyl, carboxylate groups).

The potential charges exerted by charge group of atoms at a distance, R , from the center of the group can be obtained by making an expansion in terms of the inverse powers of R :

$$\Phi \frac{1}{4\pi\epsilon} \left\{ \frac{Q}{R} + \frac{\mu \cos \theta}{R^2} + \frac{\Theta(3 \cos 2\theta - 1)}{R^3} + \dots \right\}$$

where Q is the total charge, μ is the dipole moment, Θ is the quadrupole moment, and the θ terms describe the orientation of the charge group. If the charge group bears a neutral charge, the leading term of the expansion is proportional to μ/R^2 . Considering a second group of neutral charge, with its center at distance R from the first, the leading interaction term will be proportional to $\mu\mu'/R^3$, where μ' is the dipole moment of the second charge group. The R^3 dependence suggests charge group interactions decay more rapidly than charge-charge interactions. Thus for a given cutoff distance, the use of charge groups is expected to better represent Coulombic interactions than atom-based cutoff methods.¹⁴⁷

Beyond charge group assignment, the quality of the simulation is based on four parameters: cutoff distance, spline width, buffer width, and relative dielectric whose definitions are given in Table A.1. The combination of these determines energy summations of the amorphous cell, and the specific values that correspond to the quality settings are element specific and are taken from the pseudopotential files stored within

the software database. For example, the “Medium” quality summation sets the cutoff distance to 9.50 Å, the spline width to 1.00 Å, the buffer width to 0.50 Å, and the relative dielectric to 1.00.

Table A.1

Definition of force field parameters.

Parameter (units)	Definition
Cutoff Distance (Å)	Distance between charge groups for consideration of van der Waals and Coulombic non-bond forces
Spline Width (Å)	Distance at which non-bond forces are splined from their full value to zero
Buffer Width (Å)	Distance beyond cutoff at which non-bond interactions are zero
Relative Dielectric Constant (unitless)	Relates to the permittivity of free space (1.00 is standard)

Reaction mechanisms, such as the ring-opening of an epoxide by a primary or secondary amine, cannot be predicted by Materials Studio. To accommodate, reaction sites are labeled by the user and called within the script such that they form accurate linkages upon simulated reaction. In the case of the monomers simulated here, the epoxies are built with epoxide groups that have already been opened and are missing a methyl group, while the amines are built with two methyl groups bonded to each nitrogen atom (shown in Figure A.1). Prior to reaction, each ring-opened epoxide contains an extra hydrogen atom in place of a methyl group, which is included on the amine. This modification also aids in the assignment neutral charge groups. The labeled reaction sites are methyl carbon atoms on the amine and the primary carbon of the ring-opened epoxide atoms on the epoxy, name R1 and R2 respectively. Upon reaction, the extra hydrogen atoms present on both the modified epoxy and amine molecules are eliminated to leave

the correct chemical bond. The script then calculates a reaction conversion percentage based on the initial number of reaction sites within the amorphous cell. Once the user-defined conversion has been reached (with a tolerance one reaction), the crosslinking script is terminated. If the conversion target is exceeded, extra bonds are deleted. All simulations in this work maintained 1:1 stoichiometry in correlation with experimental studies.

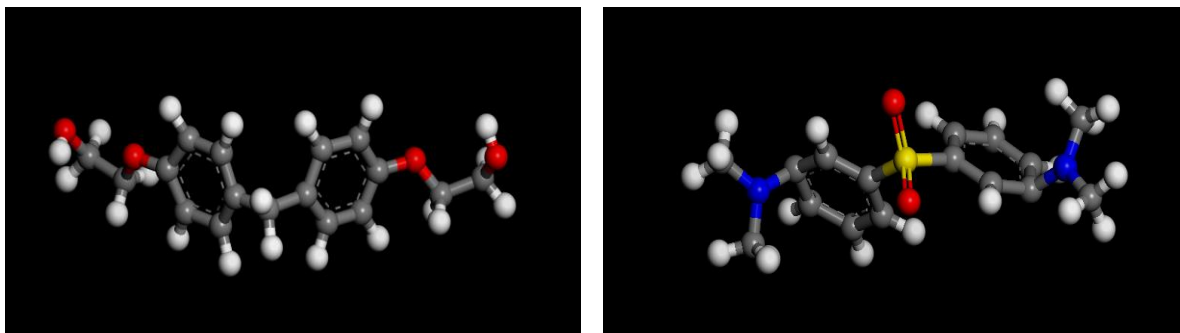


Figure A.1 DGEBF (left) and 33DDS (right) modified structures for simulation.

The crosslinking procedure iterates between nearest-neighbor reaction and short dynamics simulation steps. Distances between reactive sites R1 and R2 are computed, and all possible bonds within a cutoff distance are formed. The system, now with increased conversion of reactive sites, is integrated forward in time to relax the artificial stresses created. After relaxation, additional bonds can be formed if reactive pairs are found within the same cutoff. This process is repeated until no more bonds can be formed, incrementally progressing conversion. Once no more bonds can be formed at the initial cutoff distance, the distance is incrementally increased, and the steps are repeated. This process iterates until the cutoff reaches a user-defined maximum. In this work, the crosslinking steps were performed at a medium quality setting, reaction temperature of 800 K, with a minimum cutoff distance of 3.3 Å, increasing in 0.1 increments to a

maximum of 4.1 Å. The script calls two barostat protocols to control the amorphous cell pressure during the reaction steps. Dynamic steps up to 50% conversion alternate the Andersen and Parrinello barostats for 5 picoseconds each. This aids in prevention of unit cell skewing while the monomers are unconstrained and mobile. Above 50%, the Parrinello barostat is used exclusively, with 10 picoseconds relaxation steps after each bonding step to relax internal stresses.

Upon creation of an amorphous cell, the cell was checked for speared rings using an open source script available on the Accelrys online community forum. If molecules were arranged within the amorphous cell such that a molecule speared a second molecule in a non-physical manner, the script failed to complete and the amorphous cell was rejected. Similarly, if upon crosslinking a non-physical bond formed through a ring, the amorphous cell was rejected. Four accepted amorphous cells were created for the four simulated chemistries. These were taken to a final conversion from 90-95%. After each reactive step, a “snapshot” of the cell was output at increasing conversions. These output cells of various conversions served as the input amorphous cells for the annealing stage, with changes in density at a given temperature representing chemical shrinkage. During the annealing process, density of the polymer network increases significantly and is calculated every 20 K over the entire simulated temperature range. This allows for the densities of various networks to be compared at any single temperature, removing convolution of density change due to thermal expansion/contraction. Figure A.2 shows the density of six simulated networks at increasing conversions, ranging from 0 to 90%. Particularly at low conversions, a clear slope change or knee can be seen in the density-temperature curves, due to simulated annealing through the T_g of the polymer networks.

At high conversions, however, this knee becomes less prominent, complicating the calculation of simulated glass transition temperatures.¹⁴⁸ Density values of annealed 33F amorphous cells ranging from 0 to 93% were taken at room temperature, 300 K, to represent densification brought about by chemical shrinkage, shown in Figure A.3. Achieving 100% conversion was not possible due to the reactivity parameters outlined in the crosslinking script.

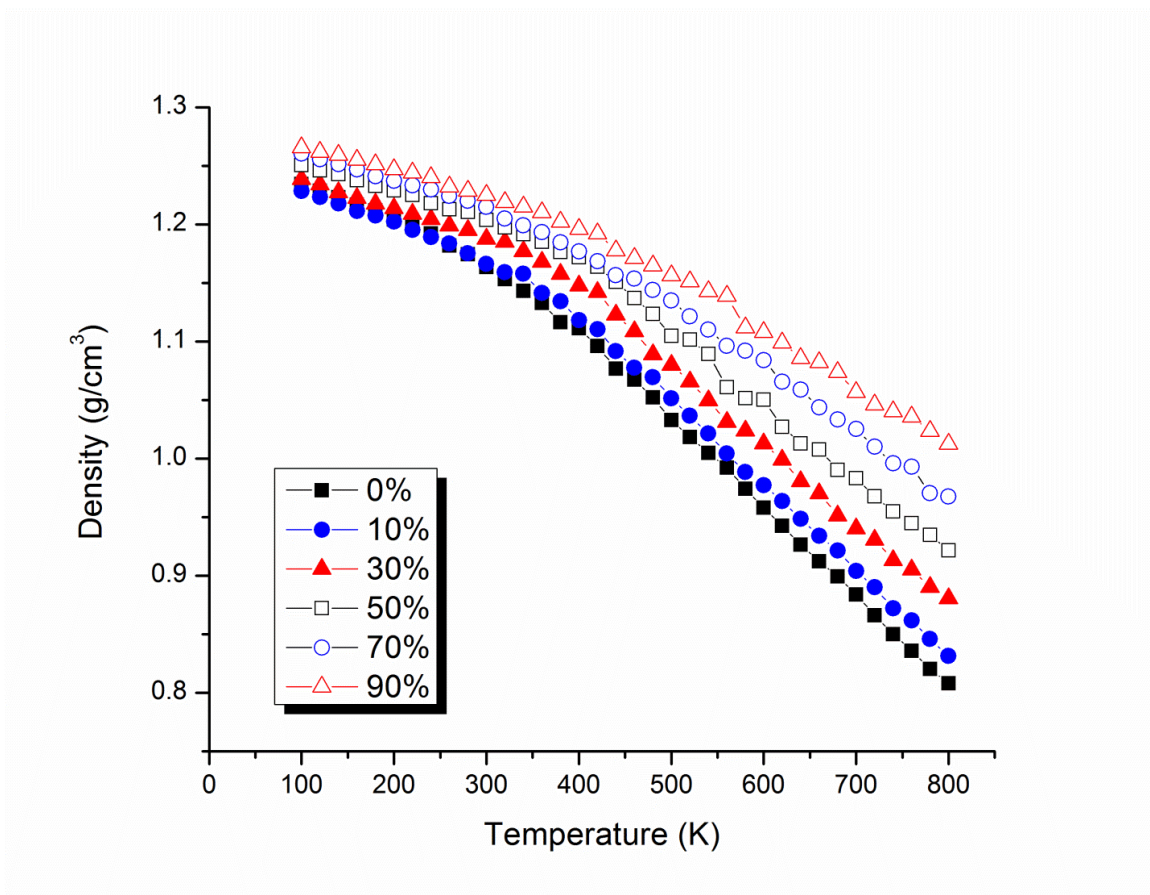


Figure A.2 Density upon annealing simulated 33F networks of increasing conversion.

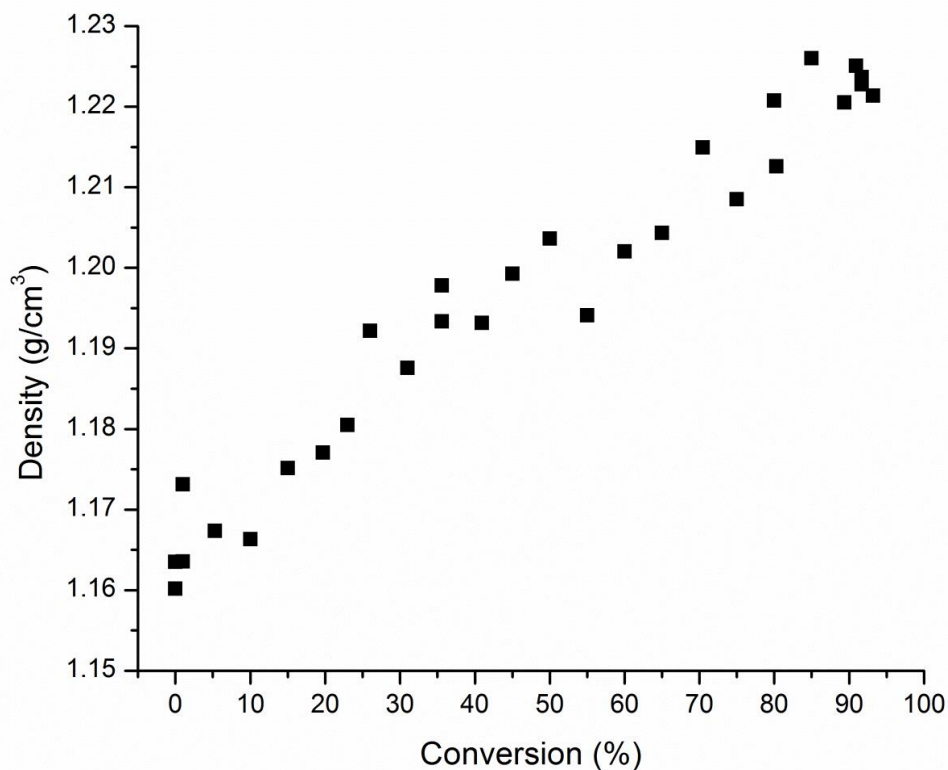


Figure A.3 Room temperature density (300 K) for 33F at various conversions.

Chemical shrinkage calculations are not often performed experimentally due to convolution of density (or volume) changes due to chemical shrinkages and thermal expansion or contraction. This is visualized in Figure 1.1 of *Chapter I*, which represents the volume changes a thermoset polymer will undergo during elevated temperature curing. Upon heating, changes in volume (or density) are solely caused by thermal expansion until significant chemical reaction occurs, shown from Point a to b. During an isotherm at the cure temperature, T_{cure} , volume changes are solely caused by chemical shrinkage (Point b to c). Upon cooling from T_{cure} , the polymer experiences volumetric contraction as chains pack and density increases (Point c to e). If T_{cure} is above the T_g of

the polymer, the rate of contraction with temperature will decrease as the polymer transitions from the rubbery (above T_g) to glassy state in cooling below T_g (Point c to d).

Experimentally, chemical shrinkage is commonly taken as volume change during an isotherm at the cure temperature to avoid convolution of thermal expansion and chemical shrinkage. One advantage of experiments in a simulated environment is the ability to account for this convolution. Simulated polymer networks of prescribed conversions can be taken through temperature ramps without causing any changes in cure state. Figure A.3 suggests a near linear relationship exists between polymer network density and conversion, which is in agreement with experimental results for epoxy resins;³⁸ however, there is significant scatter in the data. This scatter is due to convolution of densification due to chemical shrinkage with the annealing process. While the polymer networks are annealed from an artificially high simulated cure temperature of 800 K, their densities approach experimentally-measured densities as the temperature approaches room temperature; however for chemical shrinkage measurements densification due to cooling should not be included. To remedy this, we examine the simulated network densities at an experimentally-relevant cure temperature of 460 K (approximately 186 °C), shown in Figure A.4. Decreasing changes in density due to annealing removes much of the variation in the data, while the linear relationship between density and conversion is maintained.

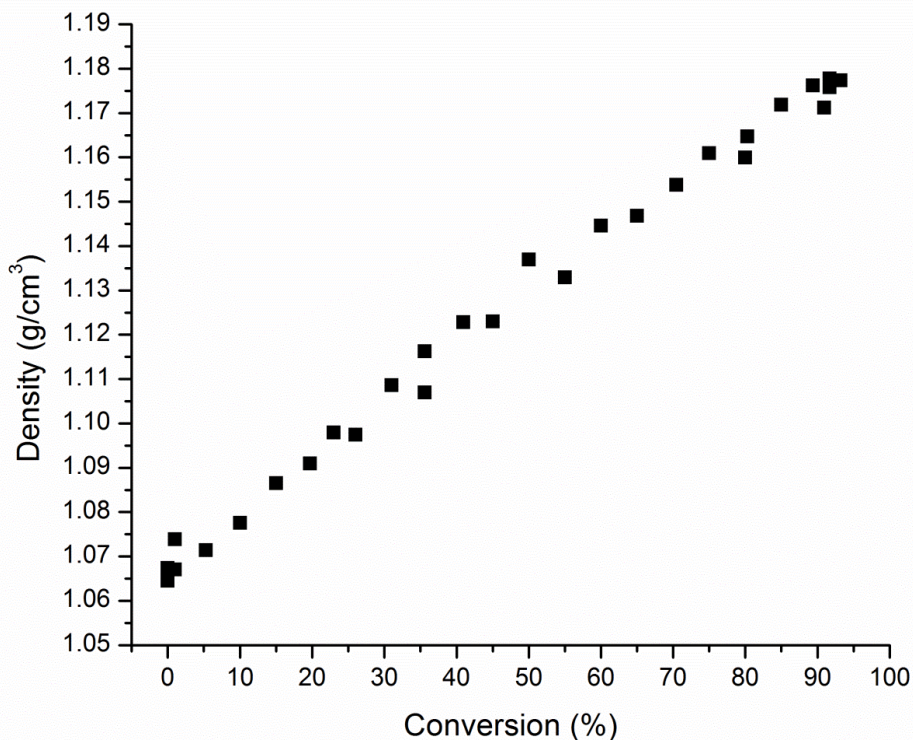


Figure A.4 Density at 460 K for 33F at various conversions.

Amorphous cell densities can be converted to chemical shrinkage measurements by simple calculations of density changes relative to the density of a 0% conversion network. Chemical shrinkage is brought about by the densification of a thermoset resin as prepolymers and curatives react forming covalent bonds and non-covalent bonded forces as polymerization progresses and molecular weight increases.^{10,11} It is, therefore, logical to hypothesize that amorphous polymer networks which exhibit increased room temperature density in the cured state would correlate with measurably increased chemical shrinkage. Because non-covalent bonds also contribute to the densification, studies seeking to compare differences in chemical shrinkage must employ chemically-similar polymer networks. The difunctional and multifunctional prepolymers diglycidyl

ether of bisphenol F (DGEBF) and tetraglydicyl-4,4'-diamino-diphenyl methane (TGDDM) are very chemically similar, while average epoxide functionality is significantly different at 2 and 3.6, respectively.¹⁴⁹ The aromatic amine isomer curatives of 3,3'-and 4,4'-diaminodiphenyl sulfone (33DDS and 44DDS) are chemically identical. The experimentally-measured room temperature densities of these four polymer networks are shown in Table A.2. It should be noted these samples were cured by the industrially-relevant cure cycle (IC) as described in Table 2.1 in *Chapter II*. By this cure cycle, final conversions and therefore room temperature densities are different than those reported in *Chapter IV*. Unfortunately, the densities did not show statistically significant differences between the four simulated networks. This can likely be attributed to the number of atoms simulated (approximately 4000) being too few for materials systems of nearly identical atomistic composition. Future works should explore coarse-graining of polymer chains to allow for simulation of larger systems. Coarse-grained models replace explicit atoms with grains, or pseudo-atoms, decreasing resolution at the atomic level and freeing up computation resources.

Table A.2

Polymer network densities measured by Archimedes' Principle.

Network	Room Temperature Density (g/cm ³)
33F	1.272 ± 0.003
44F	1.272 ± 0.003
33TGDDM	1.285 ± 0.002
44TGDDM	1.280 ± 0.001

Although simulated densities of DGEBF and TGDDM did not show significant differences, comparison of simulated and experimentally-measured properties was

continued for a select network and showed excellent correlation. Simulated chemical shrinkage of 33F as a function of conversion is plotted in Figure A.5. For these calculations, the density of a simulated amorphous cells at increasing conversions was taken at 460 K (186.85 °C) and normalized to the simulated density 0% conversion amorphous cell at that temperature. The temperature of 460 K was chosen due to its proximity to the experimentally-relevant cure temperature of 180 °C. At the highest conversions, simulated chemical shrinkage ranges from 9.34 to 9.46%. This is very similar to experimentally-measured chemical shrinkage of 10.0% by PVT, shown in Figure A.6.

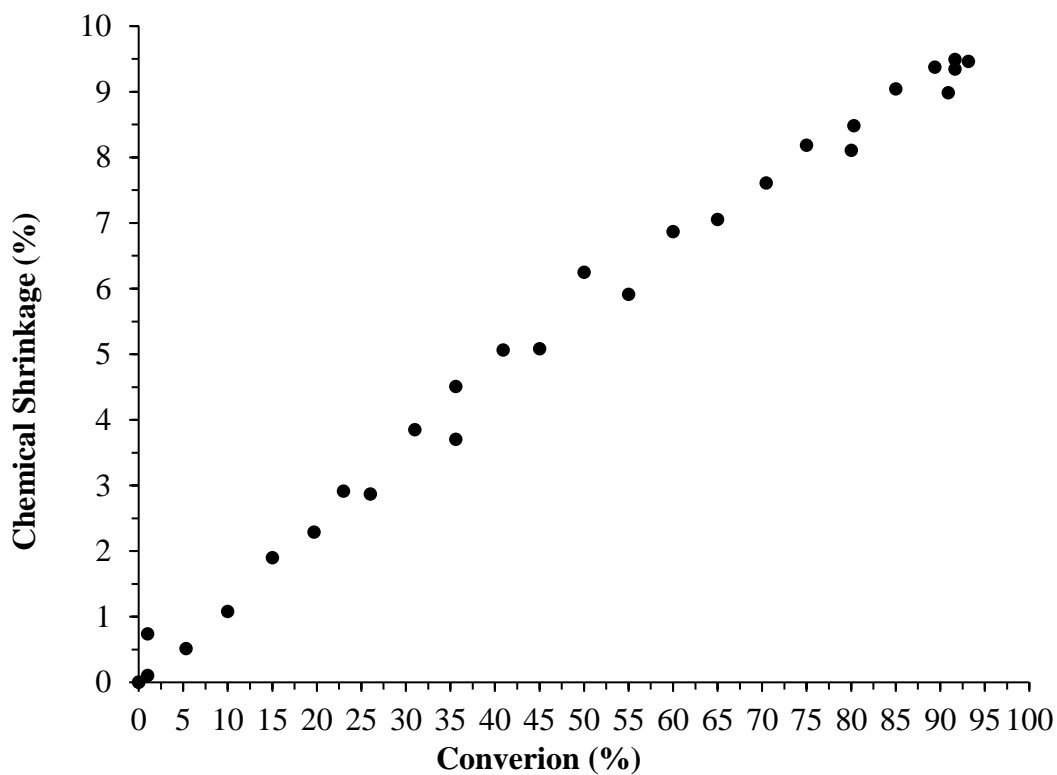


Figure A.5 Simulated chemical shrinkage of 33F.

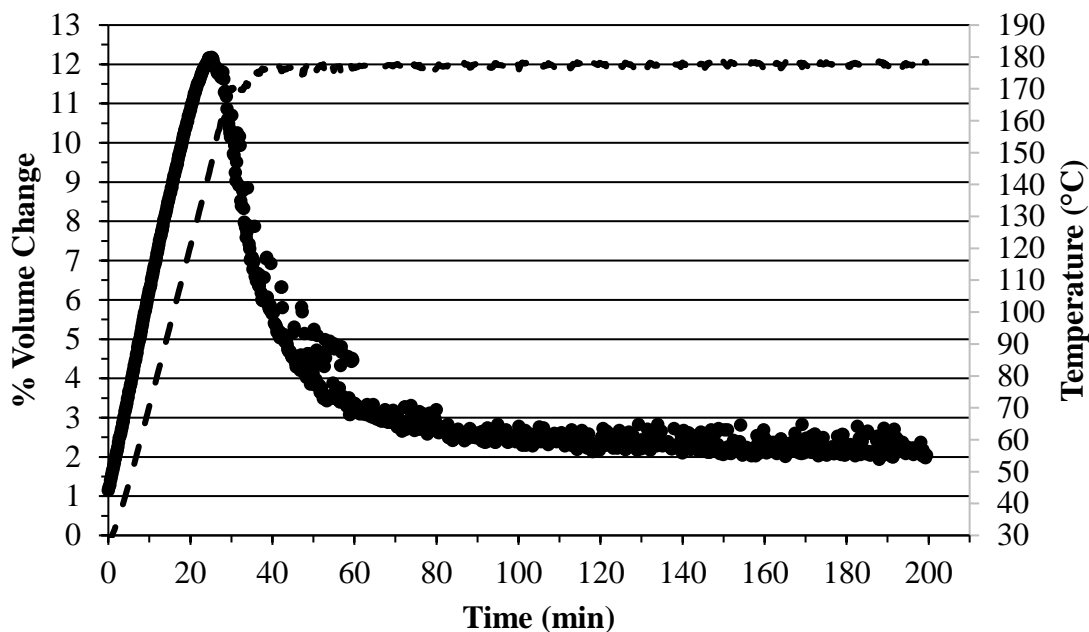


Figure A.6 PVT volume change measurements and cell temperature vs. time.

Black circles represent volume change of uncured 33F and correspond to the left vertical axis. Dashed line represents the cell temperature which contains the sample and mercury confining fluid, and corresponds to the right vertical axis.

In addition to chemical shrinkage simulations, CTE was also calculated from changes in simulated density as a function of temperatures. A linear of best-fit was applied to the density vs. temperature curves below the knee, as visualized in Figure A.2. The calculated CTE values were volumetric and converted to linear CTE values for facile comparison to experimental values from thermomechanical analysis. Linear CTE as a function of conversion for simulated 33F networks is plotted in Figure A.7. At high conversions (91-93%) the average simulated glassy state CTE was $55.7 \mu\epsilon/\text{°C}$, which is very similar to the experimentally-measured CTE of $57.2 \pm 1.0 \mu\epsilon/\text{°C}$, listed in Table 4.6.

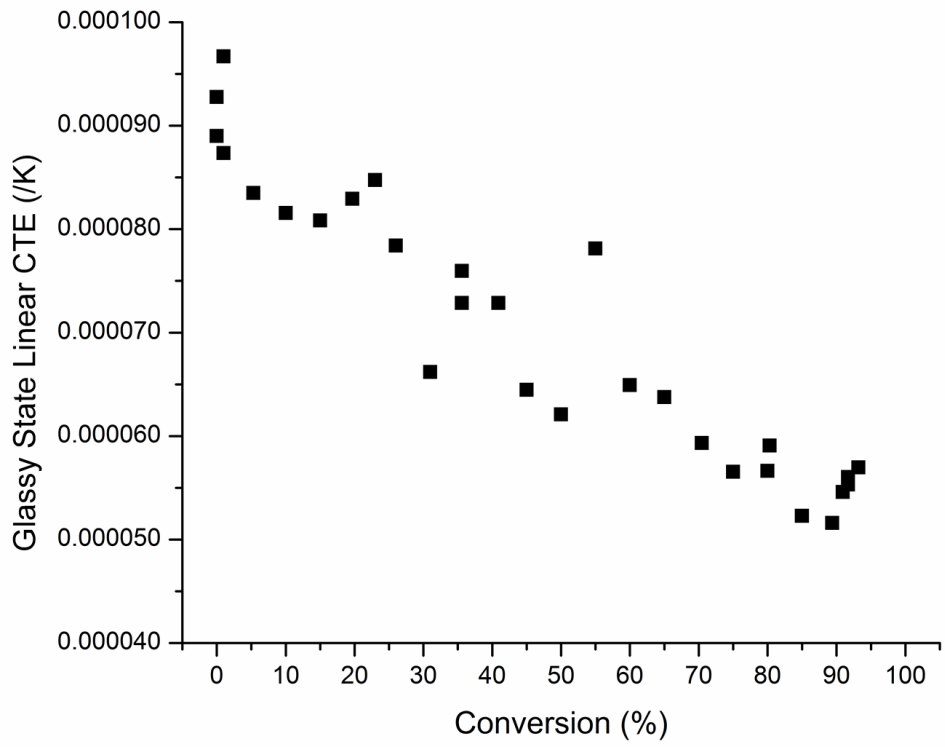


Figure A.7 Simulated linear glassy state CTE of 33F at increasing conversions.

REFERENCES

- (1) Strong, A. B. *Fundamentals of Composite Manufacturing*, 2nd ed.; Society of Manufacturing Engineers: Dearborn, Michigan, 2008.
- (2) Olivier, P. A. *Compos. Part A Appl. Sci. Manuf.* **2006**, *37*, 602–616.
- (3) Merzlyakov, M.; McKenna, G. B.; Simon, S. L. *Compos. Part A Appl. Sci. Manuf.* **2006**, *37*, 585–591.
- (4) Timmerman, J. F.; Tillman, M. S.; Hayes, B. S.; Seferis, J. C. *Compos. Part A Appl. Sci. Manuf.* **2002**, *33*, 323–329.
- (5) Garstka, T.; Ersoy, N.; Potter, K. D.; Wisnom, M. R. *Compos. Part A Appl. Sci. Manuf.* **2007**, *38*, 2517–2526.
- (6) Li, C.; Browning, A. R.; Christensen, S.; Strachan, A. *Compos. Part A Appl. Sci. Manuf.* **2012**, *43*, 1293–1300.
- (7) Madhukar, M. S.; Genidy, M. S.; Russell, J. D. *J. Compos. Mater.* **2000**, *34*, 1882–1904.
- (8) Lee, C. W.; Tienda, K. A.; Storage, T. M. *SAMPE Conf. Proc.* **2014**.
- (9) Olivier, P. A.; Sawi, I. *Int. J. Mater. Form.* **2010**, *3*, 1373–1389.
- (10) Odian, G. *Principles of Polymerization*, 4th ed.; John Wiley & Sons: Hoboken, New Jersey, 2004.
- (11) Bruice, P. Y. *Essential Organic Chemistry*, 2nd ed.; Pearson Education, Inc.: Upper Saddle River, New Jersey, 2010.
- (12) Wisnom, M. R.; Gigliotti, M.; Ersoy, N.; Campbell, M.; Potter, K. D. *Compos. Part A Appl. Sci. Manuf.* **2006**, *37*, 522–529.
- (13) Lange, J.; Toll, S.; Månson, J.-A. E. *Polymer (Guildf)*. **1997**, *38*, 809–815.

- (14) Nawab, Y.; Tardif, X.; Boyard, N.; Sobotka, V.; Casari, P.; Jacquemin, F. *Compos. Sci. Technol.* **2012**, *73*, 81–87.
- (15) Boriek, A. M.; Akin, B. E. *J. Compos. Mater.* **1989**, *22*, 986–1002.
- (16) Li, C.; Potter, K.; Wisnom, M. R.; Stringer, G. *Compos. Sci. Technol.* **2004**, *64*, 55–64.
- (17) Eom, Y.; Boogh, L.; Michaud, V.; Sunderland, P.; Månson, J.-A. E. *Polym. Eng. Sci.* **2001**, *41*, 492–503.
- (18) Saraswat, M. K.; Jansen, K. M. B.; Ernst, L. J. In *2006 1st Electronic Systemintegration Technology Conference*; Ieee, 2006; pp 782–787.
- (19) Khoun, L.; Hubert, P. *Polym. Compos.* **2010**, *31*, 1603–1610.
- (20) Tcharkhtchi, A.; Gouin, E.; Verdu, J. *J. Polym. Sci. Part B Polym. Phys.* **2000**, *38*, 537–543.
- (21) Chompff, A. J.; Newman, S. In *ACS Symposium on Highly Cross-Linked Polymer Networks*; Plenum Press, 1970.
- (22) Yang, L.; Hristov, H. A.; Yee, A. F.; Gidley, D. W.; Bauchiere, D.; Halary, J. L.; Monnerie, L. *Polymer (Guildf)*. **1995**, *36*, 3997–4003.
- (23) Reese, R. P.; Gossard, Jr., T. W. Near Zero CTE Composite Patent, 1997.
- (24) Sulaiman, S.; Brick, C. M.; De Sana, C. M.; Katzenstein, J. M.; Laine, R. M.; Basheer, R. A. *Macromol. Rapid Commun.* **2006**, *39*, 5167–5169.
- (25) Adolf, D.; Chambers, R. *Polymer (Guildf)*. **1997**, *38*, 5481–5490.
- (26) Francis, L. F.; McCormick, A. V.; Vaessen, D. M.; Payne, J. A. *J. Mater. Sci.* **2002**, *37*, 4717–4731.
- (27) Lange, J.; Toll, S.; Månson, J.-A. E. *Polymer (Guildf)*. **1995**, *36*, 3135–3141.

- (28) Shenogin, S.; Raravikar, N.; Ozisik, R.; Keblinski, P. *J. Polym. Sci. Part B Polym. Phys.* **2009**, *47*, 2114–2121.
- (29) Telford, R.; Katnam, K. B.; Young, T. M. *Compos. Struct.* **2014**, *107*, 502–511.
- (30) Kulkarni, R.; Ochoa, O. *J. Compos. Mater.* **2005**, *40*, 733–754.
- (31) Mott, R. L. *Applied Strength of Materials*, 5th ed.; Anthony, V. R., Krassow, E., Eds.; Pearson Education, Inc.: Upper Saddle River, New Jersey, 2008.
- (32) Shokrieh, M. M.; Daneshvar, A.; Akbari, S.; Chitsazzadeh, M. *Carbon N. Y.* **2013**, *59*, 255–263.
- (33) Poveda, R. L.; Achar, S.; Gupta, N. *Jom* **2012**, *64*, 1148–1157.
- (34) Shokrieh, M. M.; Daneshvar, A.; Akbari, S. *Mater. Des.* **2014**, *53*, 209–216.
- (35) Eom, Y.; Boogh, L.; Michaud, V.; Månson, J.-A. E. *Polym. Compos.* **2002**, *2*, 1044–1056.
- (36) Li, Q.; Hutcheson, S. A.; McKenna, G. B.; Simon, S. L. *J. Polym. Sci. Part B Polym. Phys.* **2008**, *46*, 2719–2732.
- (37) Leroy, E.; Dupuy, J.; Maazouz, A.; Seytre, G. *Polymer (Guildf)*. **2005**, *46*, 9919–9927.
- (38) Zarrelli, M.; Skordos, A. A.; Partridge, I. K. *Plast. Rubber Compos. Process. Appl.* **2002**, *31*, 377–384.
- (39) Kravchenko, O. G.; Li, C.; Strachan, A.; Kravchenko, S. G.; Pipes, R. B. *Compos. Part A Appl. Sci. Manuf.* **2014**, *66*, 35–43.
- (40) Prasatya, P.; McKenna, G. B.; Simon, S. L. *J. Compos. Mater.* **2001**, *35*, 826–848.
- (41) Dodiuk, H.; Goodman, S. H. *Handbook of Thermoset Plastics*, Third.; Elsevier Inc.: Kidlington, Oxford, UK, 2014.

- (42) Morrison, F. A. *Understanding Rheology*; Oxford University Press: New York, New York, 2001.
- (43) Archer, E.; Broderick, J.; McIlhagger, A. T. *Compos. Part B Eng.* **2014**, *56*, 424–430.
- (44) Genidy, M. S.; Madhukar, M. S.; Russell, J. D. *J. Compos. Mater.* **2000**, *34*, 1905–1925.
- (45) Van Assche, G.; Van Hemelrijck, A.; Rahier, H.; Van Mele, B. *Thermochim. Acta* **1996**, *286*, 209–224.
- (46) Gillham, J. K. *Polym. Eng. Sci.* **1986**, *26*, 1429–1433.
- (47) Kremer, F.; Schönhals, A. In *Broadband Dielectric Spectroscopy*; Springer, 2002; pp 363–366.
- (48) Ersoy, N.; Garstka, T.; Potter, K.; Wisnom, M. R.; Porter, D.; Clegg, M.; Stringer, G. *Compos. Part A Appl. Sci. Manuf.* **2010**, *41*, 401–409.
- (49) Parlevliet, P. P.; Bersee, H. E. N.; Beukers, A. *Polym. Test.* **2010**, *29*, 291–301.
- (50) Sicot, O.; Gong, X. L.; Cherouat, a.; Lu, J. *J. Compos. Mater.* **2003**, *37*, 831–844.
- (51) Mülle, M.; Collombet, F.; Olivier, P.; Grunevald, Y.-H. *Compos. Part A Appl. Sci. Manuf.* **2009**, *40*, 94–104.
- (52) Okabe, Y.; Yashiro, S.; Tsuji, R.; Mizutani, T.; Takeda, N. *Compos. Part A Appl. Sci. Manuf.* **2002**, *33*, 991–999.
- (53) de Oliveira, R.; Lavanchy, S.; Chatton, R.; Costantini, D.; Michaud, V.; Salathé, R.; Månson, J.-A. E. *Compos. Part A Appl. Sci. Manuf.* **2008**, *39*, 1083–1090.
- (54) Anagnostopoulos, G.; Parthenios, J.; Galiotis, C. *Mater. Lett.* **2008**, *62*, 341–345.
- (55) Melanitis, N.; Galiotis, C.; Tetlow, P. L.; Davies, C. K. L. *Composites* **1993**, *24*,

459–466.

- (56) Filiou, C.; Galiotis, C.; Batchelder, D. N. *Composites* **1992**, *23*, 28–38.
- (57) Crasto, A. S.; Kim, R. Y.; Russell, J. D. *Polym. Compos.* **2002**, *23*, 454–463.
- (58) Darrow, D. A.; Smith, L. V. *Int. SAMPE Tech. Conf.* **2001**, *33*, 326–337.
- (59) Kappel, E.; Stefaniak, D.; Hühne, C. *Compos. Struct.* **2013**, *106*, 615–625.
- (60) Zhu, Q.; Geubelle, P. H.; Li, M.; Tucker, C. L. *J. Compos. Mater.* **2001**, *35*, 2171–2205.
- (61) Kim, K. S.; Hahn, H. T. *Compos. Sci. Technol.* **1989**, *36*, 121–132.
- (62) Palerosi, A. C.; de Almeida, S. F. M. *Compos. Part A Appl. Sci. Manuf.* **2007**, *38*, 2283–2293.
- (63) Gosse, J.; Christensen, S. In *42nd AIAA/ASME/ASCE/AHSIASC Structures, Structural Dynamics, and Materials Conference & Exhibit*; American Institute of Aeronautics and Astronautics: Seattle, WA, 2001.
- (64) Heinz, S. R.; Wiggins, J. S. *Polym. Test.* **2010**, *29*, 925–932.
- (65) Hiemenz, P. C.; Lodge, T. P. *Polymer Chemistry*, 2nd ed.; Taylor & Francis Group: Boca Raton, Florida, 2007.
- (66) Tobolsky, A. V. *Properties and Structure of Polymers*; Hollomon, J. H., Burke, J. E., Chalmers, B., Sproull, R. L., Eds.; John Wiley & Sons: New York, New York, 1960.
- (67) Patrone, P. N.; Tucker, S.; Dienstfrey, A. **2016**.
- (68) Jackson, M. B.; Heinz, S. R.; Wiggins, J. S. *Polym. Test.* **2012**, *31*, 1131–1139.
- (69) Heinz, S.; Tu, J.; Jackson, M.; Wiggins, J. *Polymer (Guildf)*. **2016**, *82*, 87–92.
- (70) Heinz, S. R. Development and Utilization of Digital Image Correlation Techniques

for the Study of Structural Isomerism Effects on Strain Development in Epoxy Network Glasses, University of Southern Mississippi, 2011.

- (71) Raghava, R.; Caddell, R. M.; Yeh, G. S. Y. *J. Mater. Sci.* **1973**, *8*, 225–232.
- (72) Rottler, J.; Robbins, M. O. *Phys. Rev. E* **2001**, *64*, 51801.
- (73) David, L.; Quinson, R.; Gauthier, C.; Perez, J. *Polym. Eng. Sci.* **1997**, *37*, 1633–1640.
- (74) Eyring, H. *J. Chem. Phys.* **1936**, *4*, 283.
- (75) Argon, A. S. *Philos. Mag.* **1973**, *28*.
- (76) Duckett, R. A.; Rabinowitz, S.; Ward, I. M. *J. Mater. Sci.* **1970**, *5*, 909–915.
- (77) McGinty, B. Hydrostatic & Deviatoric Stresses
<http://www.continuummechanics.org/index.html> (accessed Oct 7, 2015).
- (78) Mott, P. H.; Argon, A. S.; Suter, U. W. *Philos. Mag. A* **1993**, *68*, 537–564.
- (79) Rusch, K. C.; Beck, R. H. *J. Macromol. Sci. Part B* **1969**, *3*.
- (80) Stachurski, Z. H. *Prog. Polym. Sci.* **1997**, *22*, 407–474.
- (81) Tu, J.; Tucker, S. J.; Christensen, S.; Sayed, A. R.; Jarrett, W. L.; Wiggins, J. S. *Macromolecules* **2015**, *48*, 1748–1758.
- (82) Chen, L. P.; Yee, A. F.; Moskala, E. J. *Macromolecules* **1999**, *32*, 5944–5955.
- (83) Misasi, J. Hybrid Aryl-Ether-Ketone and Hyperbranched Epoxy Networks, The University of Southern Mississippi, 2015.
- (84) Urbaczewski-Espuche, E.; Galy, J.; Gerard, J. F.; Pascault, J. P.; Sautereau, H. *Polym. Eng. Sci.* **1991**, *31*, 1572–1580.
- (85) Bartolotta, A.; Cerini, G.; Carini, G.; Di Marco, G.; Tripodo, G. *Macromolecules* **2010**, *43*, 4798–4804.

- (86) Vogel, M.; Medick, P.; Rössler, E. A. *Annu. Reports NMR Spectrosc.* **2005**, *56*, 231–299.
- (87) Henrichs, P. M.; Nicely, V. A.; Fagerburg, D. R. *Macromolecules* **1991**, *24*, 4033–4037.
- (88) Garwe, F.; Schonhals, A.; Lockwenz, H.; Beiner, M.; Schroter, K.; Donth, E. *Macromolecules* **1996**, *29*, 247–253.
- (89) Chen, K.; Schweizer, K. S. *Europhys. Lett.* **2007**.
- (90) Lee, H.-N.; Riggelman, R. A.; De Pablo, J. J.; Ediger, M. D. *Macromolecules* **2009**, *42*, 4328–4336.
- (91) Knauer, K. M.; Greenhoe, B. M.; Wiggins, J. S.; Morgan, S. E. *Polym. (United Kingdom)* **2015**, *57*, 88–98.
- (92) Knauer, K. M. Surface and Interfacial Design and Control of High Performing Thermoplastics: Polysulfones and Beyond, The University of Southern Mississippi, 2016.
- (93) Kaushik, M. Free Volume Studies of Various Polymeric Systems Using Positron Annihilation and PVT-EOS Analyses, The University of Southern Mississippi, 2011.
- (94) Jackson, M. B. Effects of Molecular Architecture on Fluid Ingress Behavior of Glassy Polymer Networks, University of Southern Mississippi, 2011.
- (95) McNair, O. D. Investigations Toward Tunability of Mechanical, Thermal, and Impact Properties of Thiol-ene Networks for Novel High Energy Absorbing Materials, The University of Southern Mississippi, 2013.
- (96) Ngai, K. L.; Roland, C. M. *Macromolecules* **1993**, *26*, 6824–6830.

- (97) Owen, A. J.; Bonart, R. *J. Appl. Polym. Sci.* **1997**, *64*, 77–93.
- (98) Andjelic, S.; Fitz, B.; Mijovic, J. *Macromolecules* **1997**, *30*, 5239–5248.
- (99) Fitz, B.; Andjelic, S.; Mijović, J. *Macromolecules* **1997**, *30*, 5227–5238.
- (100) Angell, C. A. *J. Non. Cryst. Solids* **1985**, *73*, 1–17.
- (101) Williams, M. L.; Landel, R. F.; Ferry, J. D. *J. Am. Chem. Soc.* **1955**, *77*, 3701–3707.
- (102) Qin, Q.; McKenna, G. B. *J. Non. Cryst. Solids* **2006**, *352*, 2977–2985.
- (103) Angell, C. A. *Polymer (Guildf)*. **1997**, *38*, 6261–6266.
- (104) McCrum, M. G.; Read, B. E.; Williams, G. *Anelastic and Dielectric Effects in Polymeric Solids*; Wiley: New York, New York, 1967.
- (105) Huang, D.; McKenna, G. B. *J. Chem. Phys.* **2001**, *114*, 5621.
- (106) Roland, C. M.; Santangelo, P. G.; Ngai, K. L. *J. Chem. Phys.* **1999**, *111*, 5593.
- (107) Ngai, K. L.; Yamamuro, O. *J. Chem. Phys.* **1999**, *111*, 10403.
- (108) GOM. ARAMIS User Manual, 2007.
- (109) Sachs, C.; Fabritius, H.; Raabe, D. *J. Struct. Biol.* **2006**, *155*, 409–425.
- (110) Godara, A.; Raabe, D. *Compos. Sci. Technol.* **2007**, *67*, 2417–2427.
- (111) Godara, a.; Raabe, D.; Bergmann, I.; Putz, R.; Müller, U. *Compos. Sci. Technol.* **2009**, *69*, 139–146.
- (112) Parsons, E. M.; Boyce, M. C.; Parks, D. M.; Weinberg, M. *Polymer (Guildf)*. **2005**, *46*, 2257–2265.
- (113) Yu, H.; Mhaisalkar, S. G.; Wong, E. H. *Macromol. Rapid Commun.* **2006**, *27*, 1393–1397.
- (114) Chu, T. C.; Ranson, W. F.; Sutton, M. A. *Exp. Mech.* **1985**, *25*, 232–244.

- (115) Bruck, H. A.; McNeill, S. R.; Sutton, M. A.; Peters, W. H. *Exp. Mech.* **1989**, *29*, 261–267.
- (116) Peters, WH; Ranson, W. *Opt. Eng.* **1982**, *21*, 427–431.
- (117) Lyons, J. S.; Liu, J.; Sutton, M. A. *Exp. Mech.* **1996**, *36*, 64–70.
- (118) McClung, A. J. W.; Tandon, G. P.; Goecke, K. E.; Baur, J. W. *Polym. Test.* **2011**, *30*, 140–149.
- (119) Jerabek, M.; Major, Z.; Lang, R. W. *Polym. Test.* **2010**, *29*, 407–416.
- (120) Bing, P.; Hui-min, X.; Tao, H.; Asundi, A. *Polym. Test.* **2009**, *28*, 75–83.
- (121) Wang, S.; Liang, Z.; Gonnet, P.; Liao, Y. H.; Wang, B.; Zhang, C. *Adv. Funct. Mater.* **2007**, *17*, 87–92.
- (122) Guiver, M. D.; Lee, Y. M. *Science (80-.)*. **2013**, *339*, 284–286.
- (123) Karayiannis, N. C.; Mavrantzas, V. G.; Theodorou, D. N. *Macromolecules* **2004**, *37*, 2978–2995.
- (124) Niemelä, S.; Leppänen, J.; Sundholm, F. *Polymer (Guildf)*. **1996**, *37*, 4155–4165.
- (125) Ding, M. *Prog. Polym. Sci.* **2007**, *32*, 623–668.
- (126) Adam, G.; Gibbs, J. H. *J. Chem. Phys.* **1965**, *43*, 139–146.
- (127) Kunal, K.; Robertson, C. G.; Pawlus, S.; Hahn, S. F.; Sokolov, A. P. *Macromolecules* **2008**, *41*, 7232–7238.
- (128) Simha, R.; Boyer, R. F. *J. Chem. Phys.* **1962**, *37*, 1003.
- (129) White, R. P.; Lipson, J. E. G. *Macromolecules* **2016**, *49*, 3987–4007.
- (130) Jackson, M.; Kaushik, M.; Nazarenko, S.; Ward, S.; Maskell, R.; Wiggins, J. *Polymer (Guildf)*. **2011**, *52*, 4528–4535.
- (131) Mol, G. N.; Harris, K. D.; Bastiaansen, C. W. M.; Broer, D. J. *Adv. Funct. Mater.*

- 2005**, *15*, 1155–1159.
- (132) Cohen, M. H.; Grest, G. S. *Phys. Rev. B* **1979**, *20*, 1077–1098.
- (133) *EPON 862 Technical Data Sheet*; 2005.
- (134) *EPON 825 Technical Data Sheet*; 2005.
- (135) Blanco, M.; Ramos, J. A.; Goyanes, S.; Rubiolo, G.; Salgueiro, W.; Somoza, A.; Mondragon, I. *J. Polym. Sci. Part B Polym. Phys.* **2009**, *47*, 1240–1252.
- (136) Won, Y. G.; Galy, J.; Pascault, J. P.; Verdu, J. *Polymer (Guildf)*. **1991**, *32*, 79–83.
- (137) Shimbo, M.; Ochi, M.; Shigeta, Y. *J. Appl. Polym. Sci.* **1981**, *26*, 2265–2277.
- (138) Bandyopadhyay, A.; Valavala, P. K.; Clancy, T. C.; Wise, K. E.; Odegard, G. M. *Polymer (Guildf)*. **2011**, *52*, 2445–2452.
- (139) Detwiler, A. T.; Lesser, A. J. *J. Appl. Polym. Sci.* **2010**, *117*, 1021–1034.
- (140) Yossi, C.; Smarajit, K.; Itamar, P.; Konrad, S. *Europhys. Lett.* **2012**, *100*, 36003.
- (141) Cukierman, S.; Halary, J.-L.; Monnerie, L.; Halary, J.-L.; Cukierman, S. *Polym. Eng. Sci.* **1991**, *31*, 1476–1482.
- (142) Wu, J.; Huang, G.; Qu, L.; Zheng, J. *J. Non. Cryst. Solids* **2009**, *355*, 1755–1759.
- (143) Morel, E.; Bellenger, V.; Bocquet, M.; Verdu, J. *J. Mater. Sci.* **1989**, *24*, 63–68.
- (144) Goyanes, S.; Rubiolo, G.; Salgueiro, W.; Somoza, A. *Polymer (Guildf)*. **2005**, *46*, 9081–9087.
- (145) Hasan, O. A.; Boyce, M. C. *Polymer (Guildf)*. **1993**, *34*, 5085–5092.
- (146) Oleynik, E. F. *High Performance Polymers*; Baer, E., Moet, S., Eds.; Hauser: Munich, 1990.
- (147) Charge groups and group-based cutoffs theory. *Accelrys Materials Studio Online Help*, 2015.

(148) Patrone, P. N.; Dienstfrey, A.; Browning, A. R.; Tucker, S.; Christensen, S.
Polymer (Guildf). **2016**, *87*, 246–259.

(149) Huntsman. High Performance Components, 2010, 10.